



UNIVERSIDADE FEDERAL DE SANTA CATARINA
CENTRO TECNOLÓGICO
PROGRAMA DE PÓS-GRADUAÇÃO EM ENGENHARIA MECÂNICA

Fernando Moreira Bordin

Grinding wheel characterization by X-ray tomography for grinding cycle optimization

Florianópolis
2019

Fernando Moreira Bordin

Grinding wheel characterization by X-ray tomography for grinding cycle optimization

Tese submetida ao Programa de Pós-Graduação em Engenharia Mecânica da Universidade Federal de Santa Catarina para a obtenção do título de doutor em Engenharia Mecânica.

Orientador: Prof. Dr.-Ing. Walter Lindolfo Weingaertner

Coorientadores: Prof. Dr.-Ing. Márcio Celso Fredel

Prof. Fábio Antônio Xavier, Dr. Eng.

Florianópolis

2019

Ficha de identificação da obra elaborada pelo autor,
através do Programa de Geração Automática da Biblioteca Universitária da UFSC.

Bordin, Fernando Moreira

Grinding wheel characterization by X-ray tomography for grinding cycle optimization / Fernando Moreira Bordin ; orientador, Walter Lindolfo Weingaertner, coorientador, Marcio Celso Fredel, coorientador, Fabio Antonio Xavier, 2019.

145 p.

Tese (doutorado) - Universidade Federal de Santa Catarina, Centro Tecnológico, Programa de Pós-Graduação em Engenharia Mecânica, Florianópolis, 2019.

Inclui referências.

1. Engenharia Mecânica. 2. Usinagem. 3. Retificação. 4. Caracterização de rebolos. 5. Otimização da retificação. I. Weingaertner, Walter Lindolfo. II. Fredel, Marcio Celso. III. Xavier, Fabio Antonio IV. Universidade Federal de Santa Catarina. Programa de Pós-Graduação em Engenharia Mecânica. V. Título.

Fernando Moreira Bordin

Grinding wheel characterization by X-ray tomography for grinding cycle optimization

O presente trabalho em nível de doutorado foi avaliado e aprovado por banca examinadora composta pelos seguintes membros:

Prof. Eraldo Janonne da Silva (Relator), Dr. Eng.
Universidade de São Paulo

Prof. Celso Peres Fernandes, Dr. Eng.
Universidade Federal de Santa Catarina

Prof. Rolf Bertrand Schroeter, Dr. Eng.
Universidade Federal de Santa Catarina

Certificamos que esta é a **versão original e final** do trabalho de conclusão que foi julgado adequado para obtenção do título de doutor em Engenharia Mecânica.

Prof. Jonny Carlos da Silva, Dr. Eng.
Coordenador(a) do Programa

Prof. Dr.-Ing. Walter Lindolfo Weingaertner
Orientador(a)

Florianópolis, 2019.

Este trabalho é dedicado aos meus queridos pais e irmão.

ACKNOWLEDGMENTS

First of all, I would like to thank my supervisor Prof. Dr.- Ing. Walter Lindolfo Weingaertner for his support, patience, help, and advice. This work would not have been possible without his knowledge and practical experience of the grinding process, as well as his fruitful insights. The idea of performing the first X-ray tomography analysis came from him, which turned out to be the most original contribution of the present thesis. Thank you for believing in my research.

I would like to thank both of my co-supervisors, Prof. Dr.- Ing. Márcio Celso Fredel and Prof. Dr. Eng. Fábio Antônio Xavier for their advice and discussions.

I would like to express my deepest gratitude to Dr. Eng. Adriano Boaron, a post-doctoral researcher for grinding processes, and unofficial co-supervisor of this thesis. His support and guidance during my first years at the *Laboratório de Mecânica de Precisão/UFSC*, vast knowledge of the grinding process, machine-tool operation and process monitoring was essential to the development of this study.

I would like to thank the post-doctoral researchers at LMPT/UFSC, Anderson Camargo Moreira and Iara Frangiotti Mantovani, for accepting the challenge of characterizing the grinding wheel samples.

I want to express my sincere gratitude to all my colleagues at LMP/UFSC for their help, joyful and funny atmosphere: Marco Thúlio, Michel Tavares, Jhonathan Gutjahr, Claudio Silveira, Adriano Pereira, Lucas Camargo, Cristian Webber, Ricardo Delgado, Francisco Ratusznei, Jurandir Sousa, Felipe Ebersbach, Caroline Dorneles, Larissa Sirtuli, Edália Azevedo and everyone else. Special thanks to Ricardo Knoblauch and Janaína Geisler Corrêa for their friendship, support, knowledge and many discussions about machining. For my brief time at the MASTeR/UCDavis, I would like to extend my gratitude to Prof. Dr.- Ing. Barbara Linke, Ian Garretson, Destiny Garcia, Akshay Kamath, Malte Seibt and Felicia Fashanu for their support and help.

I would also like to thank the technicians that have strongly contributed to this work by manufacturing many components and workpieces. Many thanks to Valtair Garcez, Joe Schmitz and Hélio Irineu, for your enthusiasm, for your original ideas, and for your hard work.

Thanks to all undergraduate and master students that worked together with me in the grinding research group. In particular, I thank Santiago Caraguay, Gabriel Pillon, Guilherme Paquelin, Vinícius Fernandes and Eduardo Pereira. My deepest gratitude to Lucas Marra for

his hard work, friendship, unique character and for encouraging me to push forward, our grinding discussions made this work possible.

I want to express my deepest gratitude to my friends and almost family, Maurício Branchi and Natacha Tonin Branchi, for their support, friendship and encouragement. I would like to also thank my friend from overseas, Michaela Bautista, for her friendship.

Finally, I want to express my deepest gratitude to my family, for their support, love, guidance. Part of my success I owe to them.

This work was funded by the Coordination for the Improvement of Higher Education Personnel (CAPES) and the National Council for Scientific and Technological Development (CNPq) and I would like to thank them for their support. Also, many thanks to Prof. Dr.- Ing. Ekkard Uhlmann and to M. Eng. Daniel Rolon at the Institute for Machine Tools and Factory Management - TU Berlin, for lending the grinding wheels in the scope of the Brazilian–German Collaborative Research Initiative on Manufacturing Technology. I would like also to thank M. Eng. Oliver Odebrecht and his company, Cantena, for providing information regarding the grinding wheels, as well as donating the dressing plate used in the experiments.

“True science teaches, above all, to doubt and to be ignorant.”

(UNAMUNO, 1913)

RESUMO

A redução dos tempos de ciclo na retificação cilíndrica periférica de mergulho influencia a qualidade do produto manufaturado. De modo a obter um componente livre de alterações deletérias ao seu rendimento e tempo de vida, é de prática comum na indústria reduzir a taxa de retificação específica, aumentando o tempo de processo. Desta forma, torna-se oportuno empregar ciclos de retificação com sequências otimizadas de desbaste até acabamento, baseadas no conhecimento da profundidade das modificações na subsuperfície retificada, evitando assim alteração de propriedades mecânicas do componente final e obtendo tempo de processo reduzido. Rebolos com abrasivos de óxido de alumínio microcristalino garantem excelente resistência ao desgaste e versatilidade no dressamento da ferramenta, entretanto com efeitos na subsuperfície ainda não completamente entendidos. Este trabalho mostra que para obter ciclos mais sustentáveis de retificação cilíndrica externa de mergulho de múltiplos estágios, utilizando como ferramenta rebolos vitrificados convencionais, é de fundamental importância conhecer as características reais dos rebolos. Corpos de prova anelares em aço AISI 1040 (temperados e revenidos), foram retificados com rebolos com diferentes concentrações de óxido de alumínio microcristalino (de 0 % até 45%), empregando taxas de retificação específica de desbaste e acabamento. Os critérios de avaliação foram a força de retificação e a integridade da superfície. Os resultados alimentam uma base de dados e auxiliam na determinação de ciclos com tempo de retificação otimizados, restringidos pela espessura das alterações na camada limite e pela rugosidade do componente. A tomografia de raios-X revelou que os rebolos fornecidos sem e com a menor concentração de óxido de alumínio microcristalino apresentam percentuais de ligante maiores que os rebolos com as maiores concentrações de óxido de alumínio microcristalino. A avaliação dos resultados das componentes de força, rugosidade e camada limite afetada, considerando a fração volumétrica de abrasivos, ligantes e poros, permitiu uma avaliação consistente dos resultados. A otimização dos ciclos de desbaste, restrita pela integridade de superfície a ser removido no acabamento, permite reduzir os tempos de retificação com o emprego de ciclos de retificação de múltiplos incrementos, entretanto que ainda exige dados experimentais mais abrangentes para tornar os resultados mais consistentes. Conclui-se também que a substituição de rebolos convencionais por rebolos contendo óxido de alumínio microcristalino deve considerar o conhecimento da composição e da estrutura dos rebolos para permitir previsões adequadas da influência desta sobre a camada limite afetada.

Palavras-chave: Al_2O_3 sol-gel; tomografia de raios-X de alta resolução; fração volumétrica das fases; camada limite afetada; ciclos de retificação; programação dinâmica.

RESUMO EXPANDIDO

Introdução

A aplicação do processo de retificação cilíndrica externa de mergulho de componentes em aço na produção seriada é fundamentalmente focada na utilização de rebolos superabrasivos com grãos de cBN. Entretanto a retificação com tais rebolos requer elevada velocidade de corte, demanda elevada potência instalada e rigidez extrema das máquinas-ferramentas, o que torna o investimento não atrativo na fabricação de pequenos lotes. A utilização de rebolos convencionais vítreos com grãos de óxido de alumínio microcristalino (obtidos pelo processo sol-gel) vem se mostrando uma alternativa interessante, visto a excelente resistência ao desgaste, se comparados aos rebolos de óxido de alumínio monocristalino (obtidos pelo processo de eletro-fusão) e elevada flexibilidade de perfilamento, se comparados aos rebolos superabrasivos. Porém, a inserção destes grãos abrasivos na mistura do rebolo pode trazer alterações nas propriedades físicas e estruturais do mesmo. Informações divulgadas pelos fabricantes de rebolo podem não representar a real estrutura da ferramenta, incorrendo em escolha errônea de condições de emprego, afetando o processo em si e reduzindo ainda mais a precária sustentabilidade do processo.

Os resultados obtidos em estudos sobre a influência da presença dos grãos abrasivos em óxido de alumínio microcristalino em rebolos convencionais tem se mostrado controverso avaliados dentro do campo de pesquisa da integridade de superfícies nos quesitos das modificações topográficas ao longo do tempo de vida e das características térmicas, mecânicas e morfológicas da estrutura do material retificado. O conhecimento da integridade da superfície (textura da superfície e camada limite afetada) em cada etapa da retificação é uma informação crucial, quando se objetiva otimizar ciclos de retificação cilíndrica externa de mergulho de múltiplos estágios, contemplando sequências de desbaste até acabamento. A maximização do volume retificado na operação de desbaste e de pré-acabamento deve considerar o dano da camada limite em cada etapa para minimizar o volume retificado nas operações de retificação de acabamento e de fim de faiscamento e garantir que não remanesçam vestígios dos danos das operações anteriores. A otimização de ciclos de retificação é importante, visto que cada vez mais conceitos de otimização e atualização contínua do processo, fomentados na indústria 4.0, tornam-se relevantes no ambiente fabril e acadêmico.

O planejamento dos ciclos de retificação contempla como entrada os parâmetros de corte, a cinemática do processo de retificação cilíndrica, e a especificação do rebolo. Os resultados de saída do processo de retificação, a exemplo da integridade da superfície, tornam-se as restrições durante o planejamento da sequência de avanços para obter o ciclo otimizado.

Este trabalho mostra uma metodologia para caracterizar a estrutura do rebolo, a fim de obter dados consistentes para elaborar ciclos de retificação de múltiplos estágios, de desbaste até acabamento, que considerem a integridade da superfície e a sustentabilidade do processo, utilizando como ferramentas rebolos convencionais com diversas composições de óxido de alumínio monocristalino (MN) e microcristalino (MC).

Objetivos

O objetivo deste estudo é obter dados experimentais confiáveis, tanto em termos de conhecimento do rebolo empregado quanto em relação aos parâmetros utilizados, para elaborar ciclos de retificação cilíndrica externa de mergulho de múltiplos incrementos com rebolos convencionais compostos por óxido de alumínio monocristalino e microcristalino, minimizando a camada limite afetada. Para tanto, objetivos secundários foram idealizados para dar suporte ao trabalho:

- a) Caracterizar o conteúdo volumétrico das fases do rebolo (abrasivos, poros e ligante);

- b) Verificar a influência da concentração de Al_2O_3 microcristalino na característica do processo: força de retificação;
- c) Verificar a influência da concentração de Al_2O_3 microcristalino na integridade da superfície de componentes retificados;
- d) Avaliar a influência da taxa de retificação específica sobre a extensão dos danos na camada limite afetada;
- e) Elaborar um algoritmo que preveja estratégias de ciclos de retificação de múltiplos incrementos, baseado nas restrições da integridade da superfície;
- f) Avaliar o desempenho das estratégias dos ciclos de retificação de múltiplos incrementos; e
- g) Comparar os rebolos usando indicadores de sustentabilidade como ferramenta de tomada de decisão.

Materiais e métodos

Para alcançar os objetivos propostos, o estudo foi dividido em duas etapas. A etapa I compreende ensaios experimentais exploratórios, visando avaliar a influência das variáveis de entrada (taxa de retificação específica, em regime de desbaste; e rebolos com concentrações crescentes de óxido de alumínio microcristalino, de 0% até 45%) sobre os esforços de retificação e sobre a integridade da superfície (rugosidade e camada limite afetada). Com o conhecimento das influências das variáveis de entrada do processo, a etapa II consiste em expandir os dados experimentais até o regime de acabamento e executar ensaios para alimentar um banco de dados. O banco de dados, por sua vez, é utilizado para elaborar um algoritmo que, com base nas restrições de rugosidade e de espessura da camada limite afetada, desenvolve uma estratégia de retificação de múltiplos incrementos de avanço, otimizada por programação dinâmica.

Os ensaios de retificação cilíndrica externa de mergulho foram realizados em uma retificadora cilíndrica universal, comandada numericamente. O material do corpo de prova anelar, fabricado em aço ABNT 1040 (temperado e revenido), foi retificado com quatro rebolos vitrificados com concentrações incrementais de óxido de alumínio microcristalino (0%, 15%, 30%, e 45%) e o restante em óxido de alumínio monocristalino (100%, 85%, 70%, e 55%) denominados, respectivamente, MC00, MC15, MC30, e MC45. Como informação adicional, as concentrações das fases dos rebolos (poros, ligantes e grãos abrasivos) foram caracterizados via tomografia de raios-X de alta resolução.

Os corpos de prova foram fixos em um dinamômetro rotativo e a retificação aconteceu em balanço.

A textura da superfície dos corpos de prova foi avaliada mediante a medição da rugosidade ao longo da periferia do corpo de prova. As modificações na subsuperfície causadas pelo processo de retificação, avaliadas como espessura da camada limite afetada, foram detectadas com auxílio de microscopia ótica. Uma rotina de processamento da imagem foi empregada e a espessura média da camada limite afetada foi determinada por meio de segmentação de cores nas imagens.

Os resultados da etapa II foram comparados com auxílio de uma ferramenta de tomada de decisão, utilizando alguns indicadores chave de desempenho com foco em sustentabilidade (intensidade de energia elétrica, intensidade de materiais não renováveis, taxa de produção, investimento, custo do trabalho, e vida em fadiga).

Resultados e discussões

Os resultados da análise por tomografia de raios-X de alta resolução dos rebolos mostraram que os rebolos MC00 e MC15 apresentavam o dobro de ligante do que os rebolos MC30 e MC45. Esta informação não está implícita na descrição das características do reboło fornecida pelo

fabricante que se limita a informar o tipo de grão (mono- e mono- + microcristalino), o tamanho do grão, a dureza, a porosidade e o ligante empregado na fabricação do rebolo.

Os resultados da força de retificação e rugosidade, observados para a etapa I, apontaram para um mecanismo dominante de microdesgaste dos rebolos. O mecanismo dominante foi a abrasão dos grãos, identificado pela diminuição da rugosidade ao longo do tempo de vida de cada ciclo, decorrente da formação de plataformas no topo dos grãos e menor influência dos lascamentos dos grãos abrasivos. As componentes da força de retificação indicam um aumento gradativo, decorrente do aumento do número de grãos cinemáticos com a progressão do desgaste, até atingirem um limiar de esforço no qual ocorrem vibrações regenerativas excessivas limitando a duração do ensaio. O comportamento da rugosidade mostra uma tendência de diminuição ao longo do tempo de retificação, resultado que também corrobora com o mecanismo de desgaste por abrasão.

As características da camada limite afetada nos corpos de prova, na retificação com os diferentes rebolos nas diferentes taxas de retificação, apresentaram valores cuja interpretação não seguia as tendências normalmente esperadas. Buscou-se suporte na literatura para identificar as causas destas diferenças não esperadas mostradas na retificação com os rebolos MC00 e MC15 em relação aos rebolos MC30 e MC45. A presença de grãos MC teve efeito significativo na camada limite afetada, elevando a magnitude da espessura das modificações com o aumento da quantidade de grãos MC- Al_2O_3 . A literatura indica que, devido à natureza da obtenção dos grãos de óxido de alumínio microcristalino, a transferência de calor dentro do grão microcristalino é inferior, o que acarreta maiores temperaturas na zona de corte e maior energia para a transformação de fase.

A modificação na camada limite afetada foi identificada como presença de camada branca e camada escura e, associadas a diferentes fenômenos predominantes durante o corte.

Os resultados das medições da força de retificação, da rugosidade e das características da camada limite foram consistentes se avaliados com enfoque isolado para cada rebolo. Entretanto, quando se compara os resultados para as distintas composições indicadas pelo fabricante, são incoerentes com os comportamentos previstos. Os resultados obtidos pelos rebolos MC00 e MC15, que deveriam apresentar um efeito de auto afiação mais acentuado em relação aos rebolos com as concentrações mais elevadas de grãos MC não foram coerentes, exigindo uma ampliação da análise das características dos rebolos.

Com a disponibilidade da informação da real composição e estrutura do rebolo a interpretação dos resultados de retificação obtidos para os 4 rebolos empregados na pesquisa se tornaram claros e interpretáveis.

Os resultados obtidos para o algoritmo desenvolvido para um ciclo de retificação de múltiplos incrementos, ilustram significativa redução de tempo quando se comparados a ciclos de retificação contendo somente dois estágios (desbaste e acabamento). A comparação entre dois rebolos, MC00 e MC45, mostrou pequenas diferenças em termos de tempo de retificação, mas significativas diferenças em termos da rugosidade R_a obtida.

A comparação dos resultados da etapa II utilizando a ferramenta de tomada de decisões sustentáveis mostrou-se adequada. Dentre os dois rebolos comparados, o rebolo MC00 mostrou-se o mais flexível para a aplicação nos dois cenários experimentados (ciclo de retificação sem acabamento e ciclo de retificação com acabamento). O rebolo MC45 mostrou-se eficiente para uma aplicação de retificação sem acabamento, entretanto mostrou-se pouco eficiente para o ciclo de retificação com acabamento, devido à baixa vida em fadiga do componente.

Considerações finais

A avaliação das características dos rebolos obtidos tomografia de raios-X de alta resolução contidas nos rótulos indicativos dos rebolos fornecidos pelo fabricante mostrou não ser o suficientemente completa para permitir uma análise consistente dos resultados de retificação.

Conforme proposto, um algoritmo para elaborar uma estratégia de retificação cilíndrica externa de mergulho de múltiplos incrementos discretos foi desenvolvido. Os resultados simulados pelo algoritmo foram satisfatórios, entretanto os dados iniciais e exploratórios mostraram-se inconsistentes quando se comparam os rebolos com composições distintas. A especificação da dureza dos rebolos, embora idêntica para os quatro rebolos, segundo o fabricante, em decorrência da significativa diferença da quantidade de ligante e quantidade de grãos por unidade de volume apresentavam variações significativas no comportamento das grandezas características na retificação.

Conclui-se que as tendências distintas de comportamentos das grandezas características do processo de retificação empregando rebolos convencionais de óxido de alumínio com grãos micro- e monocristalino descritos na literatura e nos ensaios realizados durante a elaboração desta tese apenas permitem uma interpretação correta se a especificação do rebolo for completa, contendo informações mais detalhadas do que as resumidas na especificação por norma na identificação do rebolo. A tomografia de raios-X de alta resolução mostra ser uma alternativa de avaliação de rebolos, visto que amostras do rebolo podem ser extraídas tanto da periferia como das laterais do rebolo, sem que com isto se prejudique a utilização do rebolo, quer em aplicações industriais ou na pesquisa. A disponibilidade da tomografia de raios-X de alta resolução abre um novo campo de pesquisa na área da retificação e uma nova metodologia de caracterização do rebolo deverá ser desenvolvida, a fim de apresentar com maior clareza a real composições e estrutura dos rebolos e permitir desta forma uma correlação entre os resultados obtidos.

Palavras-chave: Al₂O₃ sol-gel; tomografia de raios-X de alta resolução; fração volumétrica das fases; camada limite afetada; ciclos de retificação; programação dinâmica.

ABSTRACT

Cycle time reduction in cylindrical peripheral plunge grinding influences on the quality of the manufactured product. In order to obtain a component free of deleterious modifications to its performance and lifespan, it is a common practice in the industry to reduce the specific material removal rate which increases the process time. Thus, it becomes opportune to employ grinding cycles, with optimized roughing to finishing sequences, based on the knowledge of the damage depth on the ground subsurface during roughing, avoiding mechanical property's modification on the final component, as well as obtaining reduced process times. Conventional grinding wheels with microcrystalline aluminum oxide abrasive ensure excellent wear resistance and tool dressing flexibility, however with effects on the subsurface still not completely understood. This study shows that to obtain more sustainable multi-step external cylindrical plunge grinding cycles for grinding with conventional grinding wheels, it is of fundamental importance to acknowledge the real grinding wheel characteristics. Ring-shape quenched and tempered AISI 1040 steel workpieces, were ground with grinding wheels with different content of microcrystalline aluminum oxide (from 0%, up to 45%), employing specific material removal rates from roughing to finishing. The evaluation criteria were the grinding force and surface integrity. The results supply a database and help the determination of grinding cycles with optimized grinding time, constrained by the boundary-affected layer thickness and surface roughness of the component. The X-ray tomography revealed that the provided wheels without and with the lowest microcrystalline aluminum oxide content present a higher binder percentage than the wheels with the higher microcrystalline aluminum oxide content. The evaluation of the grinding force components, surface roughness, and boundary-affected layer results, considering volumetric fraction of the abrasives, binder, and pores, allowed a consistent evaluation of the results. The roughing cycle optimization, restricted by the surface integrity and to be removed on the finishing operation, allows the reduction of the grinding times with the use of multi-step grinding cycles, however still requiring consistent reliable in-depth data to make consistent results. It is also concluded that the replacement of the conventional grinding wheels with grinding wheels containing microcrystalline aluminum oxide in the abrasive composition must consider the knowledge of the grinding wheel composition and structure to allow adequate prediction of its influence on the boundary-affected layer.

Keywords: sol-gel Al_2O_3 ; high-resolution X-ray tomography; volumetric phase fraction; boundary-affected layer; grinding cycles; dynamic programming.

ABBREVIATIONS

AISI	American Iron and Steel Institute
ANN	Artificial Neural Network
ANOVA	Analysis of Variance
ASTM	American Society for Testing and Materials
BRAGECRIM	Brazilian–German Collaborative Research Initiative on Manufacturing Technology
CLAHE	Contrast Limited Adaptive Histogram Equalization
DIN	<i>Deutsches Institut für Normung</i>
DF	Degree of Fulfillment
DP	Dynamic Programming
EPMA	Electron Probe Microanalysis
GA	Genetic Algorithm
ISO	International Organization for Standardization
KPI	Key Performance Indicators
LCI	Life Cycle Inventory
LCM	<i>Laboratório de Caracterização Microestrutural</i>
LMP	<i>Laboratório de Mecânica de Precisão</i>
LMPT	<i>Laboratório de Meios Porosos e Propriedades Termofísicas</i>
MC	Microcrystalline
MN	Monocrystalline
MRR	Material removal rate
NF	Normalization Factor
OTM	Overtempered Martensite
PC	Personal Computer
RA	Retained Austenite
RCD	Rotating Cutting Dynamometer
SEM	Scanning Electron Microscopy
SG	Sol-Gel
SI	Sustainability Indicators
TEM	Transmission Electron Microscopy
UFSC	<i>Universidade Federal de Santa Catarina</i>
UPLCI	Unit Process Life Cycle Inventory
UTM	Untempered Martensite
UV	Utility Value
WFA	White Fused Alumina
XRD	Diffraction pattern by X-ray Diffraction

SYMBOLS

Capital letters

A_{c3}	$^{\circ}C$	Austenitization temperature
A_0	mm^2	Area constant
A_{eff}	mm^2	Wear flat area
BAL	μm	Boundary-affected layer thickness
C_{EF}	-	Electro-fused aluminum oxide abrasive grits relative cost
C_{GW}	-	Grinding wheel relative cost
C_{SG}	-	Sol-gel aluminum oxide abrasive grits relative cost
D_{waste}	μm	Waste caused by the dressing operation
E_{basic}	W	Power necessary for the machine-tool to function
$E_{grinding}$	W	Energy dispended during the grinding process
E_{idle}	W	Energy used for tasks that do not involve engagement
E_{total}	W	Total energy spent during the grinding process
F_{holder}	N	Force due to workpiece's holder mass
F_a	N	Axial force
F_n	N	Normal force
$F_{n, \infty}$	N	Normal force at the stationary region
F_n'	N/mm	Specific normal force
$F_{n, crit}'$	N/mm	Specific critical normal force
F_R	N	Resulting force
$F_{R, total}$	N	Total resulting force
F_t	N	Tangential force
F_t'	N/mm	Specific tangential force
F_w	N	Force due to workpiece's mass
F_x	N	Force on the Cartesian direction X
F_y	N	Force on the Cartesian direction Y
F_z	N	Force on the Cartesian direction Z
G	-	Grinding ratio
HPD	mm	Hardness penetration depth
K_{IC}	MPa	Critical stress intensity factor
K_s	N/mm	Grinding stiffness
K_{st}	-	Theoretical surface concentration factor caused by machining-induced surface texture
M_f	$^{\circ}C$	Martensite finish temperature
M_s	$^{\circ}C$	Martensite start temperature
M_z	$N \cdot m$	Torque on the Cartesian direction Z
N	-	Number of grinding steps/interactions
N_f	-	Number of cycles to fatigue failure
P	W	Grinding power
$P_{spindle}$	W	Grinding wheel spindle power
$P_{cooling pump}$	W	Cooling pump power
$P_{controls, drives}$	W	Necessary power for the machine to function without any motion
Q_w	mm^3/s	Material removal rate
Q_w'	$mm^3/mm \cdot s$	Specific material removal rate / Specific grinding rate
R_0	-	Empirical constant of the surface roughness
R_a	μm	Arithmetic mean surface roughness

R_{\max}	μm	Maximum surface roughness
R_{sk}	-	The symmetry of the surface on the mean line
R_{Sm}	μm	Mean width of the profile elements
R_t	μm	Maximum surface roughness
R_{ts}	μm	Grinding wheel effective roughness
R_z	μm	Mean peak-to-valley surface roughness
U_d	-	Dressing overlap ratio
V_b	%	Volumetric binder concentration
V_g	%	Volumetric abrasive grit concentration
$V_{g, \text{EF}}$	%	Electro-fused volumetric abrasive grit concentration
$V_{g, \text{SG}}$	%	Sol-gel volumetric abrasive grit concentration
V_p	%	Volumetric pore concentration
V_s	mm^3	Grinding wheel wear volume
V_w	mm^3	Material removal
V_w'	mm^3/mm	Specific material removal
Small letters		
a	nm	Martensite's lattice parameter
a_0	nm	Austenite's cubic lattice constant
a_e	mm	Depth of cut
a_{ed}	mm	Depth of cut in dressing
a_p	mm	Width of cut
b_d	mm	Active width of the dressing tool
$b_{s, \text{eff}}$	mm	Active grinding wheel width
d_q	mm	Discrete step dislocation at each iteration
d_e	mm	Equivalent diameter
d_s	mm	Grinding wheel diameter
d_w	mm	Workpiece diameter
d_{wi}	mm	Workpiece initial diameter
d_{wf}	mm	Workpiece final diameter
f_d	mm	Dressing lead
f_{dressing}	part^{-1}	Frequency in which the grinding wheel is dressed
f_n	Hz	Natural frequency
f_s	Hz	Sampling rate
h_{cu}	mm	Chip thickness
k	$\text{W}/\text{m}\cdot\text{K}$	Thermal conductivity
l_c	mm	Contact length
l_{ek}	mm	Real kinematical contact length
l_f	mm	Dislocation
$l_{f, \text{nom}}$	mm	Nominal dislocation
m	-	Constant
m	g	Mass
n	-	Type-dependent load constant
n_s	min^{-1}	Grinding wheel rotation speed
n_w	min^{-1}	Workpiece rotation speed
p_s	J/mm^2	Grinding specific energy
q	-	Speed ratio
q_d	-	Dressing speed ratio
r	mm	Workpiece radius
r	μm	Out-of-roundness
r_m	μm	Residual out-of-roundness

t	s	Time
t_{air}	s	Time spent for grinding wheel movement to the grinding position
t_c	s	Grinding cycle time
t_{dressing}	s	Time to dress grinding wheel after one machined component
t_{grinding}	s	Grinding time
t_{idle}	s	Time spent on idle motion and in grinding process
t_j	s	Time at each step
$t_{\text{transient}}$	s	Grinding wheel entrance time interval
$t_{\text{load/unload}}$	s	Time for loading and unloading the component on the machine-tool
u_j	mm/s	Programmed radial feed rate
v_d	m/s	Dressing roller circumferential speed
v_f	mm/s	Feed rate at last step of the algorithm
v_{fad}	mm/s	Axial dressing feed rate
v_{fr}	mm/s	Radial feed rate
$v_{\text{fr, nom}}$	mm/s	Nominal radial feed rate
v_{ft}	mm/s	Tangential feed rate
$v_{N-1, j}$	mm/s	Reachable feed rate at each step of the algorithm
v_s	m/s	Grinding wheel circumferential speed
v_{sd}	m/s	Grinding wheel circumferential speed during dressing
v_w	m/min	Workpiece speed
x	-	Empirical constant
y	mm	System deformation
y	-	Empirical constant
Greek letters		
α	W/m·K	Thermal conductivity
α	m ² /s	Thermal diffusivity
δ	rad	Equivalent dressing infeed angle
γ	-	Empirical constant
Δr_s	mm	Radial grinding wheel wear
Δr_{sk}	mm	Radial edge wear
θ	rad	Angle of the wheel-workpiece
θ_c	rad	Angle of the wheel-workpiece contact
θ_{mb}	°C	Critical temperature for grinding burn
λ	N/mm	Static grinding system stiffness
λ_c	mm	Wavelength of the profile cut-off filter
λ_s	μm	Wavelength of the micro-roughness filter
η	-	Efficiency for the machine-tool subsystems
ρ	g/cm ³	Specific mass
$\bar{\rho}$	μm	Equivalent root radius of surface roughness valleys
σ_r	MPa	Residual stress
τ	s	Time constant in plunge cylindrical grinding
τ_F	s	Time constant due to system deflection
τ_S	s	Time constant due to grinding wheel wear

CONTENTS

1	INTRODUCTION	20
1.1	PROBLEM DESCRIPTION	20
1.2	OBJECTIVES	22
2	LITERATURE REVIEW	23
2.1	EXTERNAL CYLINDRICAL CIRCUMFERENTIAL PLUNGE GRINDING	23
2.1.1	Optimization of the multi-stage cycle in external cylindrical plunge grinding.....	27
2.1.2	Grinding force and temperature distribution	33
2.2	ALUMINUM OXIDE GRINDING GRITS	35
2.2.1	Production of white fused and sol-gel aluminum oxide	35
2.2.2	Properties of aluminum oxide grits.....	37
2.2.3	Wear of aluminum oxide grinding wheels.....	38
2.3	SURFACE INTEGRITY	43
2.3.1	Surface texture of ground components.....	45
2.3.2	Boundary-affected layer in ground steels.....	49
2.4	SUSTAINABILITY AS A KEY PERFORMANCE INDICATOR IN MANUFACTURING	57
2.5	RESEARCH GAP	59
3	MATERIALS AND METHODS.....	60
3.1	PROCESS PLANNING.....	60
3.2	INPUT SYSTEM PARAMETERS	61
3.2.1	Machine-tool.....	61
3.2.2	Workpiece material	62
3.2.3	Grinding wheel.....	63
3.2.4	Dressing system and conditions.....	65
3.2.5	Cooling media and conditions.....	66
3.2.6	Grinding force measurement system	66
3.2.7	Optimization methodology of the grinding cycle.....	68
3.3	INPUT VARIABLE PARAMETERS	70
3.3.1	Cutting conditions.....	70
3.4	SURFACE INTEGRITY ANALYSIS	71
3.4.1	Workpiece surface texture	71
3.4.2	Workpiece boundary-affected layer analysis	72
3.5	STATISTICAL ANALYSIS	74

3.6	RESULT COMPARISON USING A DECISION-MAKING METHOD	75
4	RESULTS AND DISCUSSION	80
4.1	GRINDING WHEEL CHARACTERIZATION	80
4.2	STAGE I – SINGLE-STEP ROUGH GRINDING CYCLE	86
4.2.1	Grinding force components, F_t' and F_n'	86
4.2.2	Surface roughness	94
4.2.3	Boundary-affected layer	100
4.2.4	Summary of the stage I experiments.....	108
4.3	STAGE II – MULTIPLE-STEP PLUNGE CYCLE	108
4.3.1	Grinding force components, F_n' and F_t'	109
4.3.2	Surface roughness	110
4.3.3	Boundary-affected layer	111
4.3.4	Optimization cycle	113
4.4	ENVIRONMENTAL KEY PERFORMANCE INDICATORS AS A DECISION- MAKING METHOD FOR GRINDING PROCESS EVALUATION.....	115
5	CONCLUSIONS	121
6	SUGGESTION FOR FUTURE STUDIES.....	123
	REFERENCES	124
	APPENDIX A.....	133
	APPENDIX B.....	135
	APPENDIX C.....	138
	APPENDIX D.....	143

1 INTRODUCTION

1.1 PROBLEM DESCRIPTION

Industrial and research interests in grinding can be currently divided into four main applications: sustainable machining, adaptive and automated process control (4.0 industry), grinding of ceramic or brittle materials and grind-hardening [1-3]. Component manufacturers aim to obtain a reliable and cheap product, with relatively low manufacturing times, greater flexibility and sustainable operations [2]. However, the aspects related to the product quality (*e.g.* surface integrity) and production rate (*e.g.* high specific material removal rates and operational costs) are conflicting and should be appreciated through compromise solutions [4]. In terms of sustainable manufacturing, grinding is usually considered as a rather environmentally unfriendly process, for its high specific energy consumption and for its use of cooling lubricants [5].

When it comes to grinding of steel components, superabrasive grinding wheels manufactured with cubic boron nitride (cBN) are the industry's main option. They are highly competitive when compared to conventional grinding wheels, as well as economically advantageous if employed in the manufacturing of large batches of components. However, the use of cBN tools demands machine-tools with high circumferential grinding wheel speeds; advanced dressing process, balancing, cooling and safety systems [6]. These factors significantly increase the costs of the equipment, which makes the investment unattractive to a portion of the industry. An alternative is the application of conventional grinding wheels with microcrystalline aluminum oxide abrasives on its composition.

The development of microcrystalline sintered alumina abrasive grits, obtained by the sol-gel (SG) process, is one of the most important innovations in grinding since the early 1980s. These abrasives, in comparison with white fused alumina (WFA), are characterized by higher ductility, which improves the resistance to brittle fracture. In terms of service life, SG grains are more durable than WFA (between 5 and 30 times more) [7]. However, the cutting conditions for these grinding wheels also must be thoroughly selected.

The selection of input parameters in cylindrical plunge grinding is not only dependent on the component surface texture, but also on the visible and invisible modifications underneath the surface. For the appropriate process design, reliable simulation models can be useful for finding optimal process parameters such as grinding wheel speed, depth of cut, workpiece speed and cutting fluid, so that higher production rate can be achieved whilst potential thermal damage

of the ground surfaces can be avoided [8]. It is widely known that the knowledge of the depth of the workpiece subsurface damage is crucial to elaborate a reliable and optimized grinding cycle plan.

A grinding cycle plan must not only consider the constraints of input parameters but also be aware of the nature of the trajectory in cylindrical plunge grinding, since the ground surface is constantly under material removal and therefore, affected by constant and cyclic material modifications [9]. The cycles of heating and cooling of the ground surface lead to several overlays of material removal, leading to cyclic changes of material microstructure and properties [10].

A possible solution for this problem relies on the application of optimization algorithms that, aiming for the lowest grinding cycle time, also consider the restrictions of surface roughness, roundness, as well as the depth of machining-affected layer [8]. However, it should be noted that in most techniques, optimization of the cycle structure itself is not considered. As a result, the cycles designed according to these methods do not guarantee a minimum processing time [11]. Optimization cycles must guarantee not only a satisfactory surface texture and accuracy but also eliminate the presence of subsurface damage [12], as well as accounting for the grinding wheel's structure and properties in order to obtain reliable data for a discretized and parametric grinding cycle plan.

The boundary-affected layer, a modified portion of the underneath machined surface that is under negative or positive effects of the machining process, is of crucial importance. These modifications are the result of the input parameters (cutting conditions, cooling, grinding wheel specification, machine-tool, etc.) and play a key role in the component's mechanical properties and fatigue life [12]. The investigations of the boundary-affected layer are especially important when grinding with conventional vitreous grinding wheels with electro-fused and sol-gel aluminum oxide content, adequate for high specific material removal rates, where the highest energy is generated [7, 13-14].

However, publications concerning the resulting ground subsurface of steels using mixed abrasive content of monocristalline (MN) and microcrystalline (MC) aluminum oxide grinding wheels are scarce. Authors like Dong *et al.* [15], Fathallah *et al.* [16], Madopothula *et al.* [17], Benini [18] and Brunner [19] are unusual examples of studies which investigated the influence of sol-gel abrasive grits, in conventional vitreous grinding wheels, on the subsurface. However, the surveyed literature does not present a consensus, illustrating cases where the presence of sol-gel grits induces larger alterations in the subsurface and vice-versa.

While the surveyed literature is controversial, the grinding wheel itself, regarded as an input parameter, can also be interpreted as an unknown process variable. For example, grinding wheel manufacturing routes may lead to uneven properties [20]. The grinding wheel volumetric content (pores, binder, and abrasives) and distribution are informed only partially by the normative. By only altering the grinding wheel abrasives, porosity, or binder, it is expected that the grinding wheel presents differences in mechanical resistance, wear, efficiency, thermal conductivity, subsurface damage, and ultimately, the sustainability aspects of the grinding process.

This lack of information and uncertainties highlights the demand for further evaluation of the effects of the grinding wheel's volumetric content, endowed with microcrystalline grits, on the surface integrity focused multi-step grinding cycles plan.

1.2 OBJECTIVES

The main goal of this study is to obtain reliable experimental data, both in terms of knowledge of the employed grinding wheel as well as the used parameters, to elaborate multi-step external cylindrical plunge grinding cycles for conventional grinding wheels composed of monocrystalline and microcrystalline aluminum oxide, which minimizes the boundary-affected layer. To achieve this objective, the following secondary objectives were idealized.

- a) Characterize the grinding wheel volumetric content (abrasives, pores, and binder);
- b) Verify the effects of the microcrystalline Al_2O_3 content on the grinding process characteristic (force);
- c) Verify the effects of the microcrystalline Al_2O_3 content on the surface integrity of the ground component;
- d) Evaluate the extension of damages on the boundary-affected layer, caused by elevated specific material removal rates;
- e) Elaborate an algorithm that predicts a multi-step grinding cycle strategy, based on restrictions of the surface integrity;
- f) Evaluate the performance of the multi-step external cylindrical plunge grinding cycle strategies; and
- g) Compare the grinding wheels using sustainability indicators as a decision-making tool.

2 LITERATURE REVIEW

Grinding is one of the earliest manufacturing techniques ever used by humans. Although the process is to a great extent driven by centuries of experience, it is still an important process and represents a vital research field in the machining process. Grinding spans from very crude and roughing applications at high material removal rates (MRR) to very sophisticated ultraprecision finishing processes [2]. The main goal of the process aims to generate components with specified geometry, tolerance and surface properties. Process stability is required to guarantee a stable behavior between the input and output parameters (Figure 1), where the results can be predicted and strictly correlated, although the individual micro-events are caused by complex phenomena [21].

Figure 1 – Grinding process inputs and outputs (results).

Input parameters		Grinding process	Result
System	Variables	Process characteristics	Technology
Machine: <ul style="list-style-type: none"> type properties 	<ul style="list-style-type: none"> depth of cut workpiece speed feed rate 	<ul style="list-style-type: none"> Grinding force Power Grinding temperature Acoustic emission Process duration 	Workpiece: <ul style="list-style-type: none"> accuracy of shape/dimension surface quality influence on the boundary layer
Workpiece: <ul style="list-style-type: none"> geometry material 			<ul style="list-style-type: none"> grinding wheel speed
Grinding wheel: <ul style="list-style-type: none"> geometry specification 	<ul style="list-style-type: none"> dressing conditions 	<ul style="list-style-type: none"> Vibration External temperature 	
Dressing tool: <ul style="list-style-type: none"> type specification 			<ul style="list-style-type: none"> coolant pressure flow rate
Cooling lubricant: <ul style="list-style-type: none"> type supply 			

Source: Adapted from Klocke [21].

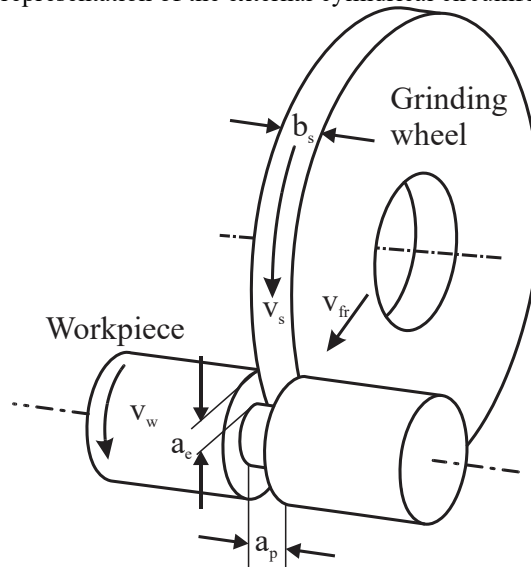
2.1 EXTERNAL CYLINDRICAL CIRCUMFERENTIAL PLUNGE GRINDING

According to the normative DIN 8589 [22], the grinding process with rotating tools is divided into several methods. Among them, the external cylindrical circumferential plunge grinding is employed when obtaining rotation-symmetrical workpieces with a radial feed

velocity v_{fr} , denominated plunge movement. Along with the feed motion, both the grinding wheel and workpiece rotate with grinding wheel circumferential speed v_s and workpiece circumferential speed v_w [21].

Therefore, material removal during cylindrical plunge grinding occurs by radially infeeding a rapidly rotating grinding wheel into a slowly rotating workpiece at a command infeed rate, as depicted in Figure 2 [23]. Typical components machined by this method are crankshafts, camshafts, bearings and hydraulic valve components.

Figure 2 – Schematic representation of the external cylindrical circumferential plunge grinding.



Source: Adapted from Klocke [21].

The process severity is calculated through the material removal rate, which specifies the volume of material removed per time unit. The material removal rate Q_w does not increase with grinding wheel circumferential speed but rather increases with the grinding wheel's feed rate. This parameter is often divided by the effective wheel width b_s , which allows distinguishing between roughing and finishing operations, and is translated as specific material removal rate, also known as specific grinding rate, Q_w' [$\text{mm}^3/\text{mm}\cdot\text{s}$] given by Eq. (1),

$$Q_w' = v_{fr} \cdot \pi \cdot d_w = a_e \cdot v_w, \quad (1)$$

where:

v_{fr} is the radial feed rate [mm/s]

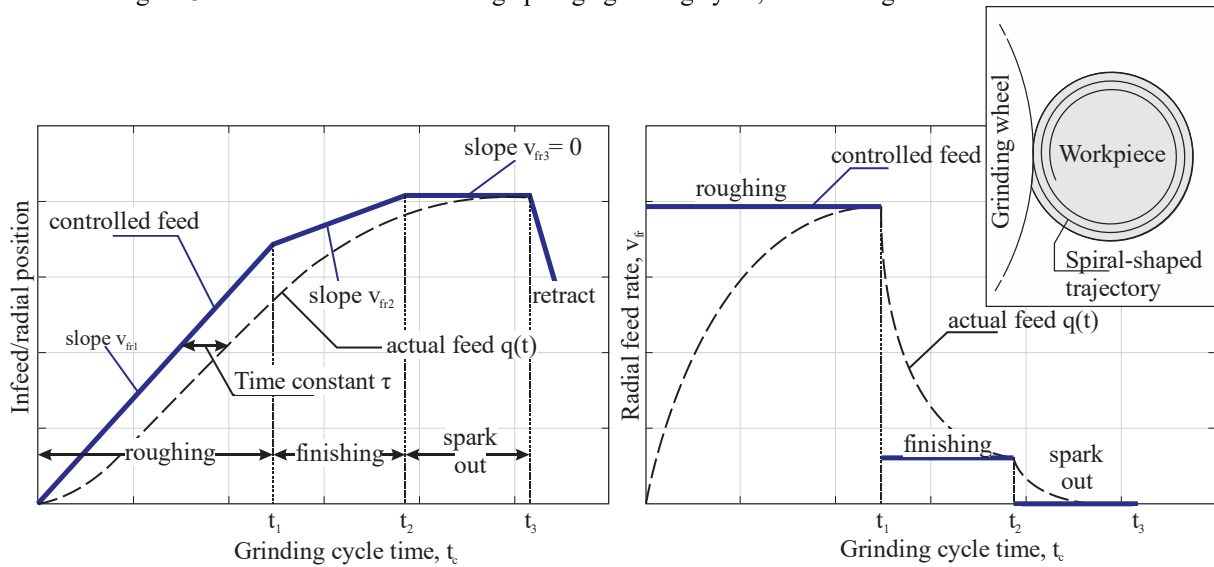
d_w is the workpiece diameter [mm]

a_e is the depth of cut [mm]

v_w is the workpiece circumferential speed [mm/s]

A typical cylindrical grinding cycle consists of three stages (Figure 3). Each stage is performed with a pre-defined radial feed rate v_{fr} : roughing with a fast feed radial rate v_{fr1} ; finishing with a slower feed rate v_{fr2} (typically about 25% of v_{fr1}); and spark-out with zero feed rate ($v_{fr3} = 0$). In response to the controlled feed rate, the actual dislocation into the workpiece follows the curve $q(t)$, whose slope is the actual instantaneous feed rate. The actual feed rate lags behind the controlled feed mainly due to elastic deflection and the wear, discretized as the time constant τ_F of the system deflection (grinding wheel, machine-tool, and workpiece), and time constant τ_S due to radial wear of the grinding wheel [22, 24-25].

Figure 3 – A conventional three-stage plunge grinding cycle, considering the time constant τ .



Source: Adapted from Dong [24].

Obtaining the time constant τ_F in cylindrical plunge grinding is usually proceeded by calculating the Eq. (2) [26],

$$\tau_F = \frac{\pi \cdot d_w \cdot K_S}{v_w \cdot \lambda}, \quad (2)$$

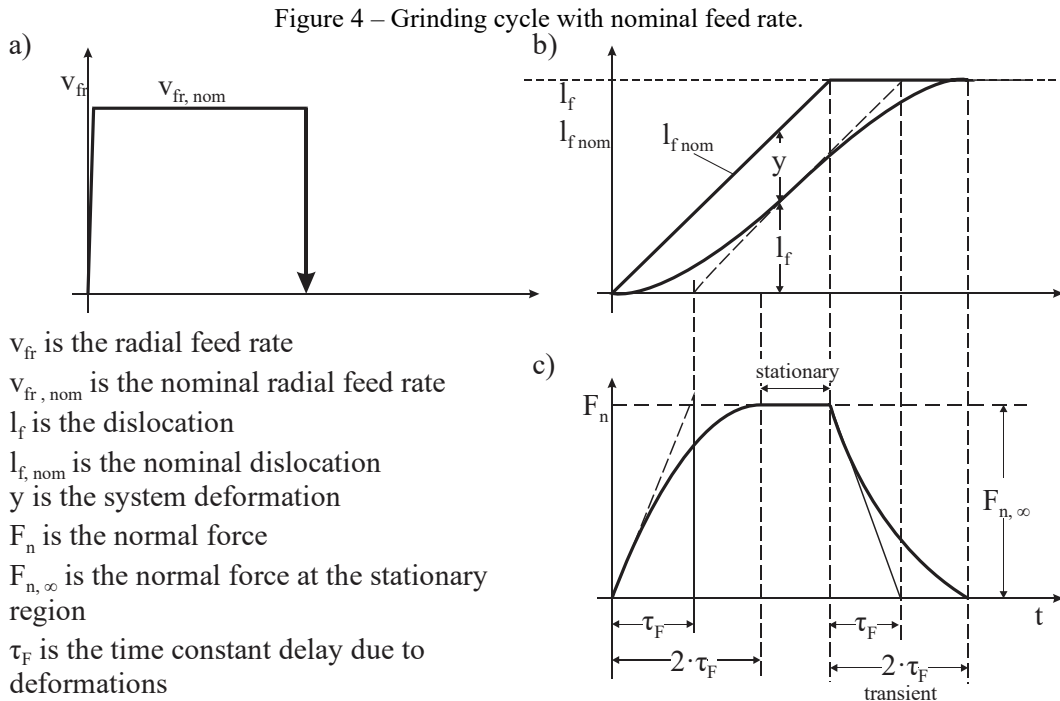
where:

λ is the static grinding system stiffness [N/mm]

K_S is the grinding stiffness [N/mm]

This method to determine the time constant, although precise, requires prior knowledge of the grinding system stiffness, or estimation of such parameters. An alternative,

suit for an experimental approach, as illustrated by Saljé *et al.* [25]. Figure 4 exemplifies the author's consideration.



Source: Adapted from Saljé *et al.* [25].

By applying a constant nominal radial feed rate during the plunge motion (Figure 4a), the deformations (y) suffered by the system are carried out into the process as a time delay (Figure 4b). This leads to a transient stage of the normal force F_n . The time necessary for the system to reach the stationary phase of the normal force ($F_{n, \infty}$) is double the time delay constant [25]. Therefore, by measuring the time necessary for the normal force to reach a stationary phase (Figure 4c), the time constant τ_F can be calculated.

One must keep in mind that the resulting component circumferential geometry presents a spiral shape, governed by the feed rate and workpiece rotation (spiral-shaped trajectory). Thus, the spark-out stage aims to decrease the circumferential error and avoid geometrical deviations.

The grinding process is treated as a finishing process and although the spark-out stage is an important step during the industrial grinding cycle, in research applications it is an undesirable stage that masks the effects of the selected roughing cutting parameters. Thus, when evaluating the depth of surface/subsurface modification caused by the roughing operation in the grinding process, cycles without the spark-out stage are providential. This is an important aspect that is to be considered when planning a grinding cycle optimization.

2.1.1 Optimization of the multi-stage cycle in external cylindrical plunge grinding

In general applications, the industry is forced to select parameters to control the cycle manually, leaning against the saved-up experience. The cycles selected in this way require additional inputs of production resources; they are not only suboptimal but also not rational because in order to fulfill the requirements of the drawing on accuracy and quality underestimated radial feed rates are assigned. As a result, the production capacity of modern CNC machines is used only by 40-60% [25].

Controlling the feed rate in cylindrical circumferential plunge grinding with numeric controlled machines is the object of several studies, as it plays an important role in grinding cycle optimization. Several methods have been proposed to deal with the most challenging problem of cycle optimization in conventional multi-stage grinding. For instance, applying on-line controlled infeed rate based on a particular process characteristic (normal force, grinding power, acoustic emission), and multi-step cycle based on prior experimental results (surface roughness, surface burn, depth of machined affected layer) [27-30].

Authors like Chang *et al.* [31] used models such as support vector machine (SVM) for classification and regression of input data (grinding conditions, surface roughness), aiming to achieve an optimized cycle. The authors compared those methods with backpropagation (BP) neural networks and achieved errors below 8%. On a similar approach, Rudapraty *et al.* [32] employed the response surface method (RSM) to model the external cylindrical grinding behavior of vibrations and surface roughness, using measured experimental data. The model exhibited a regression R^2 value of 0.98. Recently, Dražumerič *et al.* [12] applied a temperature-based method to determinate the feed increments in crankshaft grinding. The composed model considered the input parameters, *i.e.* cutting parameters, to output a multi-step grinding cycle based on a preset temperature threshold. The model results were verified by empirical experiments, and the shortest possible cycle time could also be found.

Equations were also used in this field. Webster and Zhao [33] elaborated early ideas of time-optimum adaptive control equations for plunge grinding considering the tool/workpiece stiffness through the time constant τ . González-Santander *et al.* [34] developed an analytical equation to avoid thermal damage on surface grinding using the grinding power as input. The depth of cut (a_c) was used as the controlled parameter.

Other approaches were also employed. Ning *et al.* [35] elaborated a supervision system for workpiece size, based on neural network and fuzzy control system with human interaction, which allowed it to find a local optimum grinding cycle. Nguyen and Zhang [36] developed a

cycle optimization algorithm that considers the energy input to generate a hardened layer (*i.e.* grind-hardening) using the premise of grinding overlapping surfaces. Although the authors' objective was to obtain a specific thickness of the affected layer, not avoid it, the results present errors of up to 15% in comparison with the experimental results, which illustrates the capability of such methods.

In contrast with online adaptive control systems, which use either a force, acoustic emission or motor power signal to determine grinding regime, the development of an offline algorithm that optimizes the cycle might be advantageous. This relies on the fact that the grinding damage on the subsurface is not easily predictable and it is affected by many process variables (input parameters, grinding wheel wear, dressing conditions, etc.). Methods like genetic algorithm (GA), artificial neural networks (ANN), fuzzy logic, dynamic programming (DP), among others, elaborate an optimal grinding cycle using (or not) a pre-defined mathematical (or empirical) model and real measurable data [24]. It is reasonable to state that, in order to calculate the optimal machining cycles, a method that is capable of finding the optimal cycle parameters must be selected based on a minimum number of observations, as well as consistent data input. Moreover, the method must meet the following requirements:

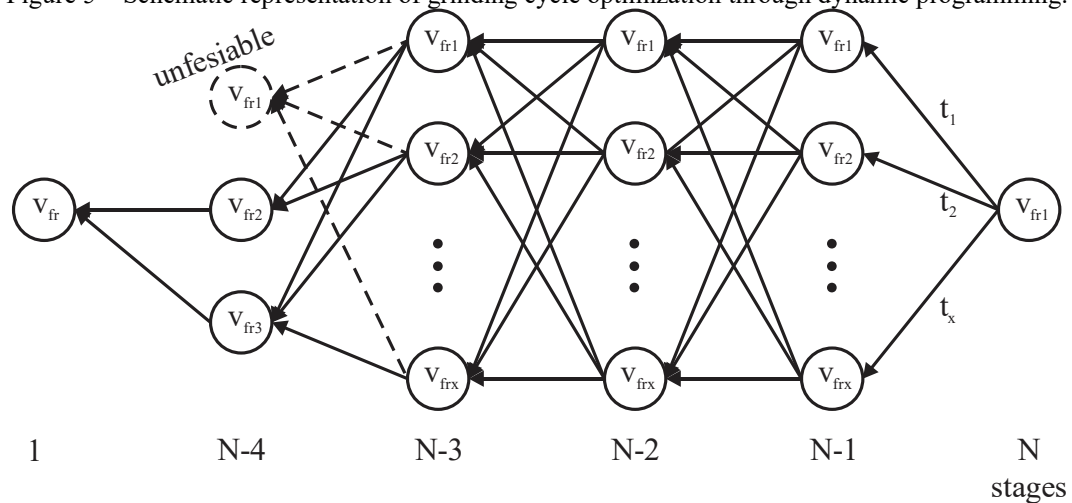
- a) insensitivity to the differentiability and continuity of the control models and constraints, due to cycle control through steps;
- b) allowance of an unlimited number of restrictions, as the grinding process is affected by many inputs and external effects, as well it is subjected to component precision requirements; and
- c) preliminary construction of the constraint's boundaries should not be required. Restrictions related to machining precision and surface roughness are only specified at the end of the cycle.

Dynamic programming (DP) is considered by many authors a logical choice for machining optimization because of the sequential nature of machining operations. In terms of process control, DP can find a sequence of optimal control values to transform the system from an initial state to a specific final state. It also considers constraints and provides a globally optimal solution [24].

Dynamic programming employs a discrete control parameter, which in case of experimental input data helps to obtain a quick response from the method, without the need for extensive experimental data (artificial intelligence) or complex evolutionary algorithm with a large scale of iteration (genetic algorithm) [24].

Cycle-time minimization, for example, is defined as a sequential decision-making problem, where the cycle is discretized into a finite number of small steps. However, since the total cycle time is unknown, steps are uniformly discretized into several steps with incremental distance dq [24]. A schematic representation of the algorithm is given in Figure 5.

Figure 5 – Schematic representation of grinding cycle optimization through dynamic programming.



— Possible feed rate choice, respecting the restriction

- - - - - Possible feed rate choice, not respecting the restriction

v_{fr} : real radial feed rate

t : calculated time for each stage, associated with a given radial reduction

N : Number of grinding steps/iterations

Source: Adapted from Hillier and Liebermann [37].

In this topic, Dong [24] elaborated a methodology that employs a dynamic programming algorithm to calculate the necessary feed rate to optimize the internal cylindrical grinding time of an AISI 52100 steel component. The optimization algorithm selects the optimal feed rate at each N step, restricted by the calculated surface roughness, roundness, and boundary-affected layer. The algorithm also considers the time delay constant due to the normal force τ_F .

In a similar approach, Pereverzev and Akintseva [38] developed a methodology to determine the optimal grinding cycle sequence to reduce grinding time, constrained by n input parameters. This was applied to the internal cylindrical plunge grinding. The method developed by the authors is very similar to a previous publication from Dong [24], a fact that brought into the light that even after a decade of technological advancements, there is still room for improvement of cylindrical plunge grinding of steel components.

The methodology developed by Dong [24] uses a dynamic programmed algorithm, in conjunction with the calculated process inputs to determine the necessary feed rate to achieve the optimized grinding cycle. This methodology is detailed, according to the author, as:

Cycle-time minimization is defined here as a sequential decision-making problem, where the cycle is discretized into a finite number of small steps. Since the total cycle time is unknown, the discrete steps cannot be defined in terms of time. Instead, the total infeed is discretized uniformly into a number of steps with incremental infeed dq [24].

The state of the process is defined at each step. The complete state of the grinding process includes the surface roughness, out-of-roundness, depth-of burn (boundary-affected layer thickness), and the actual infeed rate [24]. The surface roughness input is calculated by the Eq. (3)

$$R_a = R_0 \cdot f_d^x \cdot a_{ed}^y \cdot \left(\frac{\pi d_w v_w}{v_s} \right)^\gamma \quad (3)$$

where:

R_0 , x , y , and γ are empirical constants

a_{ed} is the dressing depth [μm]

f_d is the dressing lead [mm]

The surface roughness constraint can be satisfied by selecting the dressing lead according, given by the Eq. (4),

$$f_d = \left[\frac{R_a}{R_0} \left(\frac{v_s}{\pi \cdot d_w \cdot v_f} \right)^\gamma \cdot a_{ed}^{1/y} \right]^{1/x} \quad (4)$$

To use the DP methodology, the initial and final states of the cycle need to be defined. Because the cycle starts from the idle state, the infeed rate is zero at the first step, and it is determined from the roundness specification for the last step. The out-of-roundness (r) can be calculated, by Eq. (5)

$$r = r_m + v_f/n_w \quad (5)$$

where:

r is the out-of-roundness [μm]

n_w denotes the rotational speed of the workpiece [min^{-1}]

r_m is the residual out-of-roundness [μm]

Therefore, in order to satisfy the roundness constraint, the actual infeed rate at the last step v_f is defined, by the Eq. (6), as

$$v_f = (r_{\max} - r_m) / n_w \quad (6)$$

where:

r_{\max} is the maximum allowed value of the out-of-roundness [μm].

The dynamic programmed algorithm starts from the last step of the cycle and continues backward to the first step. The surface roughness and out-of-roundness constraint are only monitored at the first step (step 1), as this is the characteristic required on the finished part.

At step N-1 through 1, the only constraint monitored is the depth of the burn. For each reachable radial feed rate $v_{N-1,j}$ that satisfies the BAL constraint, the commanded radial feed rate u_j and time t_j to reach step N can be calculated by solving simultaneously the incremental radial feed rate and inverse dynamic equations, represented, respectively, by Eq. (7) and (8)

$$dq = u_j t_j + \tau_F [(u_j - v_{N-1,j}) e^{-t_j/\tau_F} - (u_j - v_{N-1,j})] \quad (7)$$

$$u_j = \frac{v_{fr} - v_{N-1,j} e^{-t_j/\tau_F}}{1 - e^{-t_j/\tau_F}} \quad (8)$$

where,

dq is the discrete step dislocation at each iteration [mm]

u_j is the programmed/commanded radial feed rate [mm/s]

v_{fr} is the actual radial feed rate for the j^{th} iteration [mm/s]

τ_F is the time constant for machine-tool/grinding wheel dislocation [s]

If u_j violates any constraints, the radial feed rate (step) is considered unfeasible.

Finally, at step 1, the total cycle times through each of the feasible are computed and compared. The command feed rates that result in the minimum cycle time from step 1 to step N are determined as optimal.

The depth of burn (z) is calculated due to the grinding power reached during the grinding process. The equations that estimate the grinding power and depth of burn, depicted in Eq. (9) through (14), are

$$P = 0.0138 \cdot \pi \cdot d_w \cdot v_f + 9.62 \times 10^{-7} + 0.842 \cdot (d_e \cdot v_f)^{0.85} v_s \cdot A_{\text{eff}} / (n_w)^{0.85} \quad (9)$$

$$p_s = P / (\pi d_w v_f) \quad (10)$$

$$z = -1.449 \left(\frac{v_w l_c}{4 \cdot \alpha} \right)^{0.37} \cdot \frac{2\alpha}{v_w} \ln \left[\frac{\pi \cdot k \cdot l_c \cdot \theta_{\text{mb}} \cdot v_w}{6.2 \cdot \alpha \cdot \pi \cdot d_w \cdot v_f \left(\frac{v_w l_c}{4 \cdot \alpha} \right)^{0.53} (p_s - 0.45 \cdot u_{\text{ch}})} \right] \quad (11)$$

$$l_c = \sqrt{\pi \cdot d_w \cdot d_e \cdot v_f / v_w} \quad (12)$$

$$A_{\text{eff}} = -0.008 \cdot A_0 \ln(1.4 \times 10^4 m \delta) \quad (13)$$

$$\delta = 1.1 \times 10^{-11} \cdot a_d^{0.75} \cdot s_d^{1.75} \quad (14)$$

where

A_0 is a constant [mm²]

d_e is the equivalent diameter [mm]

l_c is the contact length [mm]

P is the grinding power [kW]

p_s is the specific energy [J/mm²]

α is the thermal diffusivity of the workpiece [m²/s]

A_{eff} is the wear flat area [mm²]

k is the thermal conductivity of the workpiece [W/m·K]

m is a constant

θ_{mb} is the critical temperature for burning [°C]

δ is the equivalent dressing infeed angle [rad]

This method is based on the modeling of the grinding process. In order to avoid the uncertainties derived from a theoretical approach, the study presented in this thesis will consider the surface roughness and the depth of burn as measurable quantities from the experiments. The out-of-roundness values are not factored into this study, even though Dong's [24] model considers it. Aside from these considerations, the step-by-step grinding cycle time optimization procedure using dynamic programming will be the same one as the one elaborated by Dong [24].

The selection of dynamic programming for the logical processing of grinding was based on the premise that, in the planning of grinding experiments, the need for a multi-step

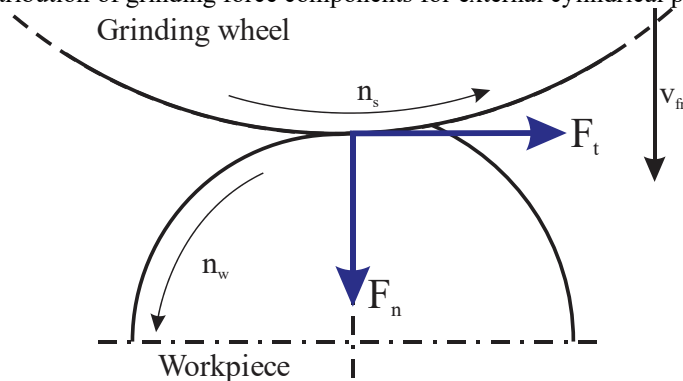
plunge cycle is null. Since in the industry, the parameters would most likely be given by the operator's experience, this procedure digitalizes experience and performs a quicker selection and decision-making.

Therefore, the elaboration of a database with fixed/constant radial feed rates (*i.e.* specific material removal rate) is enough for the elaboration of a plunge cylindrical grinding cycle. However, before this database is built, an awareness of the grinding process inputs is key to obtain reliable and consistent data.

2.1.2 Grinding force and temperature distribution

During the grinding process, the cutting edge exhibits a track-bound engagement, penetrating the workpiece upon a flat path and, after a phase of elastic deformation, triggers a plastic flow of the workpiece material [21]. The interaction of each individual cutting edge generates a force and a reaction force on the grinding wheel and workpiece. This grinding force is separated into three components, distributed along the radial and axial direction, following the feed motion: axial force F_a , tangential force F_t and normal force F_n , depicted in Figure 6. The axial component can be disregarded during the plunge motion, as there is no dislocation in that direction.

Figure 6 – Distribution of grinding force components for external cylindrical plunge grinding.



Source: Adapted from Klocke [21].

The energy needed for material deformation, chip formation, and material removal is quantified by the actual mechanical load (grinding force F) during the process. It is estimated that energy consumption in grinding is between 25 and 40 J/mm³, ten times higher than the energy consumption in the turning process [39, 40].

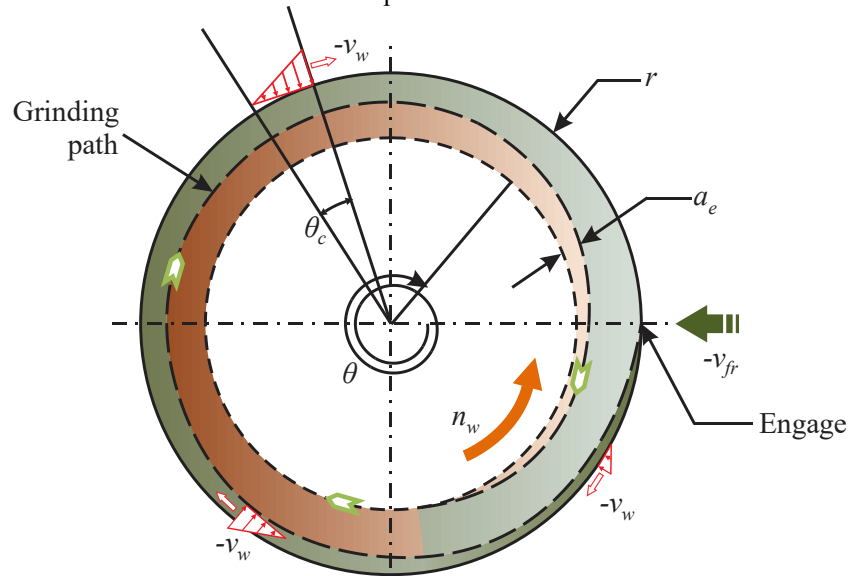
The largest amount of energy introduced to the grinding process is converted to heat by plastic deformation of the workpiece material, friction between the platform flank of the grit

with the workpiece material; friction between the chip and the face of the grit; and friction between the chip and the binder [40].

Due to the fact that part of the plastically deformed material is not converted to a chip, approximately 55% of the mechanical energy involved during chip formation is transferred to the workpiece, while 45% is transferred to the cutting fluid, the chip, and the environment [23, 41]. Once the machining system (grinding wheel, machine-tool, workpiece material, dressing conditions and cutting fluid) is set up, the temperatures in grinding will depend on the cutting parameters [21, 39].

A usual model that conveys the grinding temperature considers an approximation of the grinding wheel contact geometry, moving heat source theory for a triangular heat flux distribution, confined to a small wheel-workpiece contact zone. Due to the enclosed volume of material removal experienced during cutting, it is expected large gradients of temperature. In the case of cylindrical plunge grinding, it is important to consider the spiral trajectory of the grinding wheel on the workpiece, as well as that the depth of cut a_e may vary along the process, which leads to a non-constant temperature field on the workpiece, as shown in Figure 7 [36, 42]. In steel components, high temperatures can be a problem.

Figure 7 – Variation of the depth of cut and temperature in external plunge cylindrical grinding. Color shades indicate temperature distribution.



Source: Nguyen and Zhang [36].

For example, Ueda *et al.* [43] performed scratching experiments, employing a single conical tool of Si_3N_4 on different metallic workpieces (manufactured in medium carbon steel, titanium, molybdenum, and tungsten), and measured the tool tip temperature. A temperature

reduction from 1500 to 300 °C observed by the authors took around 2 ms for steel (around 6×10^5 °C/s), which is enough to cause martensite transformation on the steel structure.

2.2 ALUMINUM OXIDE GRINDING GRITS

Crystalline aluminum oxide (Al_2O_3), also known as corundum or alumina, is obtained through several manufacturing processes from the natural purified bauxite. The Al_2O_3 phase mostly applied in industry is the rhombohedral crystalline α - Al_2O_3 phase, with higher density and higher thermal conductivity than the γ - Al_2O_3 , exhibiting a proportion of covalent atom bonds to ionic atom bonds of 40–60 % [20].

One way to produce corundum is the application of an electric arc. The so-called electric fused corundum or electro-corundum can be divided into grades of white (core), brown and normal corundum (crust of the produced block); sintered bauxite and sol-gel (also known as microcrystalline (MC), seeded gel or SG) corundum belong to the group of sintered corundum materials [21].

The sol-gel corundum was first applied as an abrasive grit in the early 1980s. With the development of the new generations of microcrystalline sintered corundum produced with the sol-gel technology, it is now possible to obtain a sub-micron Al_2O_3 powder [13]. In the beginning, sol-gel corundum was used as the solitary abrasive grit type in grinding wheels (grit volumetric fraction of 100%). However, its higher toughness and grit-binder anchorage led to excessive grinding forces. Nowadays, typical blends consist of 10 to 50% of sol-gel corundum content in a white corundum or monocristalline (MN) corundum main structure [20].

2.2.1 Production of white fused and sol-gel aluminum oxide

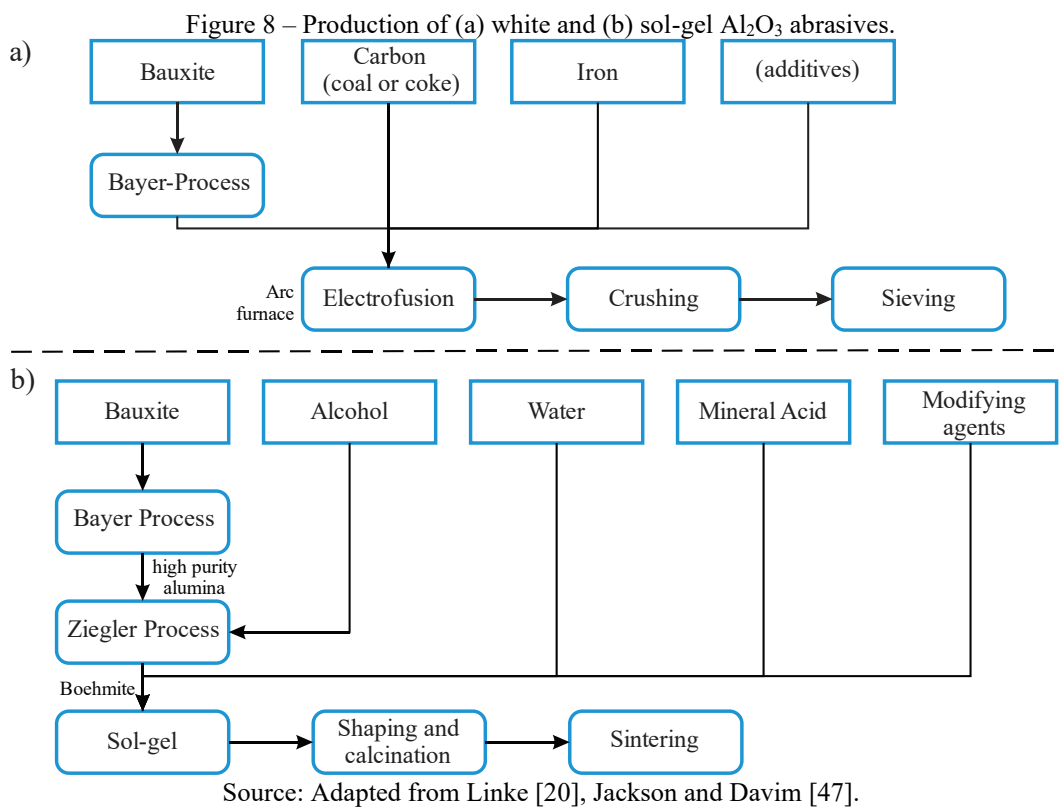
The production method distinguishes white fused and microcrystalline sintered corundum (sol-gel aluminum oxide). The usual manufacturing route to produce white fused aluminum oxide is performed by calcinating or purifying the bauxite by the Bayer process and electro-fusion in an electric arc Higgins furnace. The pre-processed bauxite is fused with carbon (from coke or coal), metallic iron, and other additives. The fused corundum block is then crushed and sieved [21, 44].

The manufacturing of sol-gel aluminum oxide is a longer and more expensive route. Bauxite is purified by the Bayer process and then transformed through the Ziegler process into boehmite. Powdered boehmite (γ - AlOOH) is transformed into a clear sol by mixing with water.

Modifying agents (grain growth inhibitors or nucleating agents) and a peptizing substance (usually nitric acid) are added, obtaining a colloidal solution of boehmite particles dispersed in a fluid called sol. Next, nitric acid, or a nitrate solution, is added to the sol in order to obtain a gel through dehydration and polymerization. The nitric acid is, on the one hand, used as a peptizer in the creation of sol and, on the other, to form a gel. The resulting sol-gel is shaped, calcinated, sintered and, lastly, sieved [13, 20, 21].

The series of topotactic transformations of the boehmite into a thermodynamically stable phase, the α - Al_2O_3 polymorph is as follows [44]: Boehmite $\rightarrow \gamma \rightarrow \delta \rightarrow \theta \rightarrow \alpha$ - Al_2O_3 .

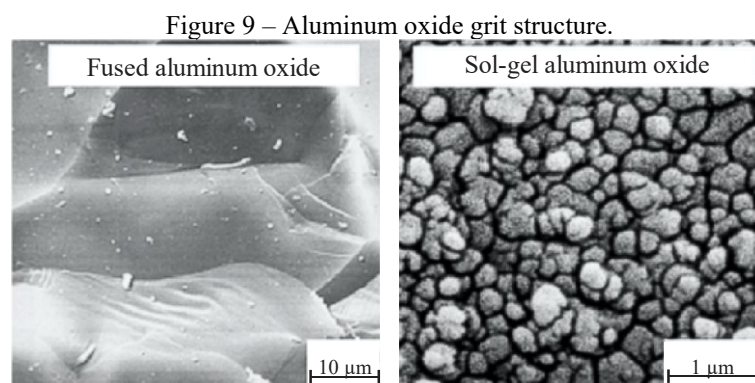
Figure 8 summarizes the methods for obtaining white fused and sol-gel Al_2O_3 abrasives.



The main differences between the two routes, and therefore, grits are that the white fused Al_2O_3 requires crushing of the blank and further sieving before employing as an abrasive grain. The generated crystallites through the sol-gel process present a size of about $0.2 \mu\text{m}$ or less. These crystallites are sintered to obtain the final grit, eliminating the need for crushing [45-46]. Sol-gel manufacturing allows a much greater manipulation and control of grain shape, as shown in MC grits with elongated shapes [47].

2.2.2 Properties of aluminum oxide grits

Considering the manufacturing chain for the aluminum oxide presented in section 2.2.1, it is expected that the properties of each type of Al_2O_3 grits are different. The main differences in the property variation are due to different manufacturing routes. During wear, for instance, the monocrystalline electro-fused aluminum oxide breaks along preferred cleavage planes, whereas sol-gel Al_2O_3 breaks along with the sintering interface, which obtains grains with a bulky surface due to the crystallite (sub-grain) structure [20], as depicted in Figure 9.



Source: Adapted from Klocke [21].

Although sol-gel aluminum oxide grain is structured by several crystallites bond during the sintering process, it is not considered a polycrystalline structure, but a microcrystalline abrasive grit. Fused aluminum oxide grits, on the other hand, are considered to be either monocrystalline or polycrystalline [19, 46].

The microcrystalline structure of a sol-gel abrasive grain affects especially its friability, hardness, toughness, self-sharpening, and specific wear behavior properties since the preferable crack propagation follows the intergranular sintering interface rather than preferable crystallographic planes of the fused aluminum oxide. Table 1 lists a few properties, among others.

Microcrystalline sintered corundum is characterized by similar hardness and greater ductility than fused alumina oxide grains, which translates into greater resistance to brittle fracture [46].

The increase in performance observed in many cases using grinding wheels with microcrystalline Al_2O_3 was attributed by some authors to the higher toughness of this type of grain. Other authors consider the effect of micro-fragmentation as an essential feature [19]. In any case, the wear behavior of sol-gel abrasives is a topic subject of discussion.

Table 1 – Composition and properties of white fused alumina and microcrystalline sintered alumina abrasives.

Full name	White fused alumina	Microcrystalline sol-gel sintered alumina
Chemical composition	Al ₂ O ₃ 99.7%, SiO ₂ 0.01%, Fe ₂ O ₃ 0.02% Na ₂ O 0.16% CaO + MgO 0.02%	Al ₂ O ₃ 95-99% MgO/Fe ₂ O ₃ 0-5%
Crystal size [μm]	> 10	< 1
Shape	Pointed, sharp	Pointed, very sharp
Specific density [g/cm^3]	3.96	3.87
Knoop hardness HK [GPa]	20.3	21.5
Ductility [$\text{MPa}\cdot\text{m}^{1/2}$]	2.0	3.7
Critical stress intensity factor K_{IC} [$\text{MPa}\cdot\text{m}^{1/2}$]	2.7	3.5 - 4.3
Coefficient of friction (hardened steel)	0.34	0.19
Thermal conductivity coefficient α [$\text{W}/\text{m}\cdot\text{K}$]	27-35	-

Source: Brunner [19] and Nadolny [46].

2.2.3 Wear of aluminum oxide grinding wheels

Grinding wheel wear concerns two scales: micro-wear, considering as such the phenomena that alter the abrasives structure and therefore wheel's initial topography (obtained after conditioning); and macro-wear, which alters the macro geometry of the grinding wheel, *i.e.* radial reduction and profile modification [21]. In a sense, shifting from micro to macro-wear is a continuous process, as well as exhibiting a simultaneous occurrence.

Micro-wear, mainly referenced as grit wear, begins in the outer crystalline layers of the grit. Extreme cyclic pressures, shearing forces, shearing force gradients, temperatures, and temperature gradients initiate crack and crack propagation in the surface layers of the single grits of the grinding wheel, decreasing the abrasion resistance of the grit material. These softened layers are removed by mechanical abrasion. In this way, new crystalline layers are constantly exposed to wear [21].

The wear of a grit starts on a small contact area at the summits of the grains, flattening this region. This flattening process increases the normal force on the grit up to the limit of the mechanical resistance of the embedded grit, leading it to fracture and further breakage. The flattening of the grit is the micro-wear and the breaking of the grits is the beginning of the macro-wear. But there is not an exact limit between the micro and macro phenomena [46].

The mechanisms that govern wear, based on existing literature and compiled by Nadolny [46] are:

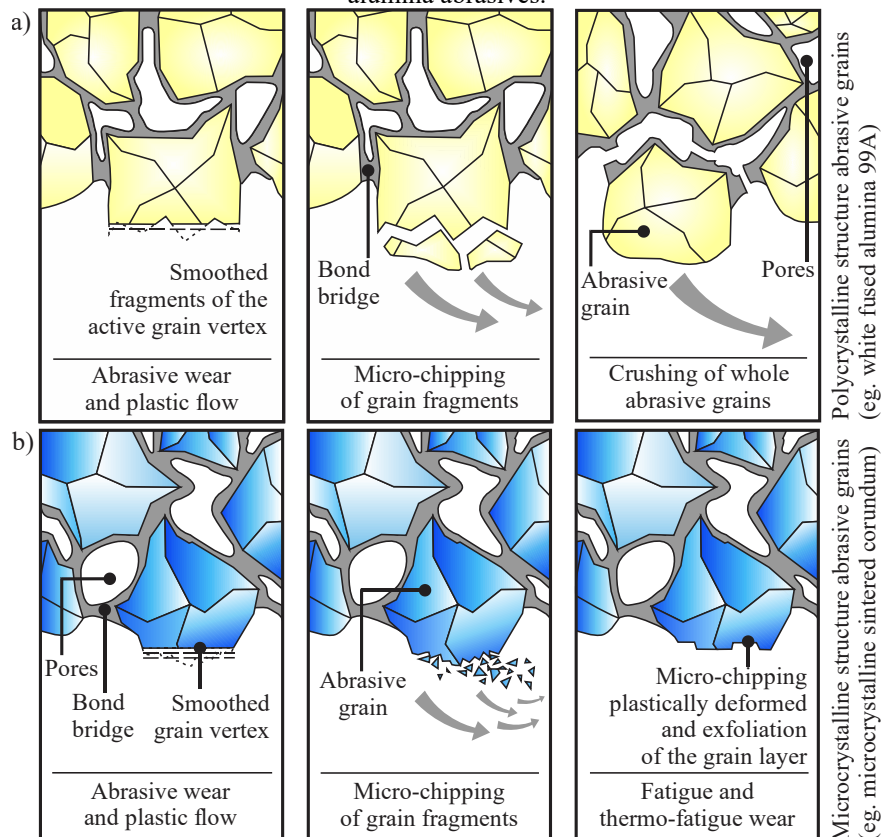
- a) Abrasive wear of the active abrasive grains vertexes (micro);

- b) Abrasive wear of the bond in the areas of contact with the machined material (micro);
- c) Fracture wear of the abrasive grains due to mechanical and thermal shock loads (micro, the beginning of macro);
- d) Fracture of bond bridges (macro);
- e) Fracture at the interface between abrasive grain and bond bridge (macro); and
- f) The smearing of the grain vertexes and intergranular free spaces with the machined material.

These phenomena act simultaneously on the grinding wheel active surface and cause several wear types, referred to as grit dulling and flattening; micro-breakage/splintering; grit breakage; bonding breakage; material and chip adhesion [14, 21, 46].

Considering the wear phenomena on sol-gel and electro-fused grits, the basic mechanisms are similar, but the crack propagation is substantially differential. In terms of abrasive grit types, wear proceeds as the schematic representation shows, in Figure 10.

Figure 10 – Grain breakdown models in grinding wheels with (a) polycrystalline and (b) microcrystalline alumina abrasives.



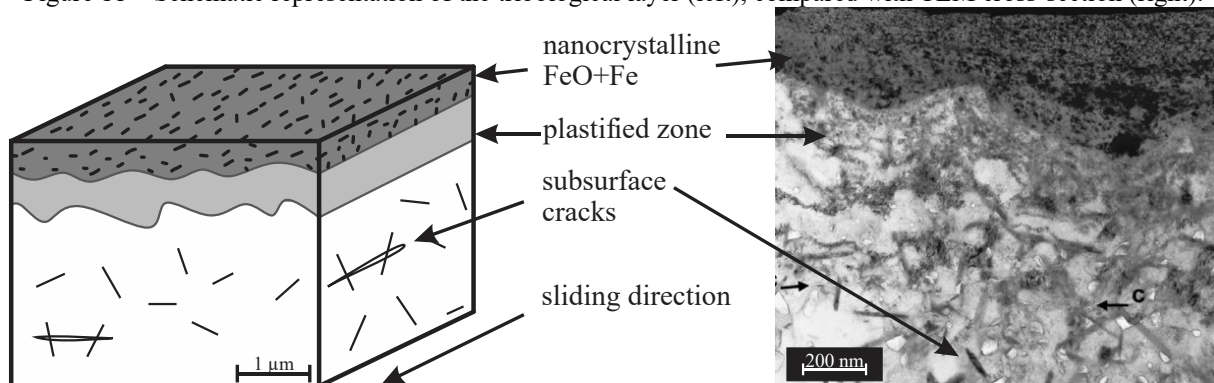
Source: Adapted from Nadolny [46].

In terms of wear progression, the macro cracking of the monocrystalline leads to faster macro wear of the wheel than the macro wear observed for SG wheels.

The abrasion caused by grit's friction on the material and plastic flow of the outermost grit crystalline layer induces, on both types of aluminum oxide, a flattening of the grit surface observed as smoothed fragments of the active grain vertex.

This is especially true for microcrystalline structures, as detected by Klocke *et al.* [48]. The authors observed, after tribological tests of single grains, a very smooth and wavy interface between the sol-gel aluminum oxide and the debris layer, indicating high-temperature plastic flow rather than surface cracking. Evidence of a homogeneous microstructure of nanocrystalline FeO/Fe layer smeared on the surface was found (Figure 11), related to high temperatures on the zone and responsible for friction coefficient reduction.

Figure 11 – Schematic representation of the tribological layer (left), compared with TEM cross-section (right).



Source: Adapted from Mayer *et al.* [49].

Owing to the high densities of grain boundaries, pores and the presence of second phases, the thermal conductivity of sol-gel corundum is lower than that of fused corundum. The higher concentration of imperfections in sol-gel corundum reduces the mean optical path length of the phonons (fundamentals packets of energy exchanged during lattice vibrations), resulting in lower thermal conductivity and, therefore, increased temperature in the cutting interface leading to metallurgical transformations of the workpiece. It can be assumed that the lower thermal conductivity of Sol-Gel corundum in comparison with that of fused corundum is a decisive factor in the occurrence of the wear mechanisms observed [48-49].

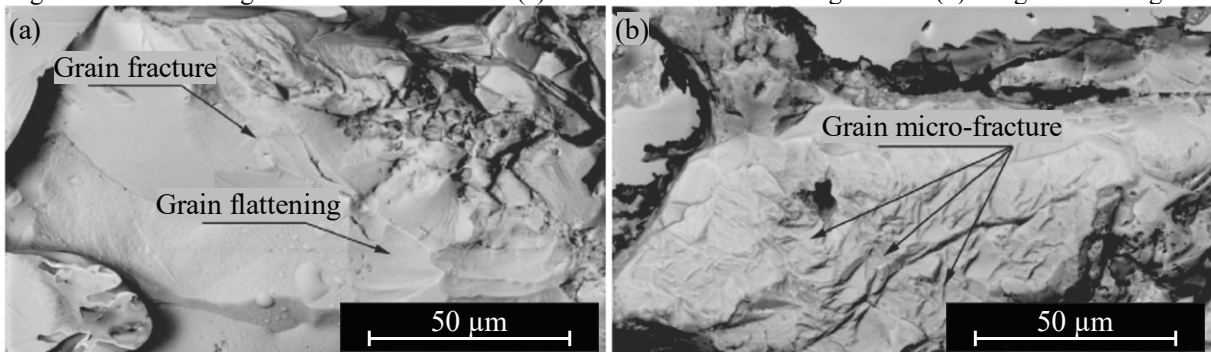
The lower thermal conductivity of sol-gel corundum compared to white corundum promotes a faster activation of plasticization mechanisms by sliding, creep or grain boundary sliding. Furthermore, a higher amount of energy is available for the activation of tribochemical reactions in the near-surface regions. Therefore, it can be concluded that reduced heat conductivity has an additional positive impact on the wear mechanisms [49].

Micro-chipping of grain fragments, caused by severe mechanical load and/or mechanical and thermal fatigue leads to removal of sections of the grain surface, and thus, renewal of the cutting capacity. For white fused alumina, crack propagation follows the crystallographic borders of large-sized grains. Whilst in the case of microcrystalline grains, the chipping usually occurs only in micro-crystals, along with the sintering interface, revealing smaller and sharp cutting edges [14, 46].

As the depth of cut increases, the mechanical load on the abrasive grain increases. Therefore, when the load overcomes bond resistance, the fracture of grits occurs [14].

The differences in grit fractures, comparing white fused with sol-gel alumina were observed by Fathallah *et al.* [16] in their studies. The authors evaluated the wear of conventional grinding wheels composed of 100% white fused alumina and 100% sol-gel alumina, applying different cooling methods. Overall, the results show the superior wear resistance of sol-gel alumina when subject to higher cutting depths. The differences in grit wear between the two tested abrasives are depicted in Figure 12.

Figure 12 – Abrasive grains wear mechanisms: (a) aluminum oxide abrasive grain and (b) sol-gel abrasive grain.



Source: Adapted from Fathallah *et al.* [16].

With increasing cutting depth, as evidenced in Fathallah *et al.* [16] studies, and maintaining the circumferential workpiece speed v_w , the specific material removal rate Q_w increases. This leads to a higher mechanical load and, therefore, more heat generation in the cutting zone.

As a consequence of the continuous micro-wear, the grinding wheel macro-geometry, *i.e.* diameter and profile, deteriorates by the macro-wear. There are two main characteristics associated with the macro-wear: radial (Δr_s) and edge (Δr_{sk}) wear, that may appear combined or not. From the radial wear, a tool lifespan parameter, grinding ratio G , can be determined by the Eq. (15),

$$G = \frac{V_w}{V_s} \quad (15)$$

where:

V_w is the volume of removed material [mm^3]

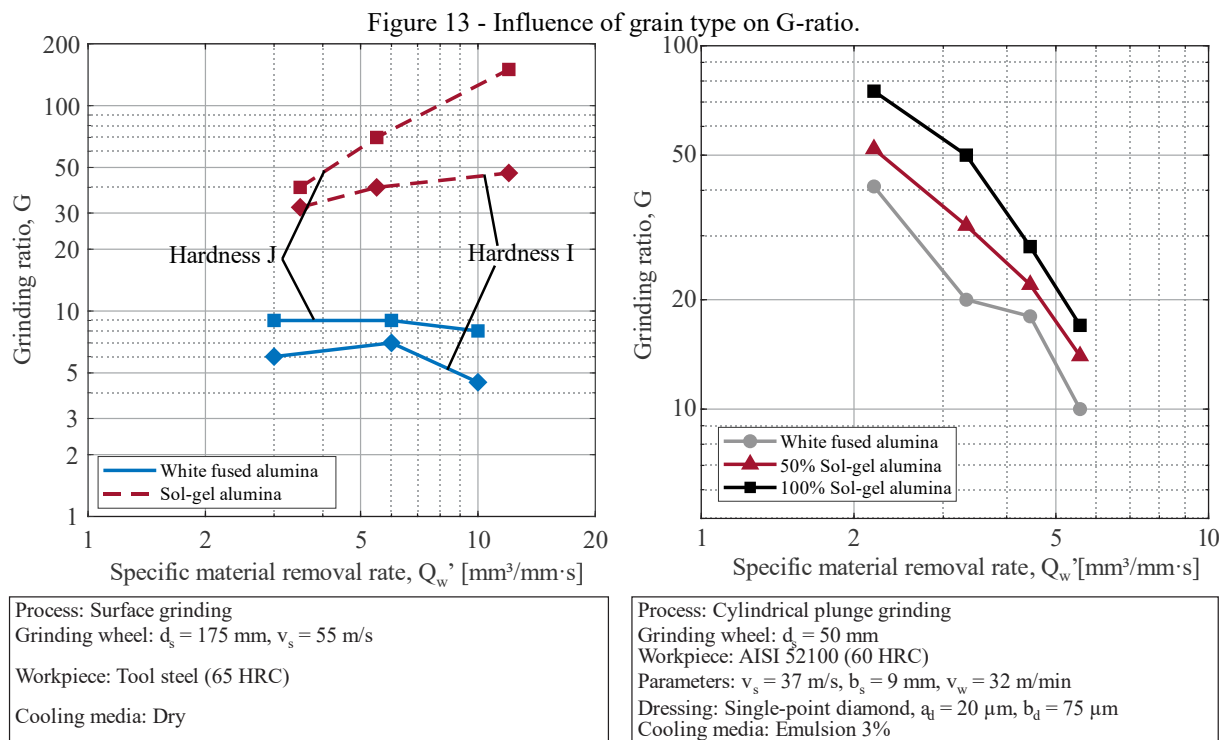
V_s is the grinding wheel wear volume [mm^3]

This ratio is highly affected by the input parameters, *e.g.* abrasive type and specific material removal rate.

Lindsay [50] compared the G-ratio of sol-gel (SG) and white fused alumina (WFA) grinding wheels on surface grinding of tool steel. As expected, the higher wear resistance of sol-gel grinding wheels yielded several times higher G-ratio. Information on the grinding wheels structure (pores, binder, and abrasive content) and composition (white fused alumina and sol-gel alumina) were only differentiated by the manufacturer's specification.

In a similar approach, Eranki *et al.* [51] evaluated the effect of an increased concentration of sol-gel alumina versus the white fused alumina on the G-ratio. The information of the grinding wheel structure was also only referenced by the manufacturer's specifications.

Figure 13 illustrates the results obtained in both studies.



By increasing the cutting severity (higher specific material removal rates Q_w'), the wear shifts faster from micro-wear to macro-wear. At low Q_w' , the micro-wear share increases due to the high specific thermal and mechanical stresses. At higher Q_w' , wear behavior is primarily determined by increasing mechanical stress [21].

The grinding wheel wear determines the grinding cycle tool life. At the end of a single life cycle, the grinding wheels must be conditioned to guarantee the required aspects of the workpiece. This conditioning process is composed of shaping and sharpening of the grinding tool. In conventional grinding, tool shaping, and sharpening is done simultaneously and is named “dressing”.

The total lifetime of a grinding wheel is determined by the possible decrease of the diameter of the grinding wheel on a specific machine tool.

Due to the low-cost of Al_2O_3 abrasives (in comparison to cBN and diamond), the entire grinding wheel bodies are made of Al_2O_3 abrasives, binders, and pores, which leads to higher total grinding wheel's lifespan. Therefore, the dressing aspects of such grinding wheels must be considered.

In this context, Yamauchi and Ueda [52] evaluated dressing forces of conventional grinding wheels with different abrasive types (white fused and sol-gel aluminum oxide) and hardness ranges from H to K. The grinding wheel information was based only on the manufacturer's specification. The normal dressing force was superior for sol-gel abrasives for all tested conditions. The authors measured an increase of 10 – 20% on the normal dressing force in comparison to white fused Al_2O_3 .

Similar results were observed by Cinar (1995) *apud* Wegener *et al.* [53], where the dressing normal force was superior for sol-gel abrasive based grinding wheels. This behavior is associated with the higher toughness and ductility, as well as a higher critical stress intensity factor, which increases the minimal force necessary for micro-fracture to take place.

2.3 SURFACE INTEGRITY

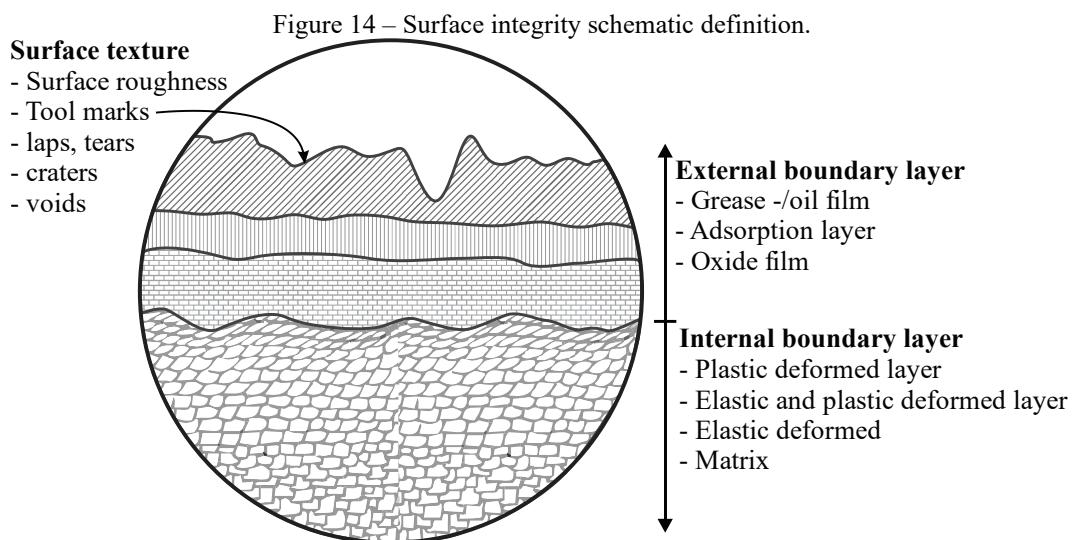
The full importance of the field of surface integrity in the industry is not acknowledged. Designers and process engineers frequently lack information about the needs of surface quality and the knowledge on how to select the appropriated processes and parameters to achieve the manufacturing requirements. In addition, since the impact of the surface integrity on the mechanical properties of a machined component is unknown, its surface requirement is only specified for higher quality. The damage extension as a result of the former steps in the

manufacturing process chain is not fully known and often not considered, which may implicate a lower lifespan of the component [54-56].

The term “surface integrity” (SI) was first introduced in 1964, by the researchers Field and Kahles [57], in an industrial report. In this publication, the authors defined surface integrity as: “inherent or enhanced condition of a surface produced in machining or other surface generation operation”. To Griffiths [58], the term is defined as: “the topographical, mechanical, chemical and metallurgical 'worth' of a manufactured surface and its relationship to functional performance.” Davim [55] established that surface integrity is defined as: “The topographic, mechanical, chemical or metallurgical state of a machined surface and its relationship with functional performance.”

However, some authors define surface integrity as mainly as the effects on the subsurface of a machined component. Hereby, in order to avoid semantic discussions, surface integrity definition in this study will encompass the surface and subsurface effects and modifications. It is composed primarily by the surface texture; and by “boundary-affected layer”, term based on the definition of boundary layer introduced by König and Klocke [20, 61], as well as Brinksmeier and Walter [62] and defined as “the mechanical, chemical, thermal or metallurgical state of a machined subsurface and its relation with the functional performance”. This term, although similar, should not be misinterpreted with the term “boundary layer” employed in fluid mechanics.

The surface texture and boundary layer can be, therefore, characterized by several effects that occur on the surface and subsurface layer, as depicted in Figure 14.



Source: Adapted from König *apud* Boehs [59] and Klocke [60].

Since grinding is usually the last manufacturing process in the production chain, the surface quality and integrity are a subject of interest, especially when considering high specific material removal rates during rough grinding. Thereby, the effects of high specific grinding rates Q_w' and different abrasive compositions of grinding wheels, will be the focus and subject of analysis in this study.

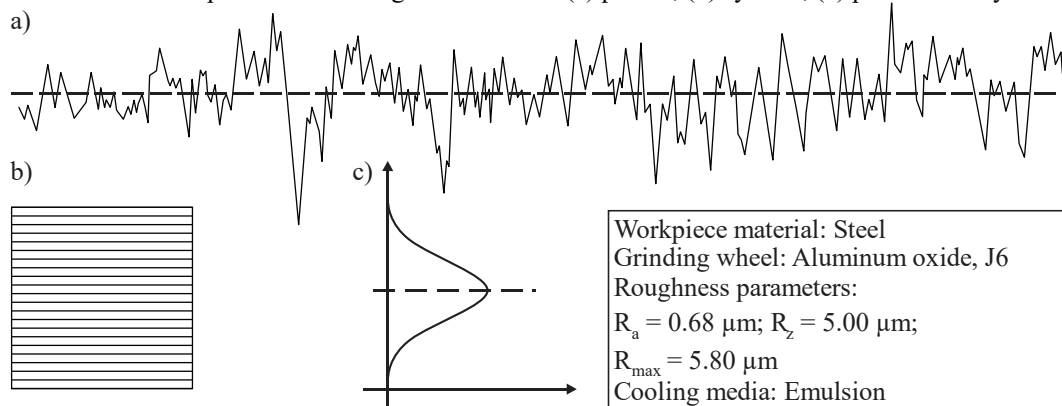
2.3.1 Surface texture of ground components

In the past, the surface texture was considered only a characteristic of a machined surface, with measurable quantity. Currently, it is regarded as a fundamental characteristic in the manufacturing control, to the functional performance and quality control [63].

Overall, the surface texture is characterized by the surface profile, which encompasses only the roughness profile (suppressing the waviness and longer wavelengths by the profile filter λ_c). Usually, the evaluations of the roughness are related to a profile (1 dimension), however, with the advent of newer measurement methods, the areal (2 dimensions) evaluation is now accessible [64].

In grinding, the organization of the surface features is stochastic in its nature, where the grinding wheel surface is characterized as an isotropic stochastic surface and the ground surface texture characterized as an anisotropic stochastic surface. Ground surfaces are stochastic in relation to the periodicity, but within an expected normal distribution of peaks and valleys, as depicted in Figure 15 [63].

Figure 15 – Schematic representation of a ground surface: (a) profile, (b) symbol, (c) peak-to-valley distribution.



Source: Adapted from Jiang and Whitehouse [64], Noppen *et al.* [65]

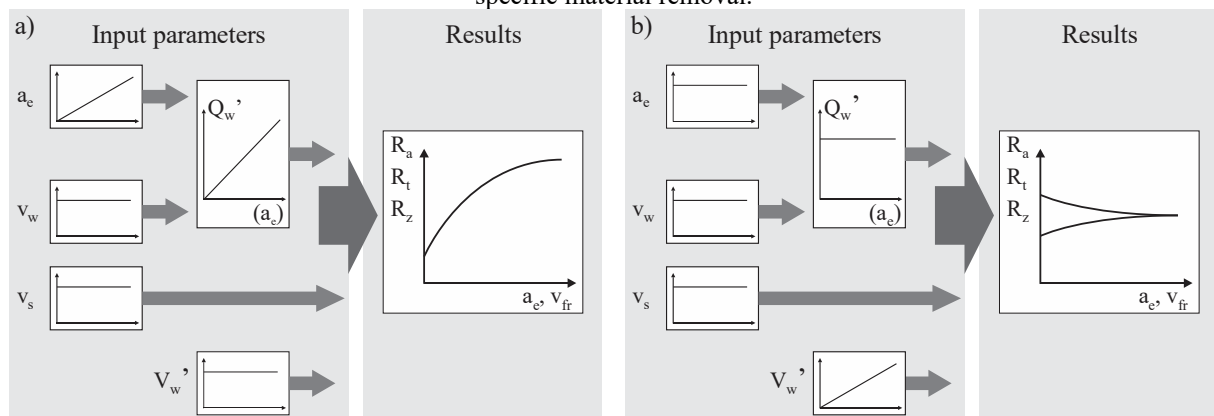
The digitalized roughness profile, if treated as a family of points, permits the extraction of a large quantity of profile and area parameters, each with distinct definitions and applications.

But the most employed parameters to represent the surface texture of a ground workpiece in industrial applications still are: the maximum profile height R_t , the arithmetic mean of the maximum profile height R_z combined with R_{max} , and the arithmetic mean profile height R_a ; and nowadays their areal counterparts, S_t , S_z , and S_a . To characterize the grinding wheel profile, the grinding wheel effective roughness R_{ts} is defined as the component roughness obtained for a defined rotational relationship between the grinding wheel and the workpiece rotation (3/1 to 5/1). The R_{ts0} is used to characterize the effect of dressing the grinding wheel on the workpiece topography [21].

Recently, the roughness measuring equipment with high computational processor integrated features permit to directly inform interesting information, such as the symmetry of the surface on the mean line R_{sk} , which characterizes the wear state of the grinding wheel, as observed by Marra [66].

Considering the grinding process' input parameters, Klocke [21] described in his publication the influence of those parameters on the surface roughness. Since the focus of the present study is the specific material removal rate Q_w' (a function of the depth of cut a_e), specific material removal V_w' and grinding wheel abrasive type. Figure 16 illustrates the effects of the input parameters, Q_w' and V_w' , on the surface roughness.

Figure 16 – Influence of the input parameters on the surface roughness: (a) specific material removal rate, (b) specific material removal.



Source: Adapted from Klocke [21].

Increasing the grinding rate Q_w' (Figure 16a), accounted by increasing the depth of cut a_e , leads to an expected increase in chip thickness. With the increase of a_e , it is expected an increase in the roughness. This increase is slow because the number of active cutting edges in the cutting region also increases. The momentary cutting edge quantity, as the depth of cut increases, also increases due to the rising contact length. The chip cross-sectional area and thus

the load on each grit also increases with the depth of cut, up to a maximum of the most protruding grit [21].

During grinding, increasing the ground volume V_w' , with the change in wheel topography (Figure 16b), there are two observable behaviors of the surface roughness. If the effective surface roughness R_{ts0} of the grinding wheel is large (aggressive dressing), and the specific grinding rate Q_w' is small, the micro-wear dominates the wear of the grinding wheel. The most protruding cutting edges reduce their height, the number of kinematic edges increases and the roughness parameters reduce over time. As a result, the workpiece roughness is also reduced and asymptotically approaches a boundary value [21]. On the other hand, if the effective initial surface roughness R_{ts0} is low and Q_w' is high, due to higher forces acting on the grains, macro-wear phenomena dominate, grains break out and the number of kinematic cutting edge reduces, which leads to an increase on the surface roughness. Optimal dressing would lead to stable roughness behavior.

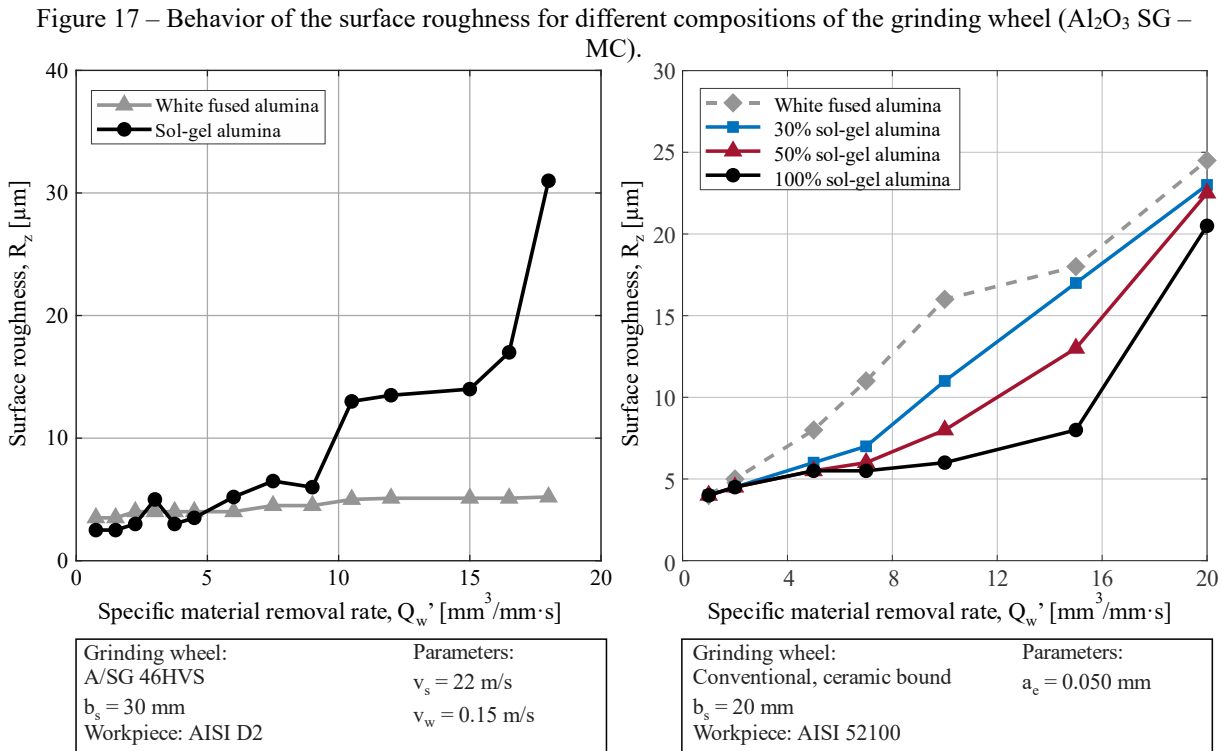
Considering the abrasive grit type, mainly the white fused and sol-gel Al_2O_3 , differences in the wear of these abrasives have been outlined in many studies. Different wheel compositions lead to different wear mechanisms and consequently, changes on the wheel topography and surface texture of the ground workpiece.

For instance, Mayer *et al.* [49] evaluated the effect of microcrystalline Al_2O_3 concentration in grinding wheels (0%, 30%, 50%, 100%), for surface grinding of an AISI 52100 steel. The experiments were performed with discrete steps increasing the specific material removal rates. In a similar approach, Fathallah *et al.* [16] investigated the effect of the abrasive type (white fused alumina and sol-gel alumina) in plunge surface grinding of AISI D2 steel. Figure 17 depicts the behavior of surface roughness for the experiments realized by Fathallah *et al.* [16] and Mayer *et al.* [49], respectively.

The results of the studies of Fathallah *et al.* [16] show that the surface roughness increases when shifting from white fused alumina to sol-gel alumina. Fathallah *et al.* [16] explain that this is related to the verified wear mechanism. The higher occurrence of micro-fractures and, therefore, the generation of newer cutting edges favors the increase in surface roughness. White fused alumina wheels presented a high presence of grain flattening, lowering the surface roughness but negatively impacting the grinding force.

The results obtained by Mayer *et al.* [49] are in total disagreement with the results of the ones obtained by Fathallah *et al.* [16]. For low Q_w' (below $2 \text{ mm}^3/\text{mm}\cdot\text{s}$), the influence of sol-gel concentration can be neglected. However, with the increase of Q_w' , the superior performance of the sol-gel corundum is explicit. The authors relate this behavior to the

significant lower wear rates as the concentration of sol-gel corundum increases, therefore, maintaining a stable cutting and lesser grit fracture, which in turn leads to surface roughness maintenance [49].

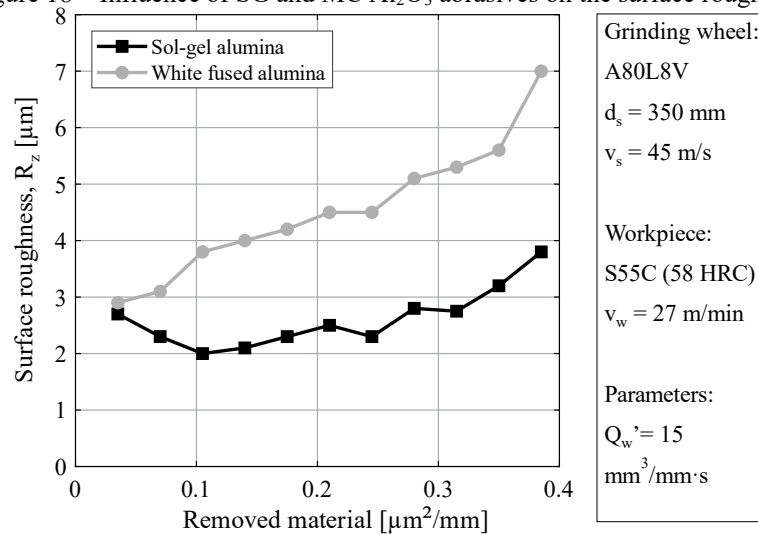


Source: Adapted from Fathallah *et al.* [16] and Mayer *et al.* [49].

Kitamura and Gotanda [67] compared sol-gel aluminum oxide grinding wheels with MC aluminum oxide grinding wheels in surface grinding of AISI 1055 steel. The authors evaluated the grinding force, surface roughness, residual stress, and grinding ratio, with increasing stock removal V_w' (Figure 18).

The results show an increase of surface roughness with an increase in removed material for the white fused aluminum oxide, reaching its roughness peak at the end of the experiments. The sol-gel aluminum oxide showed an irregular behavior, increasing and decreasing the surface roughness magnitude, reaching the maximum value, at the end of the process, but a lower value as the one obtained for MC Al_2O_3 . These results are in accordance with the results obtained by Mayer *et al.* [49].

The studies analyzed previously presented only the grinding wheel specification provided by the grinding wheel manufacturer. The lack of consistency between the different studies is possibly related to incomplete information of the manufacturer's label following the grinding wheel normative.

Figure 18 – Influence of SG and MC Al₂O₃ abrasives on the surface roughness.

Source: Adapted from Kitamura and Gotanda [67].

2.3.2 Boundary-affected layer in ground steels

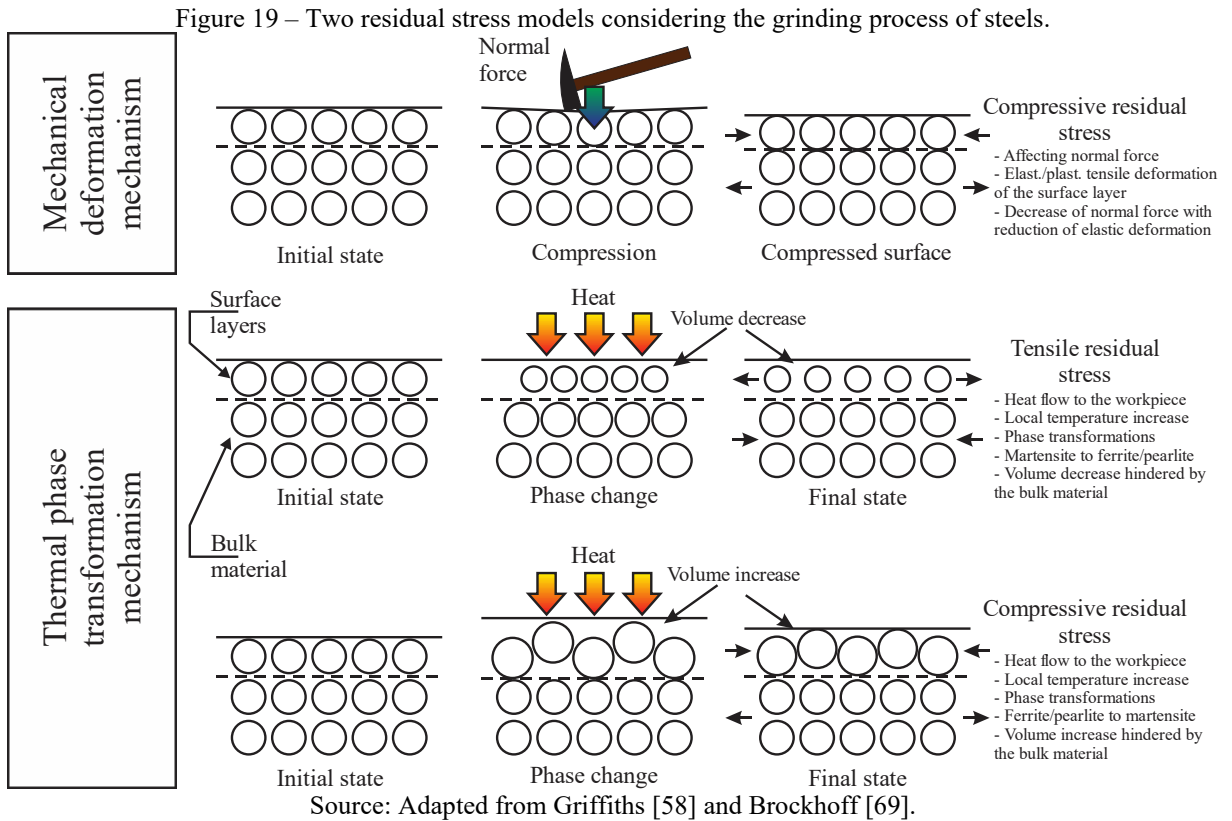
The material removal mechanism in grinding, briefly mentioned in section 2.1.2, directly affects the subsurface modifications and transformations. The hydrostatic pressure and the relative movement of the cutting edge in relation to the workpiece material in the grinding process lead to severe plastic deformation. The high temperature due to internal and boundary friction in the cutting region also leads to several transformations and modifications of the workpiece material structure. The influence of the material removal mechanisms and process severity (input parameters) play an important role in energy generation and thus different subsurface alterations. These changes appear under several forms, as listed [58]:

- a) phase transformations;
- b) plastic deformation;
- c) burr;
- d) cracks;
- e) discontinuities;
- f) tool adhesions;
- g) recast and redeposited material;
- h) residual stress (σ_r); and
- i) strain hardening and recovering.

One of the main aspects that involve the boundary-affected layer (BAL) of machined steels is the changes in the affected surface, which introduces residual stresses. In most cases, the iron-carbon diagram gives a possibility to explain material behavior. The characteristics of

a ground surface are affected by the initial microstructure, carbon content and alloying elements [68].

Griffiths [58] elaborated on a diagram (Figure 19) which considers three phenomena acting on the manufacturing process and the resulting residual stress. This diagram can also be applied to the grinding process and explain the local microstructure alterations.



The mechanical deformation mechanism, depicted in Figure 19a, represents pure mechanical energy applied to material removal. The instantaneous shear force acts removing material and promotes an intense plastic deformation, caused by the abrasive grit dislocation. Since the applied grinding force F has a normal component directed to the machined surface, the introduction of an initial compression on the surface is apparent.

The plastic deformation observed occurs when shearing forces exceed the yield strength of a material. In ductile materials, this deformation leads to plastic flow, producing cracks, voids, build-up edge, and burrs. In extreme cases, it can lead to fragmentation of the adjacent grains to the surface, experiencing that no structure can be observed, also referenced as the white layer [58]. On the metallurgical standpoint, plastic deformations are discordance dislocation due to shearing stress [70].

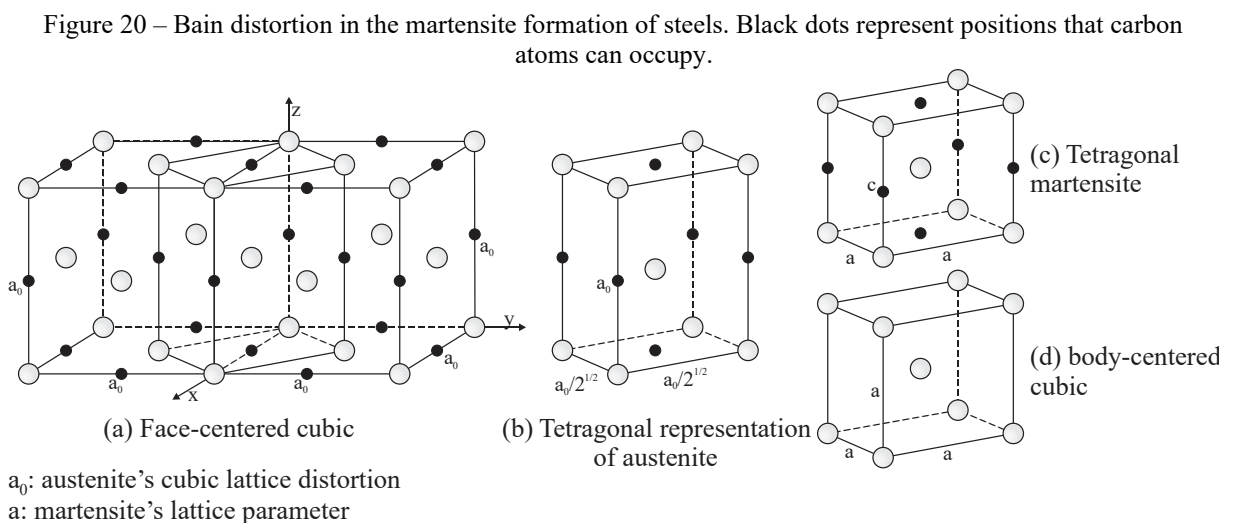
The second model, depicted in Figure 19b illustrates the effect of the intense heat generation of the process, associated with mechanical energy/friction converted into heat and dissipated on the workpiece (consider reviewing section 2.1.2 for reference).

If the heat from grinding is introduced rapidly enough, the surface temperature of the workpiece may rise to the point where tempering can occur beyond the degree imposed by prior heat treatment (overtempered martensite – OTM), commonly referenced as a dark layer. Higher the hardness of the steel part being ground, the more important this type of damage becomes [71-72].

If more heat is generated, the steel structure near the surface may be heated to a temperature high enough for the structure to be re-austenitized and quenched to untempered martensite (UTM) and retained austenite (RA).

Such rehardening and overtempering beneath the surface are accompanied by dimensional changes that can alter the distribution of residual stresses as well as changing the physical properties of the steel undergoing transformation, and in most cases influencing the fatigue life of components [73-74]. Such effects are especially influenced by high temperatures, carbon and alloy element content [26]. In the case of medium and high carbon hardened steels, this untempered martensite plus retained austenite layer is often referenced as a white layer, due to the blank appearance under microscopy, even after chemical etching [55, 58, 75].

The driving force for a martensite reaction during the quench heat treatment is the free energy difference when reducing the temperature, below the equilibrium temperature, from austenite (Fe- γ) to a ferrite (Fe- α) stability phase ranges (Figure 20).



Source: Adapted from Abbaschian *et al.* [70].

The phase change that occurs in a martensite transformation is brought about by the movement of the interface separating the parent phase from the product. As the interface moves, atoms in the lattice structure of the parent phase are realigned into the lattice of the martensite phase (Fe- α'). Because of the manner in which martensite forms, no composition change occurs (diffusionless phase transformation). The atomic realignments associated produce shape deformations [70].

The transformation in martensite depends on rapid cooling (100 – 500 °C/s) and maintaining the temperature in the martensite formation region, specified on the temperature-time-transformation diagram in between the martensite start (M_s) and finish (M_f) temperatures [70].

In addition, plastic deformation of the matrix has an effect on the formation of martensite by primarily increasing the sizes of internal strains and make the nucleation easier. As a result, martensite can form when the metal is plastically deformed at temperatures well above the M_s temperature [70].

In contrast, the martensite formation after grinding can be associated with the heat generation in an extremely small volume of material during grinding, when compared to the large material volume of a workpiece. This implies an extremely high cooling rate (*i.e.* self-quenching), of superior magnitude than the necessary cooling rate for martensite formation [74]. As reported previously, Ueda *et al.* [43] measured cooling rates of a Si₃N₄ grit, after cutting, as high as 10⁶ °C/s. Since the grit heat conduction coefficient is equal or lower to the usually employed steels, it is possible to describe an analogy with the workpiece material martensite formation.

It has also been reported that in typical grinding applications employing high specific material removal rates when grinding steels, the temperature can reach up to 700 – 1000 °C [21, 23, 40, 76-80].

Recently, Fang-yuan *et al.* [78] investigated the formation of white and dark layers after hard turning of AISI 52100 steel. The authors extensively characterized the resulting microstructure, after face turning, using several techniques: scanning electron microscopy (SEM), carbon distribution by electron probe microanalysis (EPMA), diffraction pattern by X-ray diffraction (XRD), hardness by nanoindentation and transmission electron microscopy (TEM). All applied machining conditions generated modifications on the microstructure to the point of white layer formation. The following conclusions were drawn:

- a) The white layer is composed of equiaxed subgrains of martensite and retained austenite. The austenite transformation can occur instantaneously under the action

of a large driving force. The rapid heating rate and the substructures such as dislocations and twins promote the austenite nucleation. Moreover, dislocations, twins, and stacking faults can further refine the grains in the white layer, and thus equiaxed nanocrystals are formed in the white layer.

- b) The dark layer is formed owing to the interaction between the high-temperature tempering process and plastic deformation. Lamellar ferrite and dynamic recrystallization grains are observed in the dark layer, but no austenite is indexed. The heat diffused into the interior of the workpiece results in the high-temperature tempering in the subsurface.

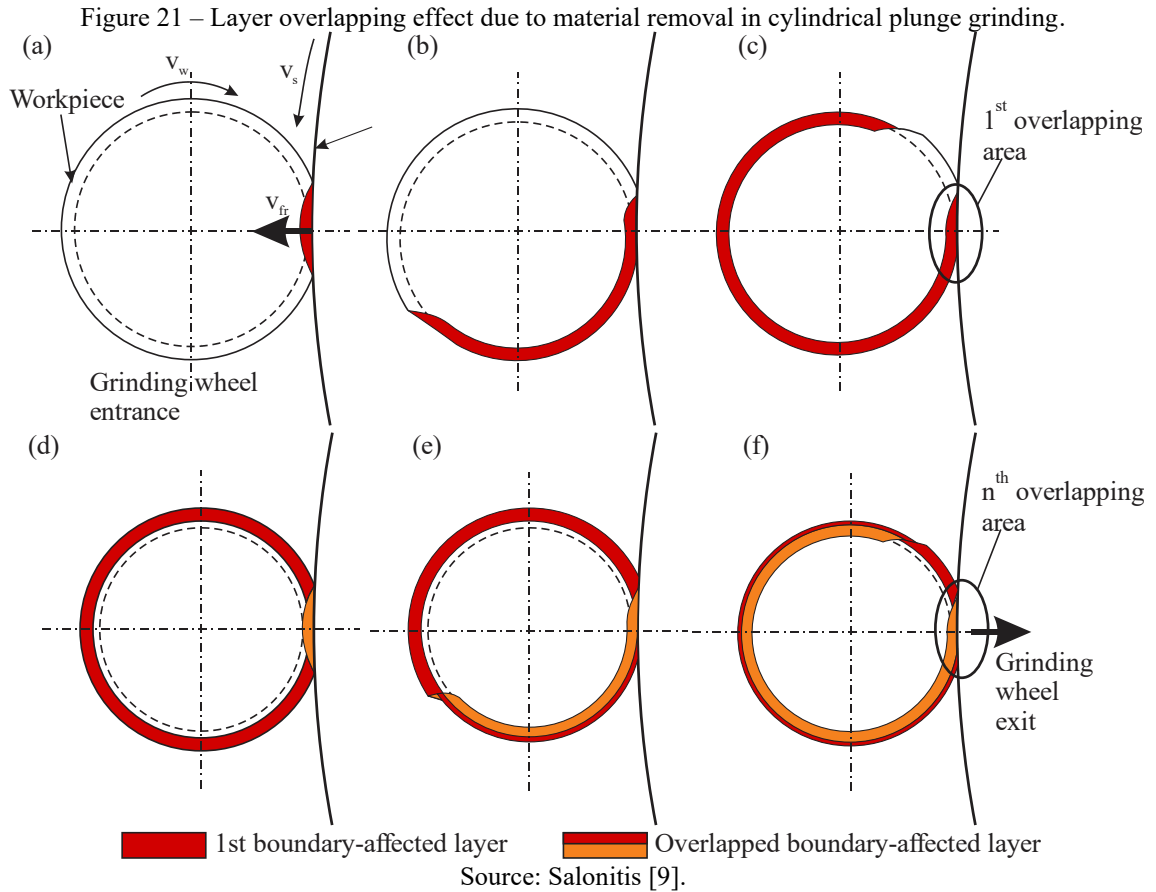
To summarize, the mechanisms that trigger martensite formation during quenching heat treatment are present in the grinding process, considering the input variables.

Therefore, controlling the heat transfer in order to ensure that the workpiece material does not undergo any metallurgical changes is one of the goals of boundary-affected layer investigations. However, this problem can also be considered an opportunity. The mechanism of induction of martensite formation through the grinding process (*i.e.* grind-hardening) has been considered by many authors as a novel and viable process to reduce production times [1, 9, 10, 69, 77-85].

Before considering the influence of the cutting parameters on the boundary layer integrity, it is essential to review the external cylindrical plunge grinding kinematics. One important aspect to be acknowledged is the constant overlapping of the grinding wheel on the already ground surface (Figure 21), posing a challenge to predict the resulting subsurface alterations, as the workpiece may be under constant phase transformation [79].

At the first rotation, one layer of material is removed and the resulting subsurface may undergo microstructural modifications (Figure 21 a, b and c). However, if the modifications are deeper in relation to the depth of cut, in the following rotations the subsurface may undergo further modifications on top of the previous boundary-affected layer (Figure 21 d, e, and f) [9]. This alternating microstructure modification cycle leads to uncertainty on the predictions of the resulting subsurface.

Since the energy input into the workpiece is the main drive for boundary layer alterations, it is expected that any parameter that inflicts change on the thermal and mechanical severity of the grinding process, impacts directly on the subsurface integrity. Considering the specific material removal rate (Q_w') as a process input, the depth of cut (a_e) and workpiece circumferential speed (v_w) parameters have diverging influences on energy distribution.

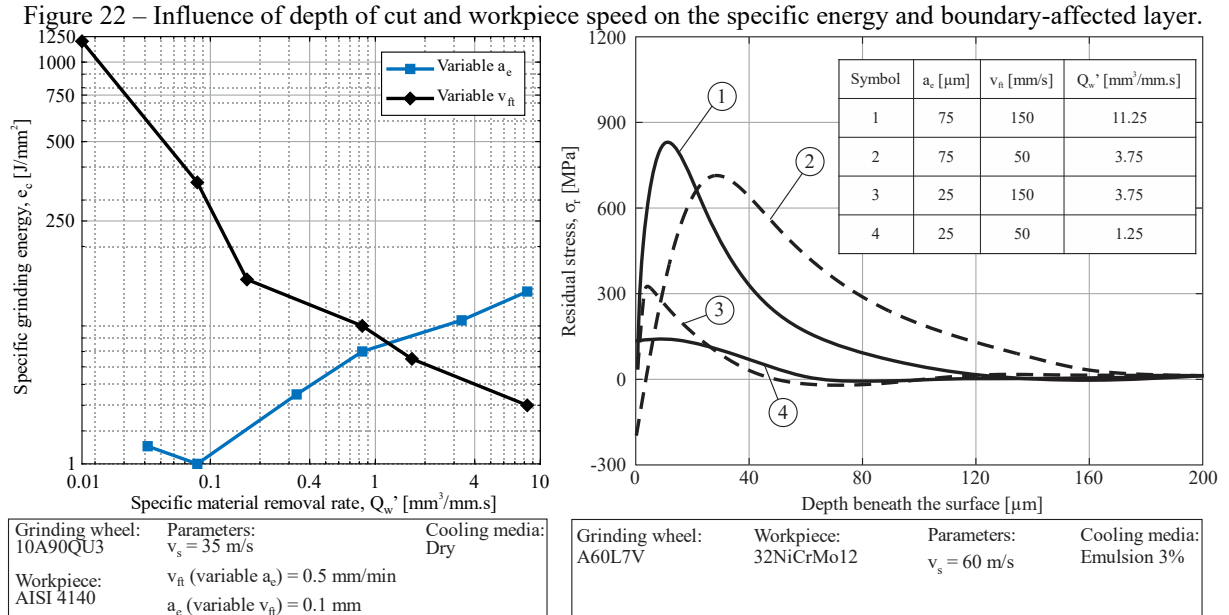


On one hand, increasing the depth of cut leads to an increase in the chip thickness, which translates to a higher portion of deformed material and thus, higher mechanical severity (higher tangential force). Since most of the grinding specific energy is used for material deformation, an increase in heat generation is expected. Also, due to the fact the volume in which this heat is generated rises in a cubic ratio and the surface of this volume rises only with a square ratio, higher temperatures in the deformed volume are bound to appear [69].

On the other hand, in cylindrical plunge up grinding with an increase of the workpiece speed v_w , while the specific grinding rate (volume of removed material in the time unit) is kept constant, the depth of cut a_e is reduced and the chip thickness increases. Additionally, since the moving heat source is faster, less heat is conducted into the workpiece (almost the same amount of heat is generated over a bigger arc on the workpiece surface). Consequently, a lower cutting zone temperature increase is expected [69, 80]. Figure 22 illustrates the measured residual stress and specific energy which states these facts.

Considering the increase in the workpiece speed and a constant depth of cut, the increase of specific material removal rate leads to a reduction of specific grinding energy. This reflects on the residual stress, which shifts slightly closer to the surface and presents a slight increase in magnitude. Oppositely, for a constant workpiece speed and increasing the depth of

cut, specific grinding energy increases, which in turn leads to larger shifts on the residual stress distribution and magnitude.



Source: Adapted from Brockhoff [69], Snoeys *et al.* (1978) *apud* Brinksmeier *et al.* [80].

The influence of these input parameters on the boundary-affected layer was investigated by several authors:

Balart *et al.* [85] evaluated the effect of increasing the input parameters (v_s , a_e , v_w) on surface grinding of AISI 1055 and 52100 steel. The measured temperature and residual stress varied with a combination of the parameters a_e and v_w , showing that the employed parameters contributed to the change in temperature and, therefore, altered the residual stress state of the ground surface.

Kruszynski and Wojcik [86] elaborated a coefficient (B , in $\text{W}\cdot\text{s}/\text{mm}^2$) that considers the grinding total power (P), wheel width (b_s), and workpiece speed (v_w). Experimental results were obtained on surface grinding of different steels, by varying the depth of cut (a_e , 0.005 to 0.06 mm) and workpiece speed (v_w , 0.08 to 0.5 m/s). The resulting coefficient exhibited a linear correlation (model $R^2 \approx 0.86$) with the maximum residual stresses, which changes accordingly with the parameters.

Zarudi and Zhang [87] also reported the influence of the depth of cut and workpiece speed on the boundary layer, on surface grinding of an AISI 4140 tempered steel. The authors employed low specific material removal rates from 0.01 – 0.52 $\text{mm}^3/\text{mm}\cdot\text{s}$ and obtained affected layers up to 1000 μm . Due to the low workpiece speed $v_w = 0.02$ – 0.3 m/min the high

plastic deformation without chip forming and the high time for heat flux to the workpiece is responsible for that.

Alonso *et al.* [88] investigated the effect of the combination of the a_e and v_w parameters on the hardness penetration depth (HPD, a parameter for grind-hardening control). The experiments were carried out in cylindrical AISI 1045 steel workpieces, characterized after external cylindrical tangential grinding. The Q_w' varied (as a function of the v_w , v_{fa} and a_e parameter). As expected, the authors observed that increasing the workpiece speed (0.1 to 0.2 m/s) leads to a decrease in the HPD parameter. The authors also found a satisfactory inverse correlation (regression value $R^2 \approx 0.82$) between the Barkhausen Noise parameter and the HPD.

Jermolajev and Brinksmeier [89] elaborated, on external cylindrical plunge grinding AISI O2 steel (quenched and tempered to 48 HR_c), a diagram that indicates different zones of boundary layer modification (hardness and residual stress). These zones were quantified in terms of the contact time and maximum contact zone temperature (as a function of the a_e , v_w and v_{fr} parameters).

Chang *et al.* [31] evaluated the effect of input parameters (v_s , n_w and a_e) on the boundary layer alterations, on internal cylindrical plunge grinding of an AISI 52100 bearing steel (61 HR_c). Results show a little effect when increasing the workpiece speed and depth of cut, whilst the grinding speed wielded the most significant changes in the boundary layer.

Recently, Sridharan *et al.* [90] developed a model integrating temperature and Barkhausen Noise analysis to predict surface integrity on a bearing AISI 52100 steel after external cylindrical plunge grinding. Increasing the workpiece speed at the same specific material removal rate leads to a reduction of the contact time and, thus, reduces the effect on the boundary-affected layer.

However, most investigations verify the effects of conventional electro-fused aluminum oxide, while very few studies treat the application of microcrystalline aluminum oxide in terms of the boundary-affected layer.

For instance, Kitamura and Gotanda [67] evaluated the residual stress distribution with the increase of the removed material (wheel life), on surface grinding of an AISI 1055 steel. Conventional white fused (WFA) and sol-gel (SG) aluminum oxide grinding wheels were used in the experiments. Results show a continuous increase in the residual stress, shifting from compressive to tensile stress when using the WFA grinding wheel; whereas the SG grinding wheel induced a stable and steady increase in the residual stress (remaining in the compressive region). The grinding wheel structure was only specified by the manufacturer's label.

In a similar approach, Fathallah *et al.* [16] compared conventional grinding wheels with white fused aluminum oxide and grinding wheels with sol-gel aluminum oxide, on surface grinding of AISI D2 steel. The subsurface integrity was evaluated in terms of residual stress, under several specific material removal rates. For an increase in the Q_w , the results show a significant rise in the residual stress (from initial compressive to tensile) for the white fused aluminum oxide, whereas the sol-gel aluminum oxide presented a slower increase on the residual stress. No clear information about the specific characteristics of the grinding wheels was given.

Madopothula *et al.* [17] observed, on surface grinding of AISI 52100 steel, that, when grinding with a sol-gel aluminum oxide grinding wheel, higher grinding force, temperature rise, and boundary-affected layer thickness were achieved, than with white fused aluminum oxide grinding wheel. The specific material removal rate used in the experiments was $1.2 \text{ mm}^3/\text{mm}\cdot\text{s}$ considered a finishing application. According to the authors, the dominant wear in sol-gel grains was flattening, whereas for the white fused grains were the fracture and, therefore, leading to significant changes in the process characteristics and results. In this paper also no detailed information was given for the exact composition of the grinding wheel.

2.4 SUSTAINABILITY AS A KEY PERFORMANCE INDICATOR IN MANUFACTURING

With the increase in environmental awareness, the reduction and control of environmental and social impacts on the manufacturing process become an additional objective on the manufacturing research, previously focused only on improving efficiency, precision, accuracy and cost reduction [91-92].

One approach in development, to evaluate the sustainability of a manufacturing process, is the use of sustainability indicators (SI). This method encompasses three sustainable dimensions (economics, social and environmental), in several levels (companies, processes, and products), especially for users with limited resources [91]. Also recently, in response to the increasing pressures and as a forum for establishing responsible practices, ASTM initiated a subcommittee on sustainable manufacturing and elaborated the normative ASTM E3096-18 [93], which defines the identification, definition, selection, and composition of environmental Key Performance Indicators (KPI) for individual processes [94].

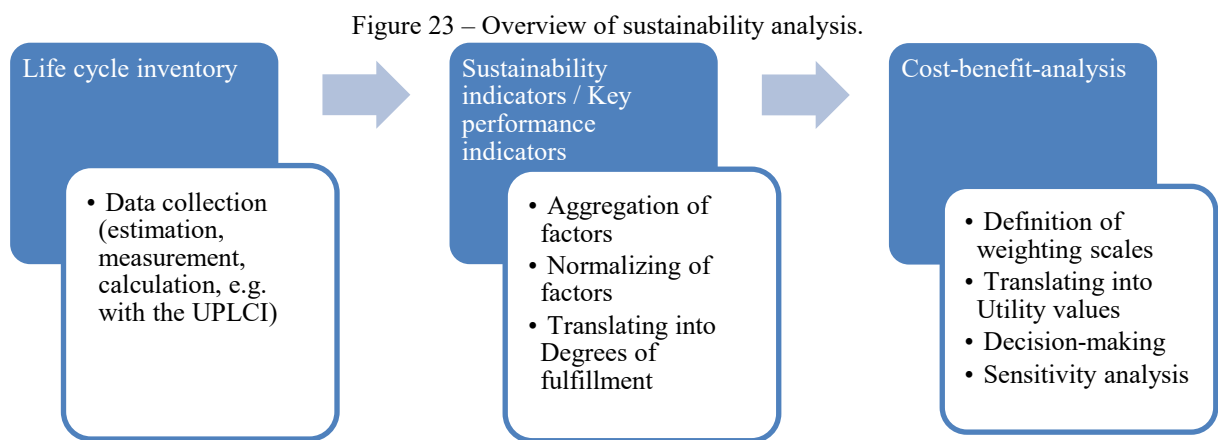
In response to such needs, several authors [91, 95-98] have sought to evaluate the life-cycle inventory of a focused manufacturing step, *e.g.* applied to many grinding operations. As

means to build reliable indicators based on several measurable aspects (energy, tool wear, volume of material removed, surface integrity, etc.), they allied the empirical/experimental results with the qualitative sustainability analysis.

Linke *et al.* [91] elaborated a methodology to evaluate and calculate the grinding process life-cycle inventory using as KPIs only a handful of outputs from the grinding process (energy intensity, non-renewable materials intensity, production rate, labor costs, and investment). These KPIs can be calculated using empirical/experimental data, as well as literature resources [99].

Such indicators are, to a great extent, dependent on the grinding process stability. An application of a specific grinding tool associated with a specific grinding condition can be strictly correlated and predicted. Therefore, if a minimal initial grinding condition is known (*e.g.* grinding wheel specification, cutting parameters, dressing parameters, workpiece properties, etc.) a comparative environmental impact can be estimated and used as a decision-making tool.

A sustainability analysis follows three steps, as proposed in [91] Figure 23.



Source: Linke *et al.* [91].

First, the life cycle inventory (LCI) is generated with data from measurements, estimations, and calculations such as described in the Unit Process Life Cycle Inventory (UPLCI) method [98]. Then selected LCI data can be aggregated and normalized into sustainability indicators (SI) or key performance indicators (KPI). These are translated into degrees of fulfillment (DFs). Finally, the cost-benefit analysis method allows to give different weighting scales to the DFs, translate them into Utility Values (UV), and make a decision based on these. Sensitivity analysis allows for increasing confidence in the results.

The use of such tools aims to evaluate the efficiency of the process at several levels, quickly becoming a reliable tool for decision-making.

2.5 RESEARCH GAP

Based on the presented literature review, it could be seen that many works have performed experimental approaches on grinding of steels with conventional grinding wheels with microcrystalline aluminum oxide abrasive grits, elaboration of multi-step plunge motion and influences of the input parameters on the surface integrity. However, there are still controversies of the influence of the microcrystalline aluminum oxide on the surface integrity of a ground workpiece.

Also, all those publications have a common gap: lack of precise information of the grinding wheel structure and content (abrasives, binder, and pores), since the information from the manufacturer is hardly precise. The characterization of the grinding wheel outside the scope of the usual empirical methods (sandblasting and GrindoSonic acoustic emission tests) is expensive and time-consuming. Technologies and techniques of porosity evaluation in rocks, such as tomography in micro and nano scales, introduces a precise alternative.

The correct information, given by the manufacturer or characterized using the available techniques, is important to understand the wear mechanisms in conventional grinding wheels. Monocrystalline and microcrystalline aluminum oxide abrasive grits have different morphologies, surfaces and breakage mechanisms, which might influence the binding strength of the wheel structure, self-sharpening effect, etc. Because of these uncertainties, the energy generation is greatly affected, which might negatively impact the already environmental unfriendly grinding process.

These aspects highlight the grinding wheel not as another input parameter, but an input variable of the process that must be considered in the elaboration of a multi-step plunge motion during cylindrical grinding, aiming as well for a more sustainable manufacturing process.

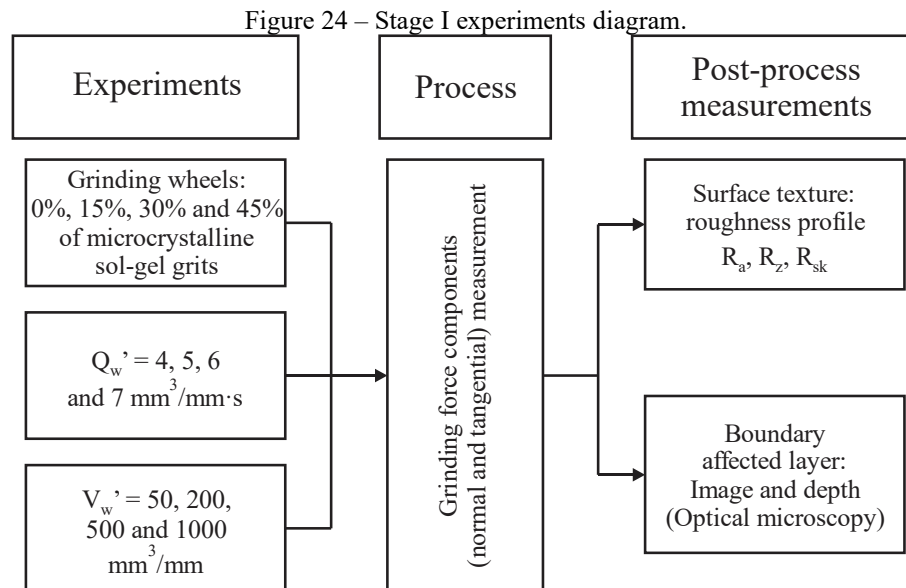
3 MATERIALS AND METHODS

In order to elaborate on a grinding cycle routine that considers the necessary over-measure for finishing operations, this study was separated into two stages. The first stage consists of the evaluation of some input parameters (grinding wheel abrasives, specific material removal rates, the volume of removed material) on the surface integrity based on exploratory experiments. The second stage elaborates a multi-step external cylindrical circumferential plunge grinding cycle algorithm, restricted by the surface integrity.

3.1 PROCESS PLANNING

This study was distributed in two main stages:

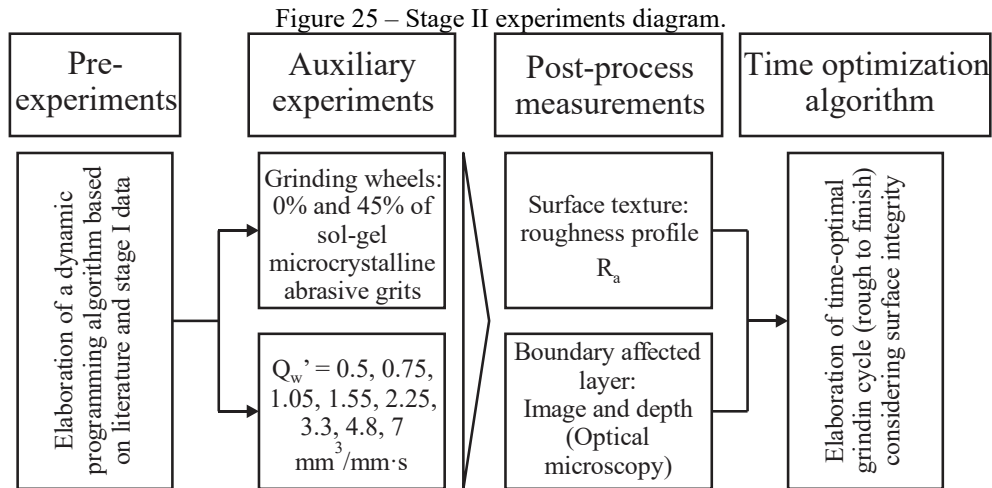
Stage I (Figure 24) consists on exploratory experiments to characterize the surface integrity of external cylindrical plunge ground components, performed with grinding wheels with various microcrystalline Al_2O_3 content (0%, 15%, 30%, and 45%), fixed specific grinding rates Q_w' (4, 5, 6, and 7 $\text{mm}^3/\text{mm}\cdot\text{s}$) and specific material removal V_w' intervals (50, 200, 500, and 1000 mm^3/mm).



Source: Author.

Stage II (Figure 25) consists of an experimental procedure to elaborate an external cylindrical circumferential plunge grinding cycle, with decreasing and discretized specific grinding rates (Q_w'), from roughing to finishing, that minimizes grinding cycle time and also

meets the surface integrity standards (minimized boundary-affected layer, minimum surface roughness). The discretized Q_w' values were selected as a geometric progression series, with a multiplying factor of 1.45, totalizing eight values, from 0.5 to 7 mm³/mm·s.



Source: Author.

3.2 INPUT SYSTEM PARAMETERS

3.2.1 Machine-tool

The experiments were performed at the *Laboratório de Mecânica de Precisão* (LMP), of the *Universidade Federal* of Santa Catarina (UFSC) – Brazil, on Zema Zselics Pratika Flexa-600-L universal cylindrical grinding machine, controlled by a Siemens Sinumeric 840D CNC command. Table 2 specifies the machine-tool characteristics.

Table 2 – Machine-tool specifications.

Item	Description	Unit
Machine-tool type	Cylindrical grinding	
Tool peripheral speed	100	m/s (max.)
Tool spindle power	5.6	kW
Tool dimensions (D x T x H)	400 x 30 x 203	mm x mm x mm
Tool minimal dimensions	305 x 30 x 203	mm x mm x mm
Workpiece spindle power	1.5	kW
Workpiece spindle rotational speed	600	1/m (max.)
Feed motor power (Z)	1.5	kW
Feed motor power (X)	1.5	kW
Feed speed (Z)	0.0005 - 6,000	mm/min
Feed speed (X)	0.001 - 12,000	mm/min
Required air pressure	6	bar
Coolant pump power	3	kW

Item	Description	Unit
Additional power needs (including controls, drives, etc)	5.5	kW
Dresser power	0.5	kW
Total max. Power	23.5	kW

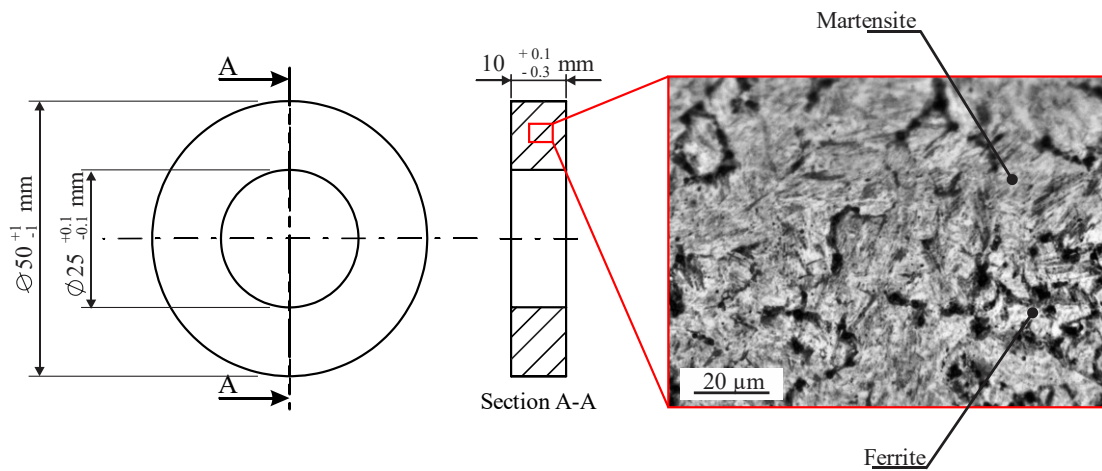
Source: Zema [100].

The workpiece was mounted on a custom-made cylindrical holder, integrated with a piezoelectric grinding force measuring system, fixed on the workpiece spindle (headstock).

3.2.2 Workpiece material

Ring-shaped workpieces quenched and tempered to a hardness of 400 ± 30 HV were manufactured in AISI 1040 steel. The ring-shaped geometry was conceived similarly to bearing components in order to allow the workpiece to clamp on the piezoelectric tool holder. Figure 26 illustrates the overall workpiece geometry and microstructure obtained after heat treatment.

Figure 26 – Ring-shaped workpiece.



Source: Author.

The workpiece material matrix is composed of quenched and tempered martensite, with little indication of free ferrite (white regions).

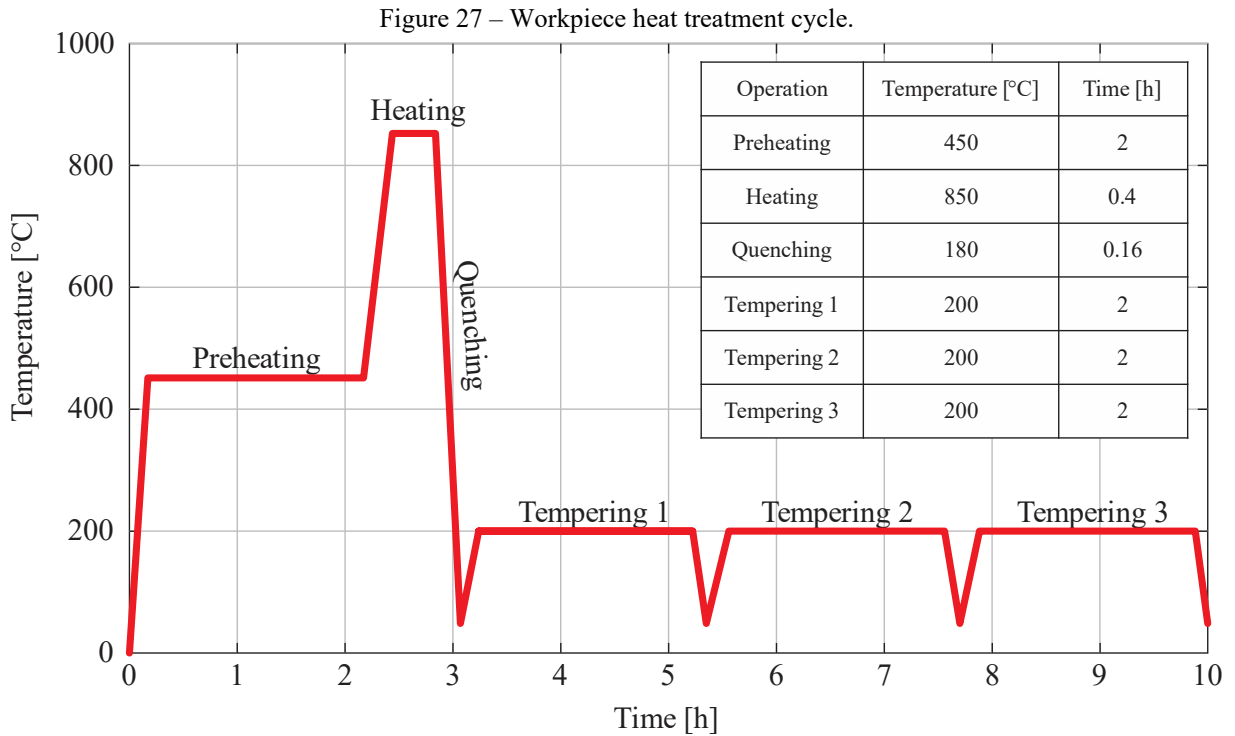
The chemical composition of the steel, obtained through spectroscopy, is depicted in Table 3.

Table 3 – Chemical composition of the AISI 1040 steel, mass %.

C	Si	Mn	P	S	Cr	Ni	Cu	Fe
0.399	0.207	0.756	0.014	0.021	0.148	0.082	0.126	Balance

Source: Author.

The workpiece manufacturing chain followed a specific route: external turning, drilling, heat treatment, and internal turning. The heat treatment was performed by Tecnotempera [101], an external company, with a heat treatment cycle shown in Figure 27.



Source: Adapted from Tecnotempera [101].

3.2.3 Grinding wheel

The grinding wheels used in the experiments were manufactured by *Krebs & Riedel Schleifscheibenfabrik GmbH & Co. KG* and delivered to the LMP in the scope of the partnership established with the Brazilian-German Collaborative Research in Innovative Manufacturing project, BRAGECRIM with the *Technische Universität Berlin (TU Berlin)*.

According to the manufacturer, the grinding wheels are composed of a mixture of two abrasives grits: monocrystalline Al_2O_3 (obtained through the electro-fusing process) and microcrystalline Al_2O_3 (obtained through the sol-gel process). Table 4 references the combination of the abrasive grits.

According to the grinding wheel specification (1A1 400 x 30 x 203.2 A80J6V), the wheels are conventional grinding wheels, with vitreous bonding, average grit size of 80 Mesh (185 μm), hardness J and porosity 6. The tools were delivered for the initial grinding experiments at the IWF – TU Berlin with 30 mm width, an inner diameter ID of 203.2 mm and an outer initial diameter OD of 500 mm. Since the Zema machine-tool only supports OD 400

mm grinding wheels, a 50 mm outer ring section of the grinding wheel was cut-off. This ring section was used to characterize the grinding wheel material.

Table 4 – Grinding wheel abrasive grit content and description.

Abbreviation	Volumetric concentration [%]		Color
	Monocrystalline Al ₂ O ₃	Microcrystalline Al ₂ O ₃	
MC00	100	0	white
MC15	85	15	lighter blue
MC30	70	30	light blue
MC45	55	45	blue

Source: Author.

Small cylindrical probes were trepanned, with aid of a diamond cup saw, from the cut-off ring sectors of the grinding wheel. The removed cylinders (OD 10 mm x 30 mm length; and OD 4 mm x 10 mm length) were characterized through X-ray microtomography on a Versa XRM-500 tomographer. The image acquisition parameters for the computer tomography are listed in Table 5.

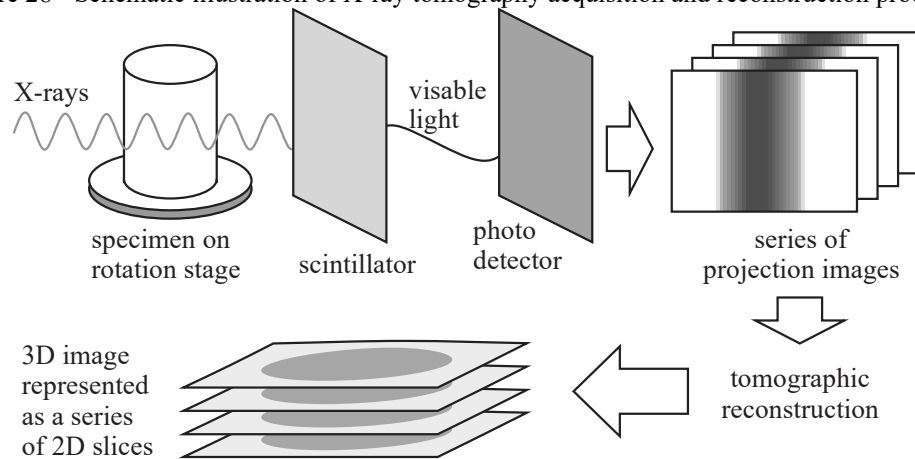
Table 5 – X-ray tomography acquisition parameters.

Technique (scale)	Micro
Resolution (image pixel size)	10.5 μm (first acquisition), 3.83 μm (second acquisition)
Image size	988 px x 1011 px
Number of images (slices)	800 images/sample
Camera binning	2
Font	60 kV / 5 W
Exposition time	5 s
Angular step	0.225°

Source: LMPT [102].

Sections of the samples were acquired (Figure 28) and characterized in terms of phase distribution using the software Avizo and Imago 3D. Imago3D is a non-commercial platform, developed at *Laboratório de Meios Porosos e Propriedades Termofísicas (Universidade Federal de Santa Catarina)* in partnership with Petrobras (Brazilian oil company), designed to analyze 3D images with available tools for image processing and characterizations. The acquisition, segmentation, and analysis were supported by the *Laboratório de Meios Porosos e Propriedades Termofísicas (LMPT)*, at the UFSC.

Figure 28 - Schematic illustration of X-ray tomography acquisition and reconstruction processes.



Source: Adapted from Landis and Keane [103].

3.2.4 Dressing system and conditions

Two different dressing systems were applied, corresponding each to a different stage.

For stage I, a diamond dressing disc, *Diamantwerkzeuge Hameln*, with an external diameter of 110 mm, nomenclature R140 IN2515, average grit size of 250 μm , plane profile, vitrified bonding with a steel structure was employed for the grinding wheels MC15, MC30, and MC45. For the MC00 it was employed a dressing plate, described in the stage II experiments.

For stage II, it was utilized only the dressing plate, provided by the company *Cantena*, containing three square diamond grits embedded on a metallic structure, dimensions of 0.8 mm x 0.8 mm x 5 mm. The dressing conditions are depicted in Table 6.

Table 6 – Dressing conditions for both stages.

	Stage I (dressing disc, dressing plate)	Stage II (dressing plate)
Grinding wheel circumferential speed v_s	30 m/s	
Dressing speed ratio q_d	0.6	-
Dressing tool circumferential speed v_d	18 m/s	-
Active dressing width b_d	0.8 mm	0.8 mm
Axial dressing feed rate v_{fad}	1172 mm/min	576 mm/min
Dressing overlap ratio U_d	1	2
Depth of cut in dressing a_{ed}	10 μm	
Total dressing depth	200 μm	

Source: Author.

The differences in dressing overlap ratios are associated with grinding conditions. Since stage I prioritized roughing conditions, the overlap ratio was lower. In stage II, a less

aggressive dressing condition was selected in order to be applicable to roughing and finishing grinding cycles.

3.2.5 Cooling media and conditions

A 3% emulsion ECOCOOL semi-synthetic oil AP71, Fuchs Co, was utilized as cooling media. The fluid was delivered tangentially to the grinding region through a free jet nozzle. The fluid flow was approximately 20 l/min. The cutting fluid is continuously filtered through external equipment, composed of magnetic and mechanical paper filters. The filters were provided by the company Freudenberg Filtration Technologies.

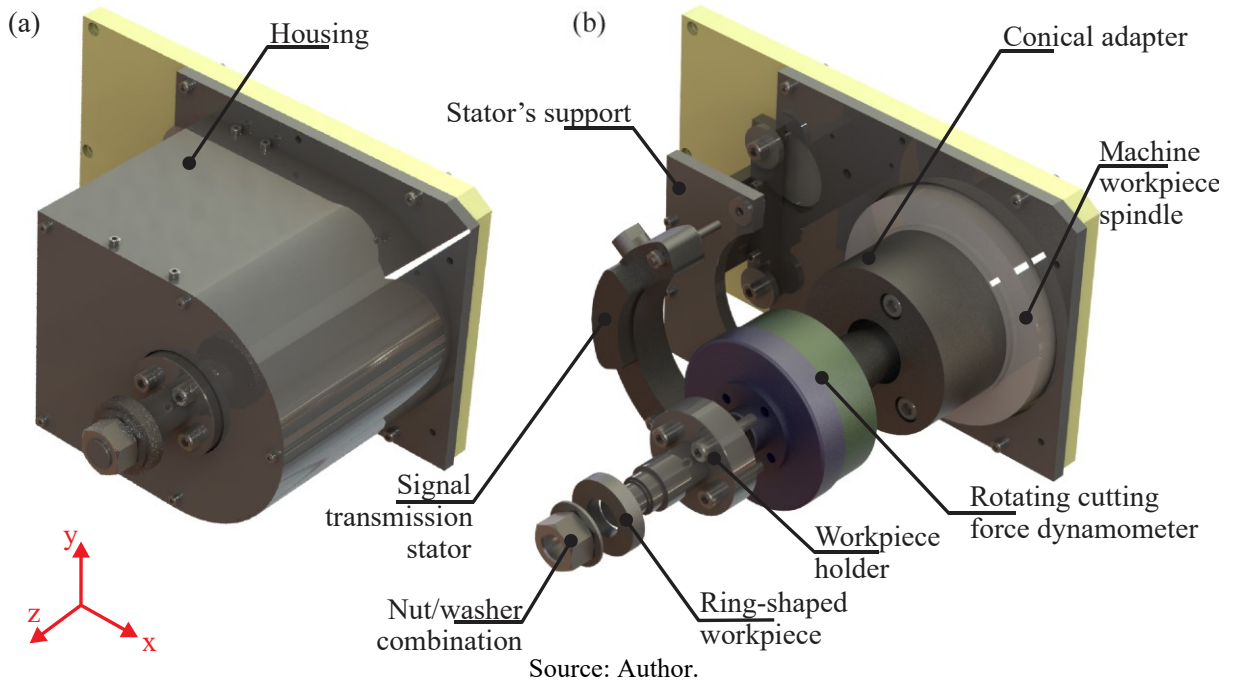
3.2.6 Grinding force measurement system

To monitor the grinding forces a piezoelectric Kistler Instrumente AG rotating cutting dynamometer RCD (model 9124B1111) with a signal transmission stator (model 5221B) and multichannel signal conditioner (model 5223B2) were used. The rotating dynamometer measures three orthogonal force components (F_x , F_y , F_z) along with the axial and radial directions, as well as the torque M_z along the axial direction of the dynamometer. The equipment was originally designed for drilling/milling applications; therefore, the probe had to be ground in balance when engaged to the dynamometer. Figure 29 illustrates the details of the force measuring assembly.

The dynamometer was mounted to the workpiece spindle, using a specially designed conical interface (ISO 40). The workpiece itself was fixed to the dynamometer through a holder and clamped with the help of a nut and washer combination. The signal transmission stator was mounted on a support, with a 2 mm gap to the rotor, allowing quick assembly and security for the stator's and dynamometer's body.

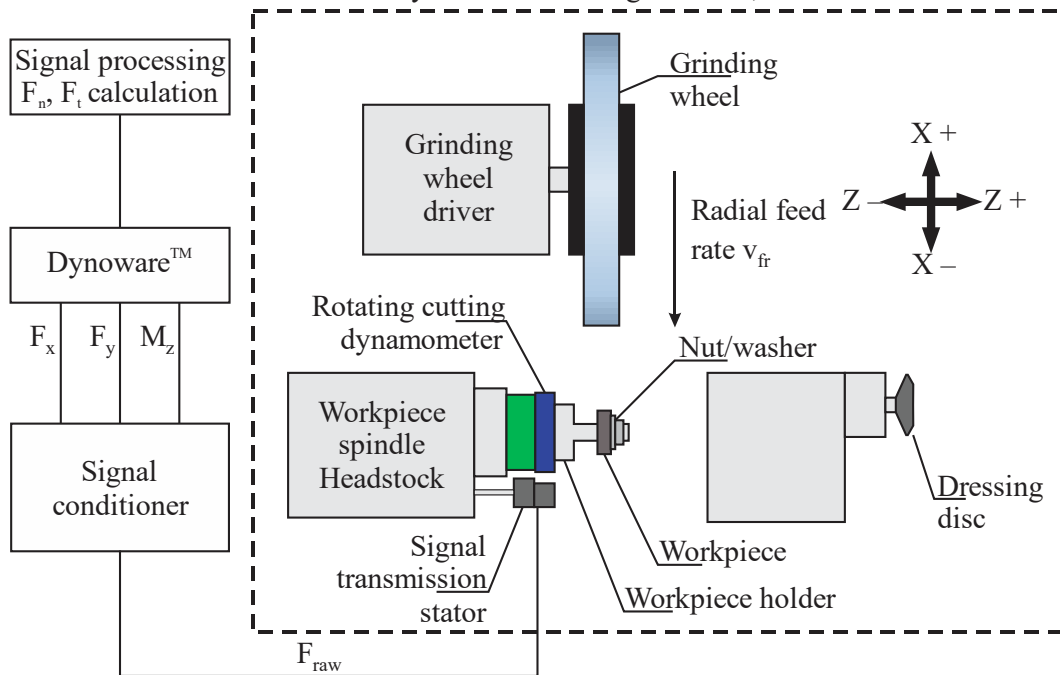
The signals generated by loading the piezoelectric crystals of the dynamometer is sent, via telemetry, to the data transmission stator and the data is sent via cables, from the stator to the signal conditioner Type 5223B. The signal is amplified, digitalized with 12-bit resolution and transmitted as a PCM signal. The data stream is de-multiplexed on the stationary side and converted back into as a $\pm 10V$ analog signal, filtered with a low-pass 1 kHz filter [104].

Figure 29 - Force measuring system: assembled view (a); detailed exploded view (b).



The output signal from the conditioner is sent to PC with PCIMDAS 1602-16 card and plotted on the display through the software Dynoware™, from Kistler Instrumente. Figure 30 illustrates the experimental setup installed on the machine-tool.

Figure 30 – Experimental setup for grinding force measurement/processing. Cylindrical Grinding Machine, Zema Zselics



Source: Adapted from Boaron [105] and Marra [66].

The force signals F_x , F_y and M_z obtained from the rotting dynamometer were processed to obtain grinding force components: normal force F_n and tangential force F_t . The gravitational interferences due to the mass of the measuring system were considered in the calculations. The methodology and signal processing sequence are presented in APPENDIX A and APPENDIX B, respectively. The signal sampling rate f_s was 2 kHz.

3.2.7 Optimization methodology of the grinding cycle

Stage II experiments were conducted as a means to elaborate a database with information on the grinding force components, surface roughness, and boundary-affected layer thickness for a given specific grinding rate. The database generated a text file (.txt) as an output, containing quantitative information of the experiments' results. With this file, an external cylindrical circumferential plunge grinding cycle, from roughing to finishing condition was developed. This cycle considers the maximum specific material removal rate Q_w ' (*i.e.* radial feed rate v_{fr}) to minimize grinding time. Therefore, an operations research methodology, using dynamic programming (DP) algorithms, was applied. The optimization problem was formulated to minimize cycle time (t_c), according to Dong's [24] methodology presented in section 2.1.1. The problem was subject to the restrictions:

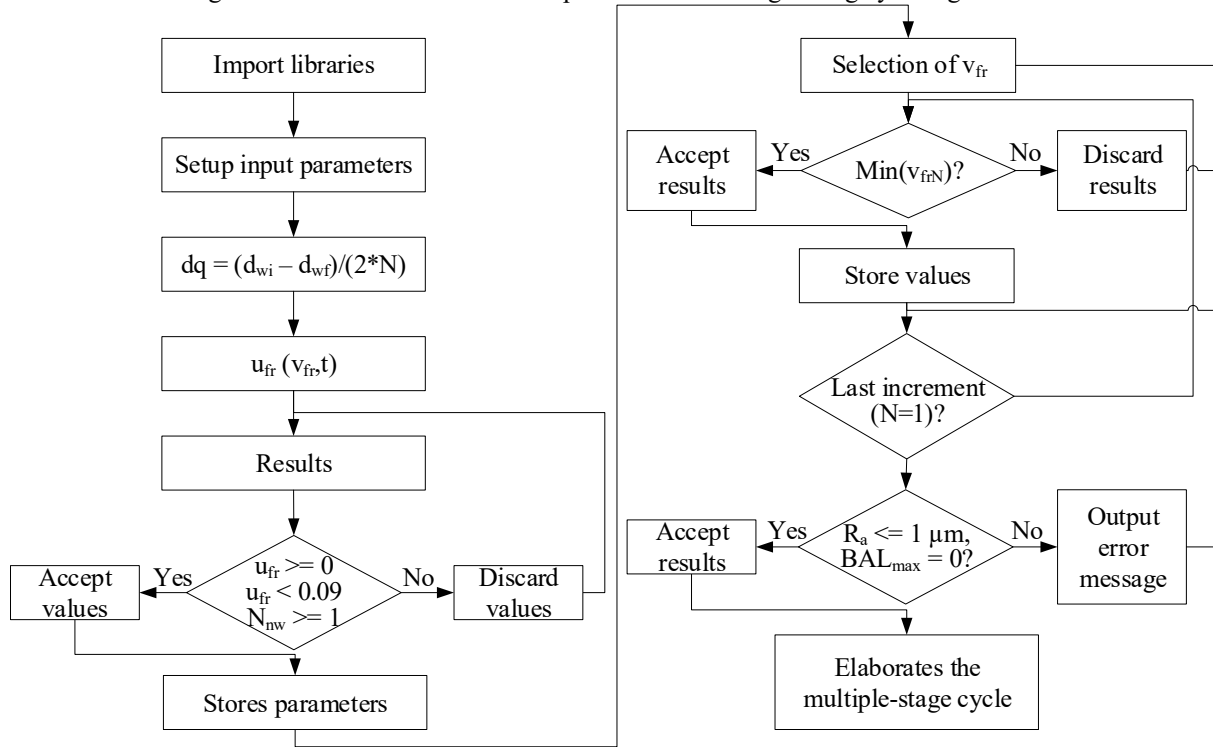
- a) The maximum final surface roughness R_a (user's input);
- b) The maximum final depth of boundary-affected layer (BAL) (user's input);
- c) The upper limit of the machine feed rate (depending on the machine-tool's available power);
- d) Non-negative feed rates; and
- e) The number of workpiece rotations ≥ 1 .

The roundness restriction was not considered in this study, since it was selected a no spark-out condition, due to the interest in evaluating the surface roughness and boundary-affected layer thickness generated by the selected grinding parameters.

The flowchart diagram in Figure 31 illustrates a schematic representation of the algorithm.

The algorithm sequence was based on the step-by-step methodology elaborated by Dong [24]. The code structure was developed by Pereira [106] in python language and is focused on applying experimental data to discretize the commanded radial feed rate and reach an optimal cycle time value.

Figure 31 – Schematic flowchart representation of the grinding cycle algorithm.



Source: Author.

The value for the time constant τ_F was calculated for the force measuring system/workpiece clamping due to the loss in stiffness, using the considerations proposed by Saljé *et al.* [25]. Details for the τ_F attainment can be observed in APPENDIX B. Usual values for this constant, considering external cylindrical circumferential plunge grinding machines, range between 0.5 and 1 s [24, 25].

The following scenarios (Table 7) were used to compare the effectiveness of the elaborate algorithm via a computational simulation of a bearing component grinding, using the experimentally obtained data from stage II experiments.

Table 7 – Simulated grinding cycle scenarios.

Grinding wheel	Grinding cycle	
MC00	Three-step (industry/reference);	Multi-step (optimized);
MC45		

Source: Author.

Considerations for the grinding cycle simulation were lowest R_a ; maximum BAL equal to 0, using a safety margin of 50% (experimental measured BAL thickness was considered 50% higher); time constant τ_F was considered as the value obtained on the force measurement experiments. The maximum specific material removal rate was selected as 7, as observed in the

stage I experiments. The initial (d_{wi}) and final diameter (d_{wf}) of the workpiece were 51 and 50 mm, respectively. The goal of the cycle was to obtain the lowest grinding cycle time.

The output of the results is a text file (.txt), containing N discrete steps as rows, with values of the: commanded radial feed rate, the time constant τ_F , actual feed rate, individual grinding time, boundary-affected layer thickness and, for the final step, surface roughness R_a . The results will be presented in form of charts, obtained by the sum of the individual discrete radial feed rates. The chart illustrates the radial feed rate versus the grinding time.

3.3 INPUT VARIABLE PARAMETERS

3.3.1 Cutting conditions

The cutting parameters employed in the experiments were selected according to preliminary experiments, considering the machine-tool grinding wheel driver power (5.6 kW). In the preliminary experiments, a specific grinding rate Q_w' of $10 \text{ mm}^3/\text{mm}\cdot\text{s}$ was used. The workpiece was a cylinder manufactured in an AISI 1040 steel, mounted and fixed between centers. Due to the intense chatter observed during the experiments, this specific grinding rate was considered unfeasible and discarded from the experiments. Therefore, stage I experiments considered a specific grinding rate up to $7 \text{ mm}^3/\text{mm}\cdot\text{s}$. Stage II parameters were selected based on stage I results, as shown in Table 8.

Table 8 – Input variables and conditions.

Description	Stage I	Stage II
Grinding wheel content	MC00, MC15, MC30, MC45	MC00, MC45
Workpiece material		1040
Grinding wheel circumferential speed v_s		30 m/s
Speed ratio q		60
Workpiece circumferential speed v_w		30 m/min
Specific material removal rate Q_w'	4, 5, 6, 7 $\text{mm}^3/\text{mm}\cdot\text{s}$	0.5, 0.75, 1.05, 1.55, 2.25, 3.3, 4.8, 7 $\text{mm}^3/\text{mm}\cdot\text{s}$
Cutting width a_p		10 mm
Active grinding wheel width $b_{s,\text{eff}}$		10 mm
Specific material removal V_w'	50, 200, 350*, 500, 1000 mm^3/mm	200 mm^3/mm
Spark-out time	None	None

*This condition was only employed for $Q_w' = 7 \text{ mm}^3/\text{mm}\cdot\text{s}$, due to the severe chatter and excessive force observed for $V_w' = 500$ and $1000 \text{ mm}^3/\text{mm}$.

Source: Author.

For stage I, it was considered that the end of the cycle was reached when excessive loads/chatter appeared during the process and limited to a specific material removal of 1000 mm³/mm. To guarantee equal initial grinding conditions, the grinding wheel was dressed with the same dressing parameters before each new experiment. The radial run-out of each new workpiece was carefully removed before each workpiece experiment (v_s of 30 m/s, v_w of 30 m/min, Q_w' of 0.5 mm³/mm·s, V_w' of 50 mm³/mm, $t_{\text{spark-out}}$ of 5 s).

To guarantee that the remaining affected surface layer of the probe corresponds to the chosen grinding conditions, no spark-out was used. Immediately after reaching the final position, the grinding wheel plunge motion was reversed with a radial feed rate v_{fr} of 500 mm/min, mitigating the effect of the spark-out time on the workpiece.

3.4 SURFACE INTEGRITY ANALYSIS

Surface integrity analysis of the workpiece was carried out in terms of surface roughness measurement and boundary-affected layer characterization.

3.4.1 Workpiece surface texture

For surface texture characterization, a profile of the surface was sampled in three positions on the workpiece, separated by an arc of 120° along the perimeter, parallel to the probe rotational axis. In association with the usual vertical roughness parameters (R_a , R_z), amplitude and shape (R_{sk}) parameters were evaluated, in order to observe changes due to the grinding wheel wear. This number of measurement positions was selected due to the rotation ratio $q = 7$, between the grinding wheel rotation (n_s) the workpiece rotation (n_w). At this ratio, the grinding wheel circumferential surface is imprinted 7 times around the probe. Taking three measurements around the probe corresponds to the imprinted position of three equally distributed positions of the grinding wheel perimeter, as Table 9 illustrates.

The roughness profile was obtained using a mechanical stylus roughness meter, Surtronic S-116 type 25, from Taylor-Hobson. The cut-off (λ_c) filter parameter of 0.8 mm was selected after the initial analysis, considering the peak distance R_{Sm} of 0.160 mm (Stage I) and R_{Sm} of 0.320 mm (Stage II).

Table 9 – Angular position of the grinding wheel on the corresponding position of the probe for surface roughness measurements.

Angular displacement of the probe in steps of 51 degrees	Rotational position of the probe for roughness measurements	Total angular displacement of the grinding wheel (degrees)
0	0	0
51		360
103	120	720 + 120
154		1080
206	240	1440 + 240
257		1800
308		2160

Source: Author.

The complete parameter selection for the surface roughness analysis can be observed in Table 10.

Table 10 – Selected parameters for surface roughness evaluation.

Profile	N	λ_c	l_n	Filter	λ_s
R	5	0.8 mm	4 mm	Gaussian	2.5 μm

Source: Author.

An in-depth analysis of the surface roughness (profile and areal evaluations) of the same experiment was performed by Marra [66] in his study.

3.4.2 Workpiece boundary-affected layer analysis

Boundary-affected layer analysis was performed in terms of optical microscopy of the ground probes obtained in stage I and II. A second evaluation by Barkhausen Noise analysis was carried out. However, due to differences in the workpiece final outer diameter, the Barkhausen Noise signal was influenced by the probe's diameter, rendering the results unreliable.

The optical microscopy images were obtained on an Olympus optical microscope BX60M, in conjunction with Leica application Suite LAS EZ. Samples were sectioned in four sections (90° apart, distributed along the workpiece perimeter) and embedded in a thermosetting phenol formaldehyde resin (bakelite - $(\text{C}_6\text{H}_6\text{O} \cdot \text{CH}_2\text{O})_n$). Samples were sanded with SiC sandpapers with decreasing grit size (mesh # 80, 150, 200, 320, 400, 600, and 1200) and polished with Al_2O_3 aqueous suspension of 0.3 μm grit size.

Each region was observed through optical microscopy and a micrographic photo of the most representative section was selected and processed with an open-source image processing

software (FIJI). A Trainable Weka Segmentation plugin, developed by Arganda-Carreras *et al.* [107] which combines a collection of machine learning algorithms with a set of selected image features to produce pixel-based segmentation, was used to segment different regions of the obtained metallographic photography. For each section analyzed, a color segmented image was obtained and then processed, totalizing four measures for each condition.

Image processing followed as such:

The selected images were cropped to a default size (1500 px x 1000 px) and underwent local contrast enhancement using the CLAHE (Contrast Limited Adaptive Histogram Equalization) FIJI plugin. The image was transformed to grayscale and segmented using the Trainable Weka Segmentation plugin [107].

Using the Weka plugin, the following features were used as classifiers for the segmentation phase:

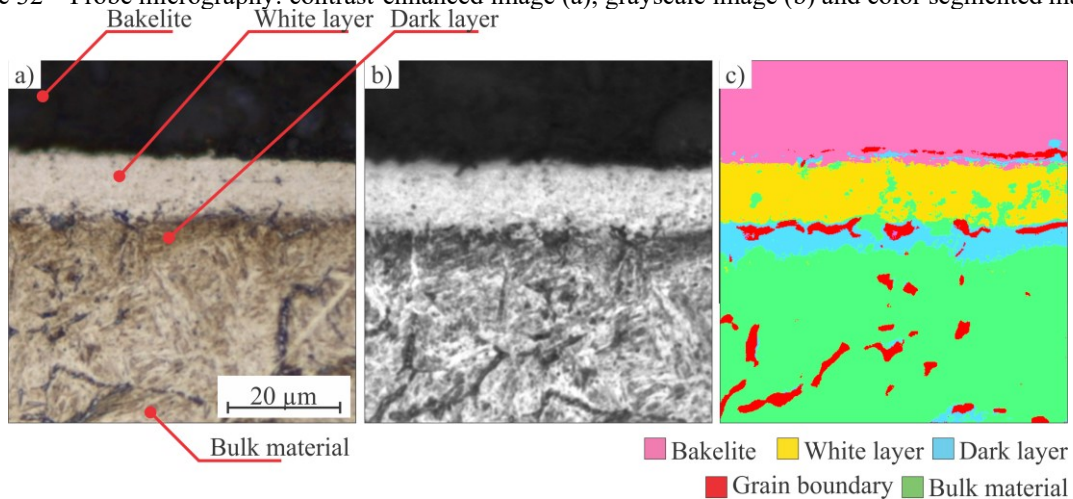
- a) Bulk material (green): The overall matrix phase of the workpiece, usually a mixture of pearlite and tempered martensite;
- b) Grain boundary (red): Presence of grain boundaries;
- c) Excessive etching (purple): due to difficult of control during the etching process, a few isolated regions showed the presence of excessive etching;
- d) Dark layer/overtempered martensite (blue): regions where a complementary tempering occurred, usually visible as a darker layer;
- e) White layer/untempered martensite plus retained austenite (yellow): regions where either a grinding induced quenching occurred or intense plastic deformation occurred, leading to the formation of martensite, visible as a white/blank layer, with the absence of discernable microstructure; and
- f) Bakelite (pink): the embedding resin was also segmented, in order to avoid confusion with other features.

Figure 32 illustrates a representation of the contrast-enhanced image, grayscale image and feature segmentation by color mapping.

Thereafter, the color-mapped image (Figure 32c) is segmented to a binary image (black and white) by applying the histogram tool, individually selecting the dark layer (blue colored area) and white layer (yellow colored area). An algorithm calculates the area of each new binary image and outputs the value to a text file.

The area of each segmented feature was divided by the image width, calculating the thickness of the boundary-affected layer (BAL).

Figure 32 – Probe micrography: contrast-enhanced image (a), grayscale image (b) and color segmented map (c).



Source: Author.

Along with the quantitative evaluation of the alterations, a qualitative evaluation, based purely on observation, was conducted. The following features were observed and considered: presence white layer (untempered martensite plus retained austenite) and presence of dark layer (overtempered martensite). These features were considered as binary values (0 for no presence and 1 for presence) and evaluated in the four sections of the workpiece periphery.

3.5 STATISTICAL ANALYSIS

The grinding wheel is considered a tool with countless cutting edges, normally distributed along the tool's periphery and width, therefore errors and disturbances influencing the grinding process are either recognized as strong disturbances or can be neglected. Average values and their standard deviation and maximum values were calculated considering the entire periphery of the workpiece as repetitions.

A variance analysis (ANOVA), using a significance level of 95%, was used. Since, in the experiments in stage I, not all conditions achieved the predicted specific material removal (V_w'), a full factorial analysis was not conceivable. Instead, only a first-level analysis was conducted, with no interaction between the independent variables.

For the grinding experiments at the second stage, first and second level analyses were conducted.

3.6 RESULT COMPARISON USING A DECISION-MAKING METHOD

In order to ascertain the flexibility of the grinding wheels, a decision-making method based on life cycle inventory was applied to evaluate a fictional condition of a product manufacturing, focused specifically on the grinding process. This allows for a focused evaluation of a manufacturing operation (*i.e.* external cylindrical plunge grinding) and a specific scenario (*i.e.* grinding wheel content, with and without finishing cycle). This investigation was performed in cooperation with the Manufacturing and Sustainable Technologies Research Laboratory (MASTeR lab), at the University of California Davis (UC Davis).

Since the grinding wheels with microcrystalline Al_2O_3 content are indicated for applications with high rates of material removal, two distinct scenarios were selected: one applying only high specific material removal rates, usual application of MC- Al_2O_3 grinding wheels; and the other one, using the grinding wheel for a full grinding cycle, from rough-to-finish feed motion. The conditions are enlisted in Table 11.

Table 11 – Scenarios applied to a life cycle inventory decision-making method.

Scenario	Stage II
A	Grinding without finishing step
B	Grinding with finishing step

Source: Author.

For scenario A, no restrictions to the boundary-affected layer and to the surface roughness were selected; whereas in scenario B, the algorithm was applied to achieve no BAL and the lowest surface roughness possible.

The grinding cycles were selected from the optimal cycles generated by the optimization algorithm developed on this thesis.

Six indicators were selected and calculated, representing the economic, environmental and social aspects of a sustainability analysis: electrical energy intensity (in kW), non-renewable materials intensity (in kg), production rate (in $\text{mm}^3/\text{mm}\cdot\text{s}$), labor costs (R\$), investment (normalized by the grinding wheel cost), and product life N_f (10^6 cycles to fatigue). The calculated indicators were normalized considering a fictional production of 1000 components.

Each indicator was calculated using either input parameters from the experimental procedures or existing literature. The following list illustrates the considerations used for each indicator calculation:

- a) Electrical energy intensity depends on the manufacturing process of electrical power input (machine-tool and adjacent systems, grinding power). Not only the necessary energy for the grinding operation, but also the idle energy, dressing energy, and dislocation energy were calculated. A step-by-step procedure was elaborated by Linke *et al.* [99], calculated by Eq. (16) through (19)

$$E_{\text{grinding}} = \left(V_w \cdot \frac{F_t \cdot v_s}{Q_w} \right) \cdot t_{\text{grinding}} \quad (16)$$

$$E_{\text{idle}} = ((P_{\text{spindle}} + P_{\text{cooling,pump}}) \cdot \eta) \cdot (t_{\text{grinding}} + t_{\text{dressing}} + t_{\text{air}}) \quad (17)$$

$$E_{\text{basic}} = P_{\text{controls, drives,etc}} \cdot (t_{\text{idle}} + t_{\text{load/unload}}) \quad (18)$$

$$E_{\text{total}} = E_{\text{basic}} + E_{\text{idle}} + E_{\text{grinding}} \quad (19)$$

where:

E_{grinding} is the energy dispended during the grinding process to remove material [W]

E_{idle} is the energy used for tasks that do not involve tool-workpiece engagement [W]

E_{basic} is the power necessary for the machine-tool to function [W]

E_{total} is the total energy spent during the grinding process [W]

t_{grinding} is the grinding time [s]

P_{spindle} is the grinding wheel spindle power [kW]

$P_{\text{cooling, pump}}$ is the cooling pump power [kW]

η is the efficiency for the machine-tool subsystems [-]

t_{dressing} is the necessary time for dressing divided by the number of parts manufactured before dressing is required (based on grinding wheel wear) [s]

t_{air} is time spent for grinding wheel movement to the grinding position [s]

$P_{\text{controls, drives}}$ is the necessary power for the machine to function without any motion [W]

t_{idle} is the time spent on idle motion and in grinding process ($t_{\text{grinding}} + t_{\text{dressing}} + t_{\text{air}}$) [s]

$t_{\text{load/unload}}$ is the necessary time for loading and unloading the component on the machine-tool

- b) Non-renewable materials intensity: considers particles due to the grinding wheel wear and workpiece material removed as waste and disposable. This waste volume can be calculated by Eq. (20) through (24)

$$V_s = \frac{V_w}{G} \quad (20)$$

$$D_{\text{waste}} = \frac{1}{f_{\text{dressing}}} \cdot \left(\frac{\Delta_{rs}}{a_{ed}} + 1 \right) \quad (21)$$

$$V_d = \left[d_s^2 - \left(d_s - \frac{D_{\text{waste}}}{1000} \right)^2 \right] \cdot \frac{\pi}{4} \quad (22)$$

$$m = V \cdot \frac{\rho}{1000} \quad (23)$$

$$m_{\text{total}} = m_d + m_w + m_s \quad (24)$$

where:

D_{waste} is the waste caused by the dressing operation [μm]

f_{dressing} is the dressing frequency [1/part]

d_s is the grinding wheel diameter [mm]

ρ is the material-specific mass [g/cm^3]

- c) Production rate considers the average specific material removal rate Q_w' , calculated using the commanded radial feed rate v_{fr} obtained for each step of the optimization algorithm.
- d) Labor costs: calculated using average monthly salary information available at the Datafolha website [108].
- e) Investment: calculated considering a normalized wheel cost, by Eq. (25), which assumes the cost for grinding wheels with 100% sol-gel alumina content as 2.5 times the cost of electro-fused alumina. The volumetric phase fraction for the abrasive grit content was also taken into consideration, in accordance with the values analyzed by X-ray microtomography.

$$C_{\text{GW}} = \frac{V_g}{100} \cdot \left(\frac{C_{\text{EF}} \cdot V_{g, \text{EF}}}{100} + \frac{C_{\text{SG}} \cdot V_{g, \text{SG}}}{100} \right) \quad (25)$$

where:

C_{GW} is the grinding wheel relative cost

V_g is the volumetric abrasive grit concentration [%]

C_{EF} and C_{SG} are the electro-fused and sol-gel aluminum oxide abrasive grits relative cost, respectively [-]

$V_{g, \text{EF}}$ and $V_{g, \text{SG}}$ are the electro-fused and sol-gel aluminum oxide abrasive grits concentrations, respectively

- f) Product life: for the last indicator, a model was developed based on the influence of the grinding process on fatigue life, as means to employ information of the boundary-affected layer, normally not included in a sustainability evaluation. This indicator uses a surface texture model for fatigue life, based on Zeng's study [109], which defines a stress concentration factor K_{st} due to the many valleys present on the surface roughness. This model is referenced by Eq. (26)

$$K_{st} = 1+n \cdot \left(\frac{R_{Sm}}{R_z}\right)^{0.5} \cdot \left(\frac{R_a}{\bar{\rho}}\right) \cdot \left(\frac{R_t}{R_z}\right) \quad (26)$$

where:

$\bar{\rho}$ is the equivalent root radius of valleys and represents the average value of root radii measured from several prominent profile valleys [μm]

R_z is the ten-point height parameter [μm]

R_t is the max peak-valley height parameter [μm]

n is the load constant, dependent on the type of loading, n equal to 1 means the ideal sinusoidal surface subjects to shear stress from torsion loads; n equal to 2 represents the ideal sinusoidal surface subjects to normal stress from tensile or bending loads [-]

Since the boundary-affected layer also influences fatigue life, it is also important to consider these aspects of the proposed indicator. Using data from the surveyed literature (Table 12), an extremely simplified exponential equation was elaborated.

Table 12 – Effect of machining processes on the fatigue life of components.

Reference	Process	Tool	Material	BAL thickness	Fatigue test	Fatigue life N_f	
						Stress	Life multiplier
Gao <i>et al.</i> [110]	Cylindrical grinding	-	GH4169	120 μm	Four-point-rotating bending	850 MPa	0.10 times
Smith <i>et al.</i> [111]	Cylindrical grinding	38A 100-H8VBE	AISI 52100	10 μm	Rolling contact fatigue	1300 MPa	0.25 times
Hashimoto <i>et al.</i> [112]	Cylindrical grinding	Vitrified Al_2O_3	AISI 52100	18 μm	Rolling contact fatigue	4500 MPa	0.50 times
Choi [113]	Face turning	cBN	AISI 52100	50 μm	Rolling contact fatigue	2724 MPa	0.15 times

Source: Author.

The equation that considers that a boundary-affected layer of 0 generates a fatigue life of 100% ($N_f = 1 \times 10^6$ cycles), is Eq. (27)

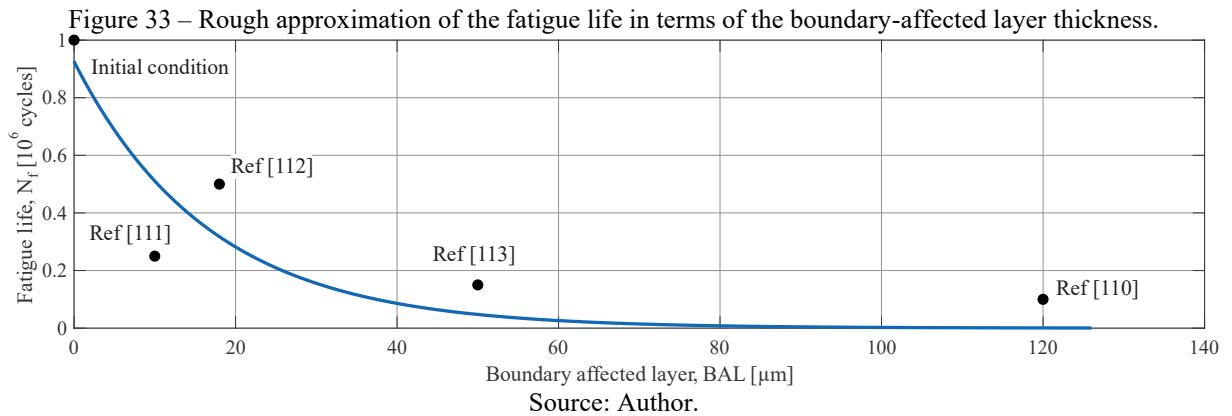
$$N_{f, \text{BAL}} = 0.92 \cdot e^{-0.059 \cdot \text{BAL}} \quad (27)$$

where,

$N_{f, \text{BAL}}$ is the fatigue life influenced by the boundary-affected layer [10^6 cycles]

BAL is the boundary-affected layer thickness [μm]

The exponential approach obtained a coefficient of determination (R^2) of 0.72, as depicted in Figure 33.



The decision-making parameters (degree of fulfillment DF, weight factor WF, and utility value U) were calculated according to the methodology compiled by Linke *et al.* [114], Zhang and Haapala [115], and Linke *et al.* [116].

4 RESULTS AND DISCUSSION

This chapter emphasizes on showcasing the obtained results for the evaluated conditions.

In the first section introduces the grinding wheel characterization using X-ray microtomography technique. In the second section, results for the stage I methodology were presented and discussed. In the following section, results for the stage II methodology were evaluated.

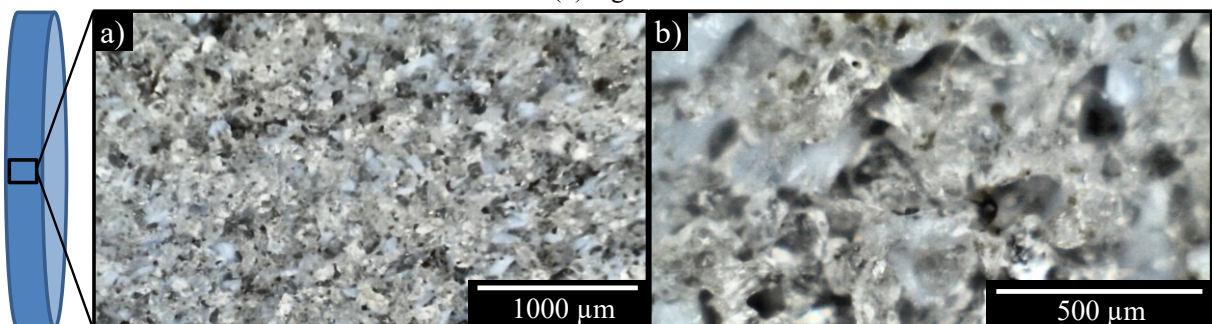
In the last section, the grinding wheels are compared in terms of the life cycle inventory analysis, using the selected sustainability indicators as a decision-making tool.

4.1 GRINDING WHEEL CHARACTERIZATION

The manufacturing procedure of conventional grinding wheels is not without its faults, as even though it follows a specific route, properties derived from the pore/binder/abrasive grit concentrations and distributions may greatly vary within the tool [117]. Additionally, the information/specification passed down by the grinding wheel manufacturer label, following the normative, is a qualitative value.

In an initial analysis of the grinding wheels, optical microscopy imaging of the wheel periphery was performed (Figure 34). The granular structure is easily identified, with hints of the presence of the microcrystalline aluminum oxide visible (blue phase) and of the binder (translucid phase) but no further information is possible to extract out of the image analysis.

Figure 34 – Optical image of the MC45 grinding wheel periphery, with different magnifications: (a) lower and (b) higher.

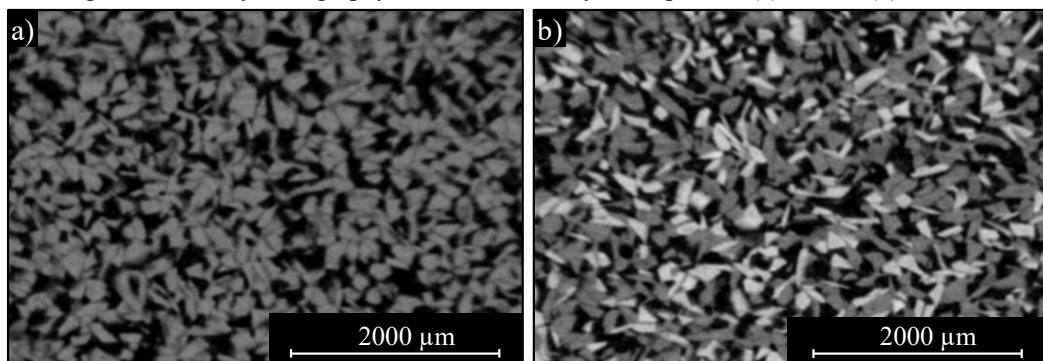


Source: Author.

If the sought information of the grinding wheels was used solely to evaluate in detail the phases fraction, the optical images would be considered enough. A flattened grinding wheel

surface would grant the necessary conditions to such evaluations. However, the tomography analysis presented a suitable option, as well as increased the variety of information extracted from a sample. To do so, a 10 mm OD cylinder, with 30 mm length, was removed axially from the periphery of the MC00 and MC45 grinding wheels and characterized by employing the X-ray microtomography technique. This initial image acquisition (Figure 35) was performed to detect the differences in extreme differential compositions of the studied grinding wheels.

Figure 35 – X-ray tomography of the Ø 10 mm cylinder probes: (a) MC00, (b) MC45.



Source: LMPT [102].

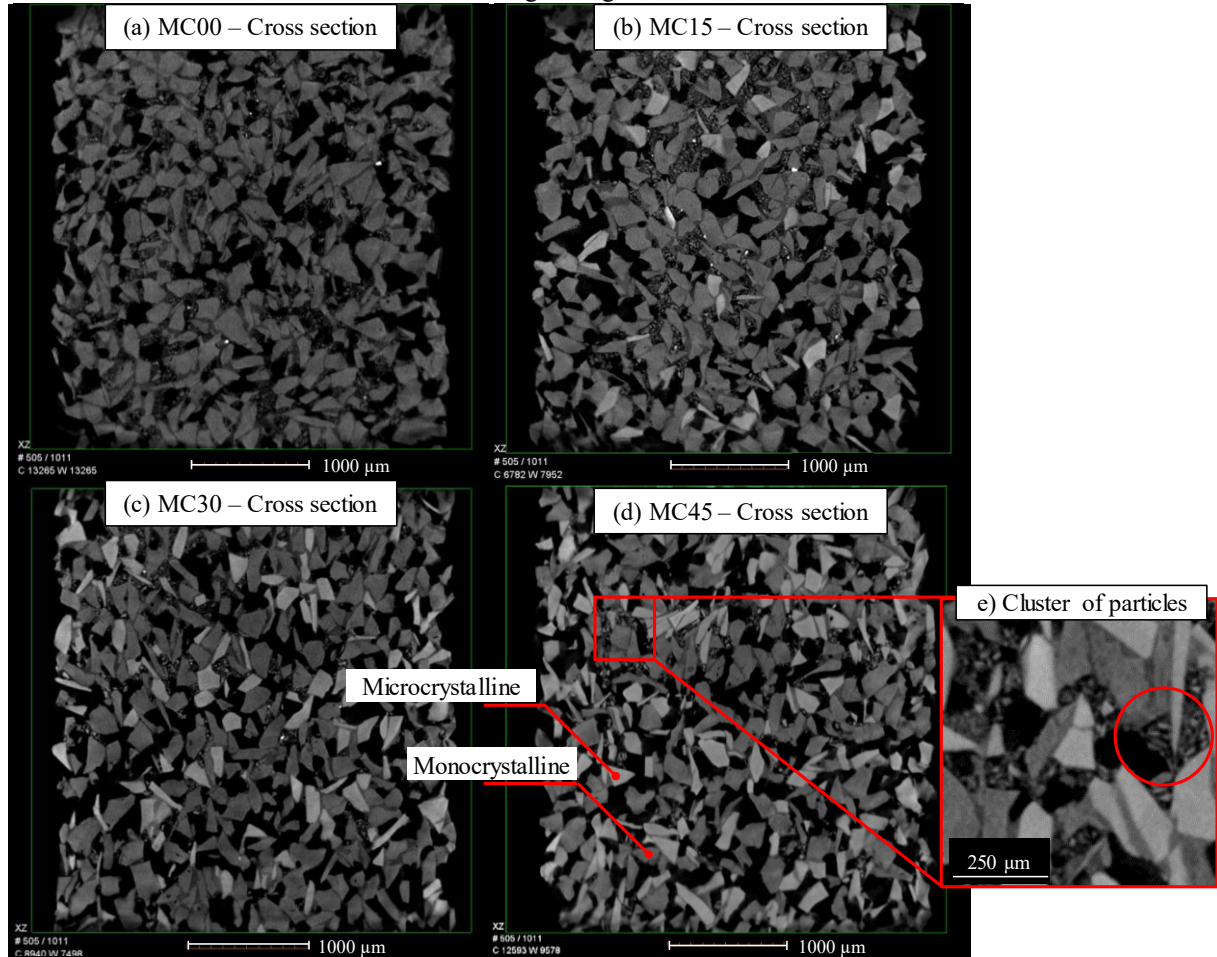
An interesting feature observation concerns the presence of microcrystalline aluminum oxide. Since image contrast and shade level is due to differences in phase density, it would be expected that both aluminum oxide abrasive grits presented a similar shade. However, this was not the case, as observed in Figure 35b. A brighter shade is observed for the microcrystalline aluminum oxide, whereas the monocrystalline aluminum oxide presented a shade level similar to the binding system. Bot-Schulz [118] has noticed the same differences when observing images of electro-fused/sol-gel Al_2O_3 using the tomography technique. However, it was still not possible to distinguish the binder phase from the monocrystalline abrasive grit phase.

In order to further characterize the grinding wheel, smaller sections of the grinding wheel were removed, increasing the spatial resolution. Samples of the MC00, MC15, MC30 and MC45 were evaluated further trepanned out of the wheels (4 mm OD and 10 mm in length). The analysis was conducted in terms of phase segmentation and separation. Images of the pores, binder and abrasive grits (divided into monocrystalline and microcrystalline Al_2O_3) were obtained, as Figure 36 depicts.

Unlike the larger samples (consequently with poorer spatial resolution), the second characterization allowed an in-depth observation (higher spatial resolution) of the different phases contained within the grinding wheel probe. The bonding system, previously mixed with the monocrystalline phase, now is discernable. The overall phases, executing a simple

observation, are evenly distributed along the volume of interest. The brighter phases, previously identified as microcrystalline aluminum oxide, show an increase in concentration, following the grinding wheel's nomenclature.

Figure 36 – X-ray tomography images of the samples, showing the distribution of phases for the experimented grinding wheels.

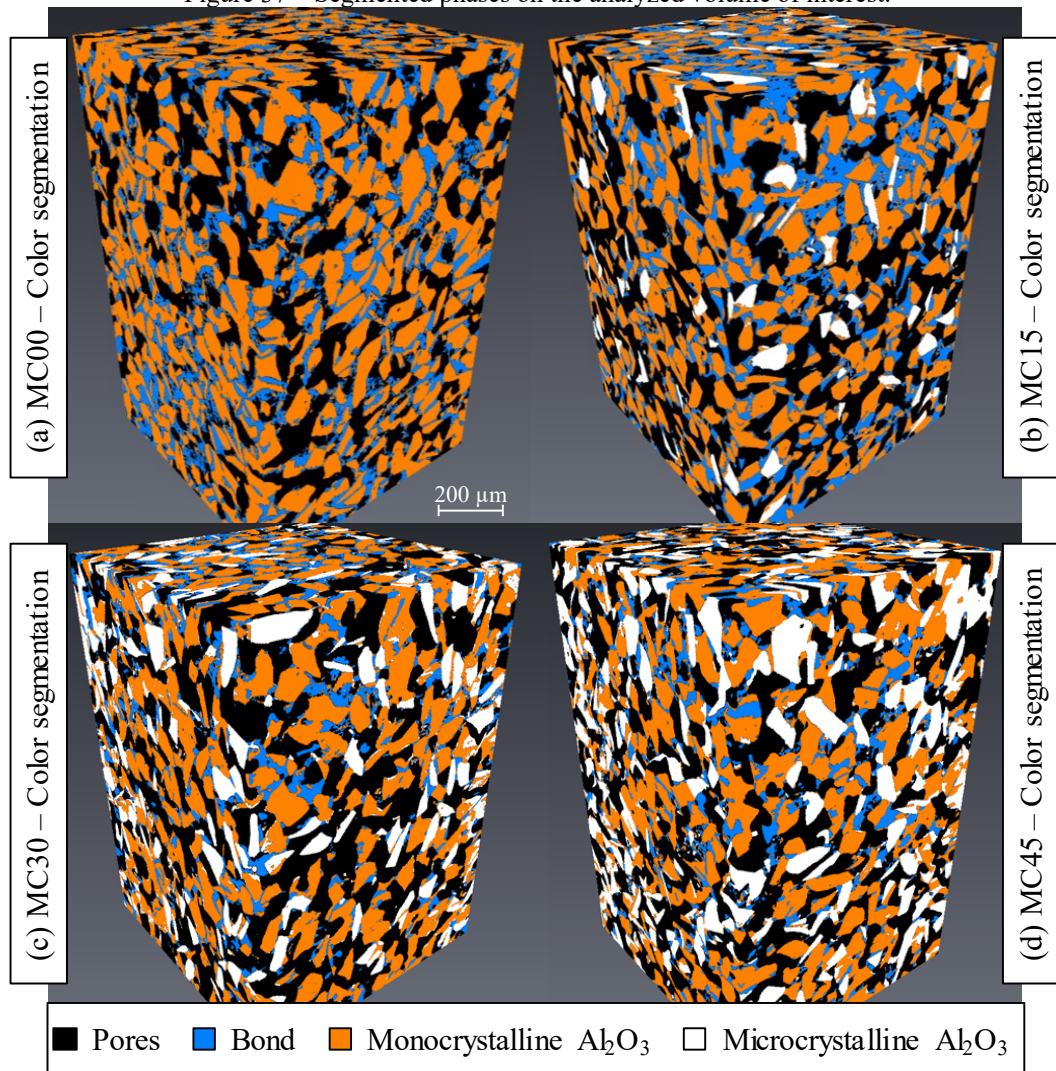


Source: LMPT [102].

Along with the phase identification, it was possible to identify, in a few zones, clusters of particles of smaller sizes than the presented structures (Figure 36e). These clusters are in the vicinity of the abrasive grit phases, which might reveal said particles as part of the bonding system, particularly a portion that was not molten during the grinding wheel manufacturing.

Using the Watershed segmentation (performed in the Avizo software), an algorithm based on the representation of a grayscale image as a topographic relief, flooded with water, where watersheds are lines dividing areas of the water from different basins [119]; the obtained images were segmented (Figure 37).

Figure 37 – Segmented phases on the analyzed volume of interest.



Source: LMPT [102].

It is noticeable the increasing amount of microcrystalline phase (in white) from MC15 sample (Figure 37b) until MC45 (Figure 37d).

To assure that the obtained images are enough representative of the samples, a representative elementary volume (REV) test was accomplished. For all samples, the values of porosity converge to a stabilized value was 300 – 350 voxel cubes, smaller than the cropped analyzed volumes of interest.

The results obtained by X-ray tomography show that the MC00 and MC15 samples are different from the MC30 and MC45 samples. The volumetric fraction of abrasive grits (V_g) is approximately 5% lower for the MC00 and MC15 samples, whereas the pore fraction (V_p) of the MC30 and MC45 samples are 6% higher than the MC15. This results in a difference of binder fraction (V_b) of 11%, Table 13 **Erro! Fonte de referência não encontrada.**

Table 13 – Average volumetric phase fraction concentration according to different grinding wheels, considering a cylinder of Ø 4 mm x 4 mm.

Sample	Phase	Volumetric phase fraction	Total volumetric phase fraction
MC00	monocrystalline	51.2%	$V_g = 51.2\%$
	binder	21.8%	$V_b = 21.8\%$
	pore	27.0%	$V_p = 27.0\%$
MC15	microcrystalline	6.7%	$V_g = 49.8\%$
	monocrystalline	43.1%	
	binder	21.5%	$V_b = 21.5\%$
	pore	28.6%	$V_p = 28.6\%$
MC30	microcrystalline	16.4%	$V_g = 54.3\%$
	monocrystalline	37.9%	
	binder	9.3%	$V_b = 9.3\%$
	pore	33.8%	$V_p = 33.8\%$
MC45	microcrystalline	21.8%	$V_g = 54.9\%$
	monocrystalline	33.1%	
	binder	10.3%	$V_b = 10.3\%$
	pore	34.8%	$V_p = 34.8\%$

Source: LMPT [102].

It is believed that concentration change for the grinding wheels was an intentional manufacturing step as a means to maintain the grinding wheel hardness classification at a similar level. This information was verified when comparing with grinding wheel hardness by sandblasting, provided by the manufacturer. The hardness for all grinding wheels was kept at a constant magnitude of 50 GPa.

The hardness by sandblasting test entails that a volume of sand of 20 cm³ is propelled onto the grinding wheel with compressed air. The depth of the crater blown out of the grinding wheel is measured by means of test needles. This represents the measure for the bond hardness of the grinding wheel [21]. Although an ease procedure, the reliability of the test diminishes, as attested to this study.

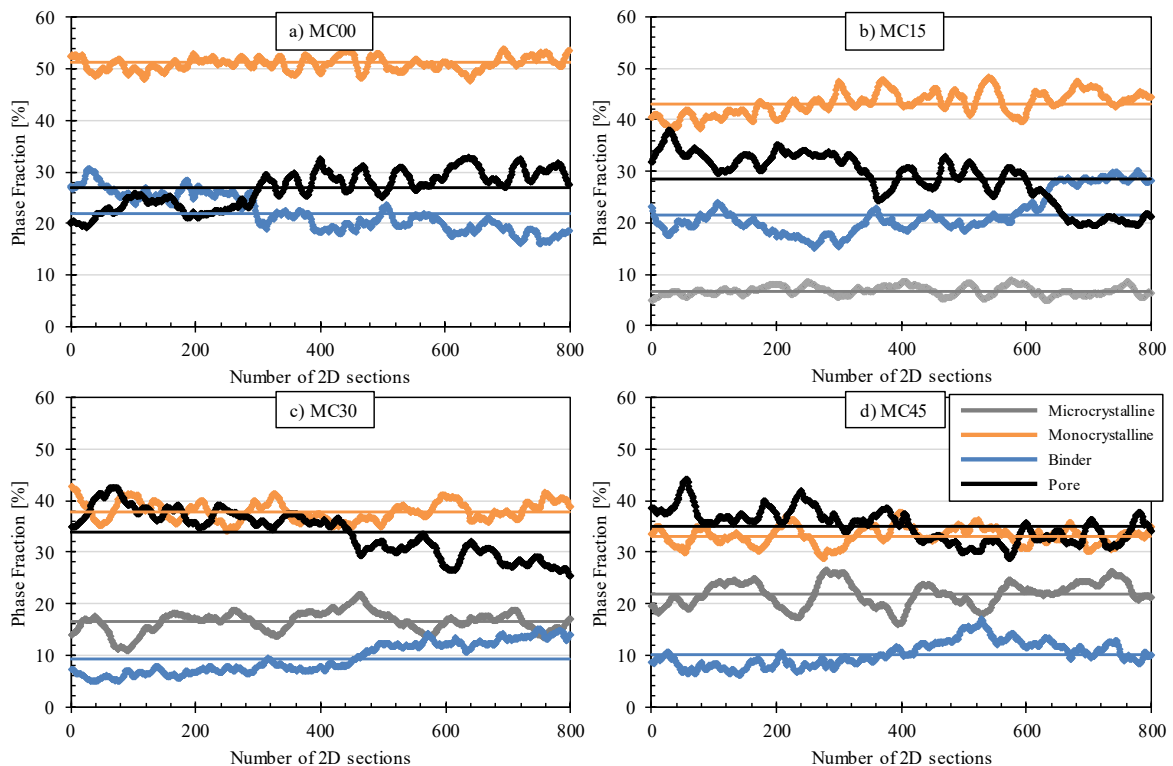
Other method that is commonly used to evaluate grinding wheels is the impulse excitation technique (GrindoSonic) [120], which relies on reaching the resonance frequency of the grinding wheel and correlations with the physico-mechanical properties of the material mass (such as hardness, porosity, density, strength, etc.), to determine the natural frequency, speed of sound, modulus of elasticity, hardness of the product. While a non-destructive test, relies on prior knowledge of the grinding wheel structure, information not readily accessible.

Since the microcrystalline abrasive grits present a rougher and more irregular surface than the monocrystalline abrasive, the irregular surface increases the real contact area and thus induces a higher area of anchorage (as evidenced by Klocke [21] and Fathallah et al. [16],

Figure 9 and Figure 12, respectively) and, consequently, stronger binding forces. Therefore, to consistently remove the same depth of abrasives (by using the sandblasting hardness test), a lower binder content is necessary and thus, effectively changing the grinding wheel's composition. This modification effectively changes the grinding wheel "hardness behavior" in the micro-scale, meaning that when cutting mechanism is considered, the grinding wheel with the higher content of binder material holds the abrasive grits more effectively, reducing the cutting edge renewal.

The abrasive grit volumetric concentrations are also similar to the manufacturer's specifications. Considering a 100% of abrasive content as a mixture of the two abrasives, the microcrystalline/monocrystalline Al_2O_3 average ratio was: MC15 (13.5%/86.5%), MC30 (30.2%/69.8%), and MC45 (39%/61%). The phase distribution along the cylinder's length was also evaluated in Figure 38 shows.

Figure 38 – Phase fraction for the different grinding wheels: (a) MC00; (b) MC15; (c) MC30; and (d) MC45.



Source: LMPT [102].

The abrasive grits (monocrystalline and microcrystalline Al_2O_3) illustrated an evenly distributed phase fraction, whereas the pores and binder showcased a tendency to increase or decrease the phase fraction around a mean line. It is shown that the pores and binder have an inverse correlation.

These results obtained by tomography expose that the manufacturing route of the grinding wheels, label information of the grinding wheel hardness (obtained by sandblasting) and GrindoSonic procedures do not deliver enough information to specify the characteristics of the tools. It is expected that, with those measured phase fractions, a discrepancy in the efficiency and in the obtained results. Therefore, controversial results are expected.

The obtained results also illustrate the potential application of the X-ray microtomography of grinding wheels as a possible technique for evaluating and certifying the quality of grinding wheels, opening fields of analysis to further characterization in the field of grinding research and, more importantly, as a quality investigation for the manufacturing industry.

4.2 STAGE I – SINGLE-STEP ROUGH GRINDING CYCLE

4.2.1 Grinding force components, F_t' and F_n'

The grinding force components behavior during grinding represents the overall process, especially the abrasive grit wear behavior. Monitoring the grinding force allows an investigation of energy generation on the cutting zone and, therefore, to understand material modifications. In this scenario, Figure 39 shows the behavior of the specific grinding force components for the employed grinding wheels and with increasing specific material removal V_w' and Q_w' ($4 \text{ mm}^3/\text{mm}\cdot\text{s}$), when grinding AISI 1040 steel probes.

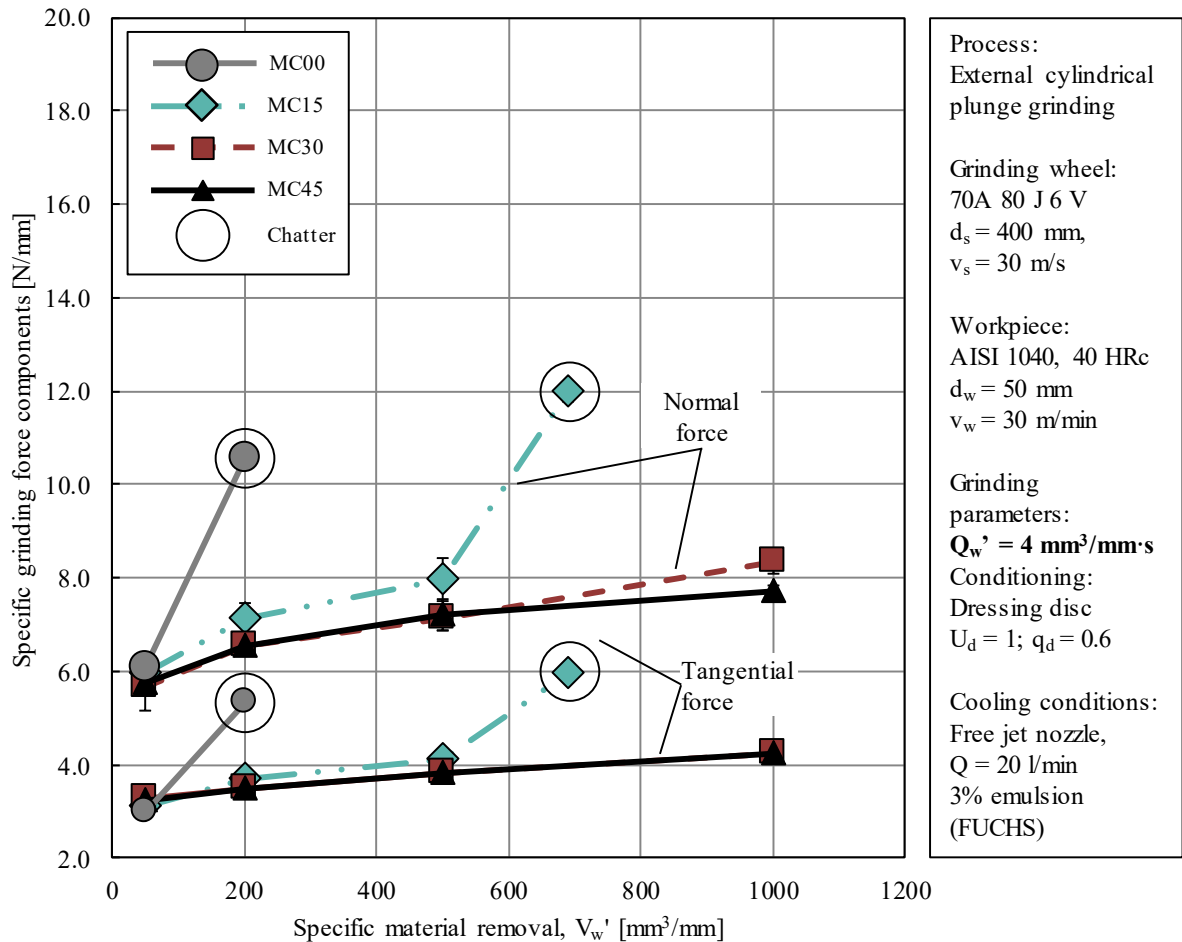
The behavior of the specific grinding force components (F_t' and F_n') illustrates a typical scenario when applying aggressive dressing conditions. A quasi-proportional increase of the grinding force components after dressing for the four applied grinding wheels. The initial grinding force components are almost equal.

For the pure monocrystalline aluminum oxide and the three grinding wheels with microcrystalline aluminum oxide content, with a specific grinding rate of $4 \text{ mm}^3/\text{mm}\cdot\text{s}$, the dominant micro-wear of the abrasive grits' along grinding cycle was recognized by an increase in the grinding force components as a function of the ground volume.

The MC00 wheel and MC15 showed a shorter cycle life, and chatter was observed after grinding of 300 and 700 mm^3/mm , respectively. What was surprising was that the force components for the lowest specific grinding rate increased to a high level, without presenting a grit sharpening the effect, which would have been expected for the monocrystalline grits (MC00) and for the MC15 (considering the same grinding wheel hardness).

The dominant wear for the MC00 and MC15 should be the monocrystalline grit chipping, causing a stabilization or a decrease of the kinematic cutting edges ($V_w' = 50 \text{ mm}^3/\text{mm}$), however, the high increase of grinding force components would only be possible if the wheel presents a higher hardness. This result was confirmed by the X-ray tomography analysis of the grinding wheels.

Figure 39 – Specific grinding force components with increasing V_w' .



Source: Author.

The fact that the MC00 and MC15 grinding wheels present a higher binder content hinders the MN abrasive breakage and, due to the flattened abrasive, the plowing mechanism becomes a larger influence during the cutting. Unable to efficiently remove the material, grinding force components rises, until it reaches a chatter condition (last V_w') due to the system's low stiffness.

Observing the grinding force components for the MC30 and MC45 wheels, as expected, the flattening of the top of the grits leads to a slight increase of the force components. As described in the literature, the effective number of cutting grits increases, lowering the

individual chip thickness and increasing the specific cutting pressure [21]. The regular behavior up to $1000 \text{ mm}^3/\text{mm}$ of ground material indicates that the cutting capacity of the grits is almost maintained. With the increase of the microcrystalline MC grit content, the effect of the monocrystalline MN abrasive grit diminishes, shifting the main wear mechanism to the microcrystalline grains, which wear more intensely by flattening of the grits by abrasive mechanisms.

Due to the lower binder content and lower real area of anchorage, the MN grits break out earlier and the reduced number of kinematic MC grits increases the load on the individual MC grits. This occurrence should lower the total force components, because of the increase of the uncut chip thickness for each grit.

However, the situation differs from the expected behavior. The higher tenacity of the MC grains permits a higher grinding force on each grain, which is distributed on several micro-edges along the top of each grain. The abrasive wear of the MC grains flattens the top of the grits, increasing the number of kinematic active grains, each of them with micro-cutting edges, leading to a slight increase of the grinding force components, but withstanding for a longer grinding time.

These behaviors only intensified with an increase in the specific material removal rate to $5 \text{ mm}^3/\text{mm}\cdot\text{s}$, as can be observed in Figure 40.

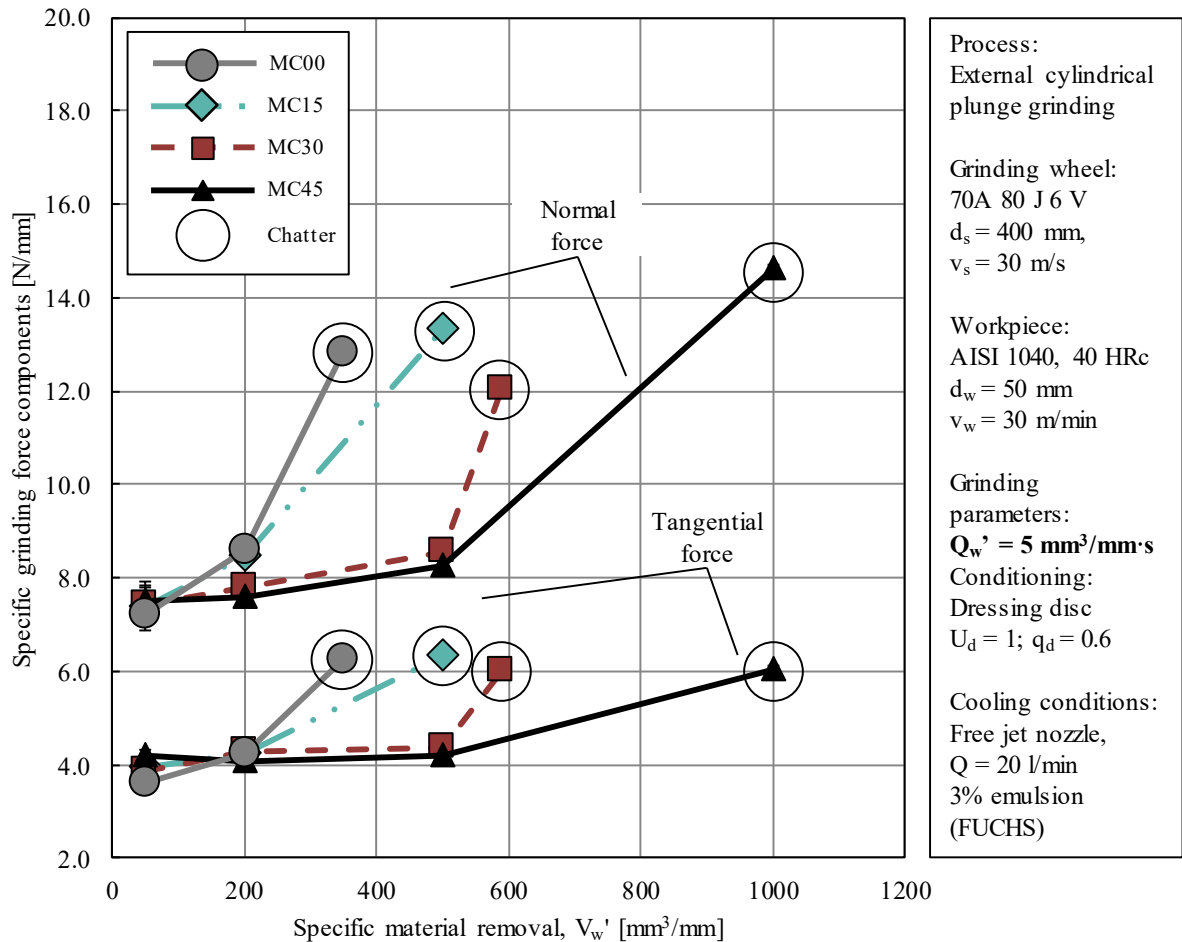
Aside from the increasing magnitude of the force components, in comparison to the previous Q_w' , the overall behavior followed a similar trend. The Q_w' increased, in this case, by increasing the depth of cut (v_w remained at a constant level). With this increment, the chip thickness h_{cu} increases, so do the number of kinematic cutting edges partaking on the cutting action, increasing the grinding force on the cutting direction. Since the contact length and area augments, the normal force also increases to keep a constant grinding pressure.

Initial grinding force presented a similar magnitude for all tested grinding wheels. However, with the increase of the wear, the distinction between the grinding wheels became evident as the force spiked, caused by wear and leading to intense chatter, interrupting the experiments.

Higher microcrystalline content meant longer stability along with the grinding wheel life. MC45 reached the specific material removal criteria established in the methodology section, while during the MC30 experiments (contrary to the previous Q_w'), the test was interrupted. The MC00 and MC15 reached the lowest V_w' of all conditions. All the grinding wheels illustrated chatter at the end of the grinding cycle.

The fact that the grinding wheels reached the chatter condition, even for a higher specific grinding rate, implies that the micro-wear mechanism is still the dominant mechanism and grit flattening, the dominant wear type. The results from the MC00 and MC15 grinding wheels still reflect the evidence of higher binder content hindering the chipping of the abrasive grits. This behavior is likely to occur in all the experimented conditions.

Figure 40 – Specific grinding force components for a Q_w' of $5 \text{ mm}^3/\text{mm}\cdot\text{s}$.



Source: Author.

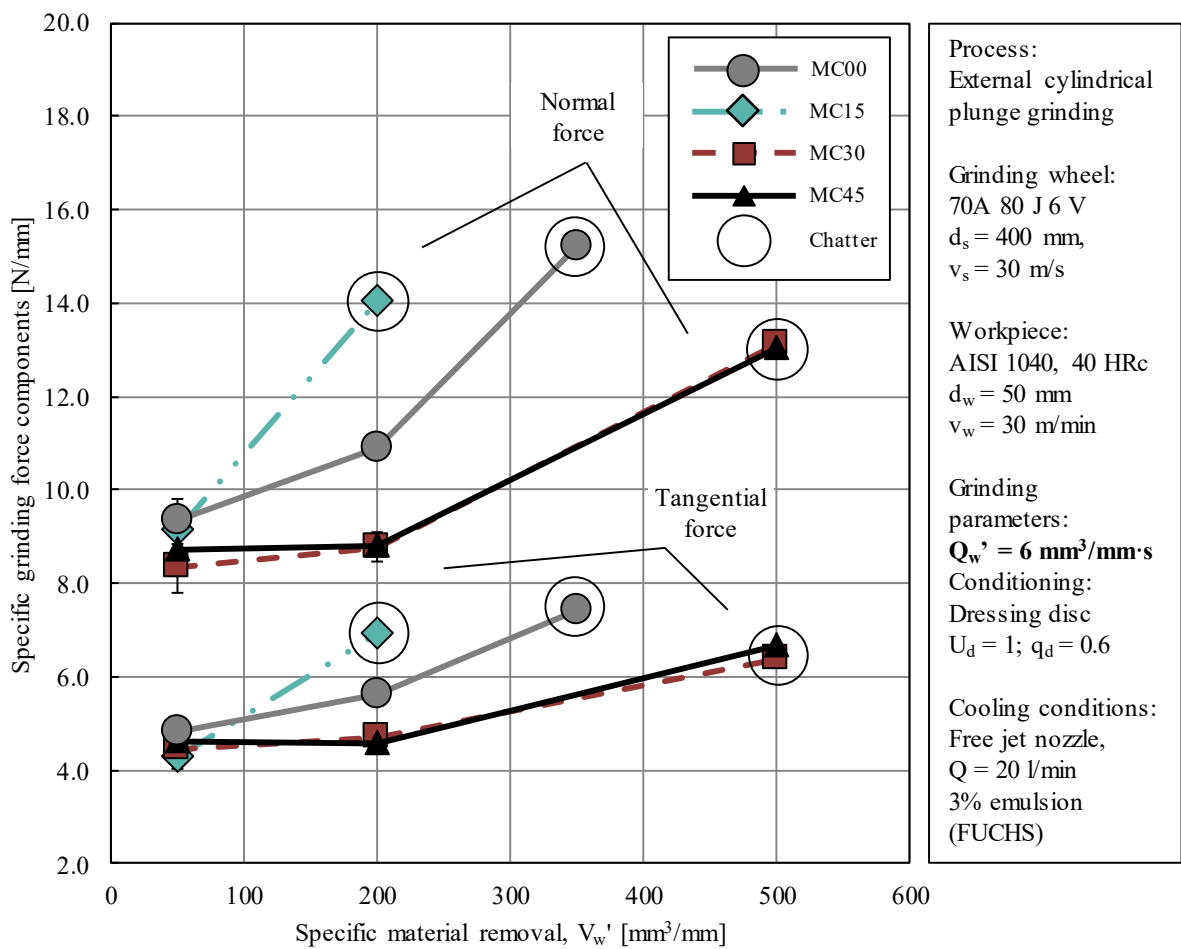
Further increasing the specific material removal rate to $6 \text{ mm}^3/\text{mm}\cdot\text{s}$ (Figure 41), the previously observed trends repeat itself.

As far as the grinding wheel content is concerned, MC15 reached the peak of grinding force after only machining $200 \text{ mm}^3/\text{mm}$. For the other conditions (MC30 and MC45), similar behavior and specific grinding force magnitude were achieved.

Chatter was identified as the main source of the grinding wheel end of life cycle. These results are in agreement with the previous specific material removal rates, however, are not consistent with the literature, even more for the MC15 grinding wheel.

Surprisingly, different from the previous Q_w' , the MC00 grinding wheel illustrated a slightly longer life than the MC15. This is not consistent with the previous tested conditions. It is hypothesized that the presence of solely MN- Al_2O_3 as abrasives led, in this condition of higher mechanical severity, to the abrasive grit breakage, causing a reduction on the grinding force components and increase on the MC00 grinding wheel's life. However, this is still not enough to generate a consistent and stabilized condition of cutting edge renewal (self-sharpening) due to the higher binder content.

Figure 41 – Specific grinding force components for a Q_w' of $6 \text{ mm}^3/\text{mm}\cdot\text{s}$.

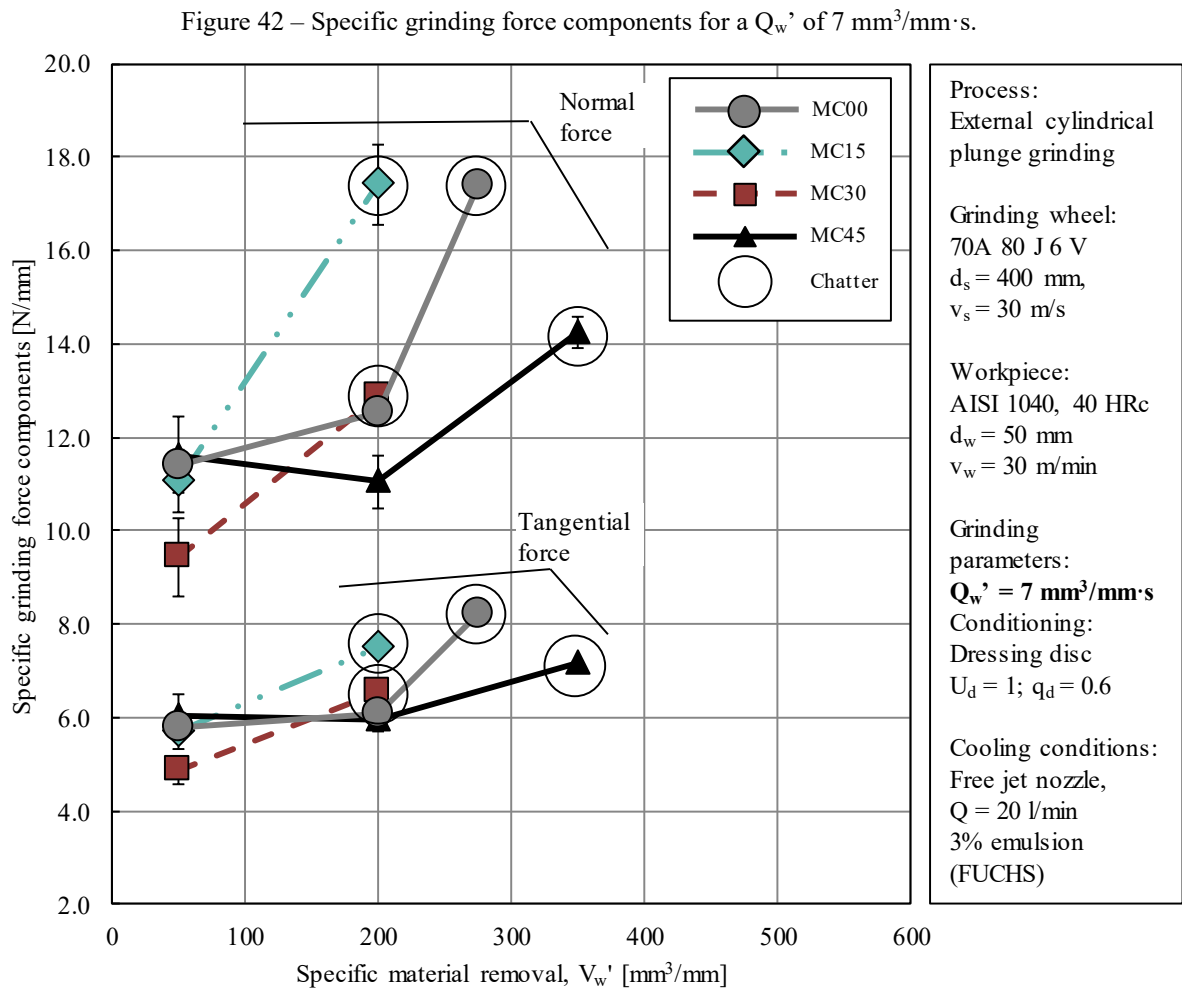


Source: Author.

Further increasing the specific material removal rate to a value of $7 \text{ mm}^3/\text{mm}\cdot\text{s}$ (Figure 42), a shorter grinding wheel life for all conditions was observed.

Contrary to previously displayed results, the initial grinding force ($V_w' = 50 \text{ mm}^3/\text{mm}$) illustrated larger differences. MC45 condition yielded the highest force magnitude, followed by the MC15 and MC30 conditions and lastly MC30 grinding wheel application.

Both MC15 and MC30 only withstood a specific material removal of 200 mm³/mm, while the specific grinding force components magnitude for the 45% microcrystalline Al₂O₃ content kept a stable (and equal level) for a V_w' of 200 mm³/mm, ultimately increasing to a spike at 350 mm³/mm. In a similar behavior with the previous specific grinding rate, the wheel without MC content withstood a higher volume than the MC15 grinding wheel, as well as the same V_w' as the MC30 grinding wheel.



Source: Author.

At this specific material removal rate of 7 mm³/mm·s, the total ground volume was shorter and, therefore, the influences of the chatter behavior can be anticipated, implying in an unusual behavior if compared to the previous specific grinding rates Q_w' .

When grinding with a specific grinding rate of 7 mm³/mm·s, a change in the wear mechanism is deduced from the behavior of the grinding force components when grinding with the MN grinding wheel. The grinding force components remain stable up to a specific ground volume of 200 mm³/mm. This indicates that the tool remains with the same overall sharpness,

which is caused by the splintering of the MN Al_2O_3 grit, maintaining the number of cutting edges stable. The increase of the grinding force components for higher specific ground volumes is due to a not enough wear of the binder with the decrease of the grit protrusion. For none of the other evaluated grinding conditions, this mechanism was observed, indicating that an even higher specific material removal rate should be evaluated, but not possible at the used infrastructure (Zema grinding machine with used Kistler grinding force measuring device and mounting).

As far as the abrasive grit content is concerned, the differences observed for most conditions were not large in magnitude.

All analyzed grinding wheels with specific grinding rates from 4 to 7 $\text{mm}^3/\text{mm}\cdot\text{s}$ illustrated a dominant wear mechanism by abrasion, caused by the loss of cutting capacity, increasing the kinematic cutting edges. No indications of the macro-wear of the grinding wheel grit, which would keep the grinding forces in a stable condition, rather than accelerated chatter.

Also, the results observed for all the specific grinding rates are on par with the expected behavior, considering the X-ray tomography results. The higher binder content hindered the MC00 and MC15 abrasives to fracture and generate new cutting edges. Greater differences could be expected, however, the abrasive volumetric fraction for the MC00 and MC15 was lower which in turn reduces the grinding force components.

The investigated literature disagrees:

Uhlmann *et al.* [121] detected when employing grinding wheels with the same concentrations to those employed in this study, differences of larger magnitudes (larger forces as the microcrystalline content reduced). The grinding force components increased in discrete steps, considering from the highest to the lowest MC content. The authors ground an AISI 52100 bearing steel (60 HR_C) with higher Q_w' (8, 10 and 12 $\text{mm}^3/\text{mm}\cdot\text{s}$) but smoother wheel surface (U_d 3.7).

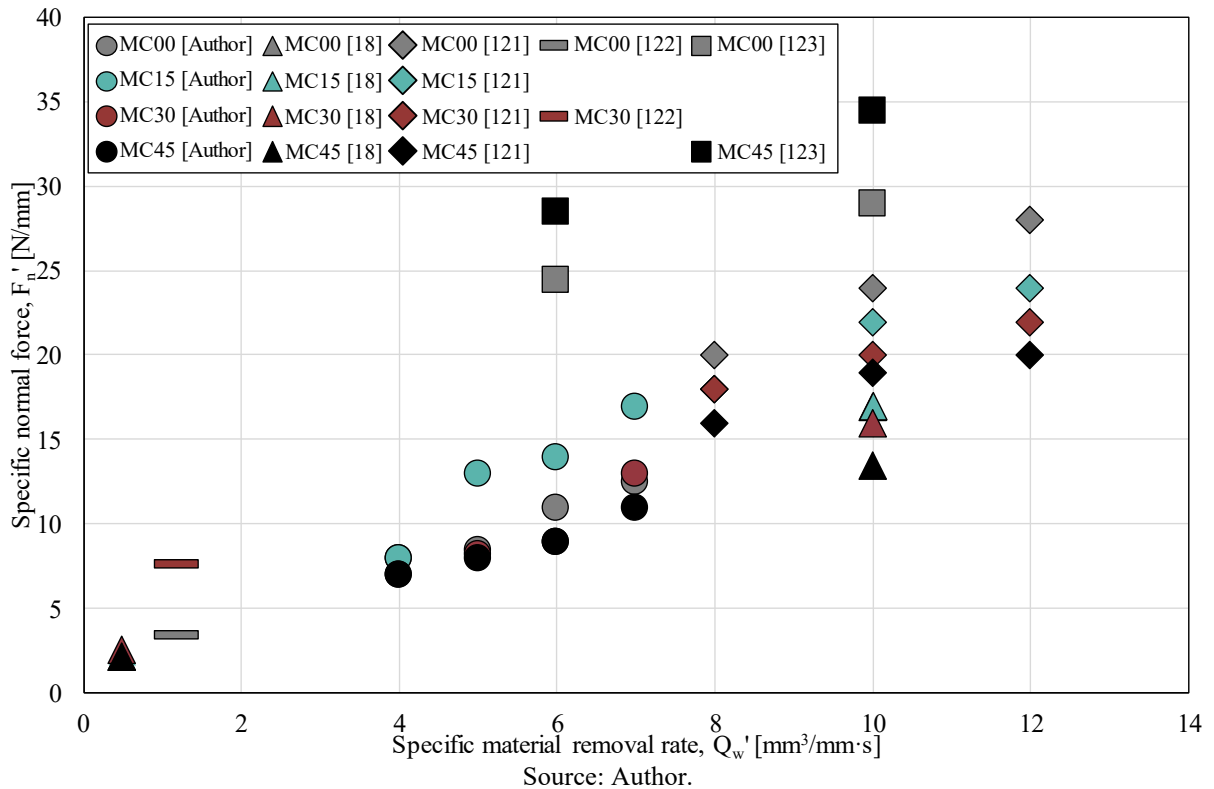
Benini [18] also reported similar results to Uhlmann *et al.* [121], when grinding of an ADI cast iron during the external cylindrical plunge. The sol-gel grinding wheels, with a composition of 0%, 15%, 30%, and 45%, illustrated a decrease in grinding force components with an increase of the sol-gel content. Parameters used were: Q_w' of 10 $\text{mm}^3/\text{mm}\cdot\text{s}$ and an U_d of 3.7.

Madopothula *et al.* [122] observed higher forces for a 30% Al_2O_3 sol-gel abrasive grits grinding wheel, in comparison to a white fused Al_2O_3 . The experiments were performed in a surface grinder when grinding an AISI 52100 bearing steel, increasing the number of passes, with a Q_w' of 1.2 $\text{mm}^3/\text{mm}\cdot\text{s}$ and a high dressing overlap ratio.

Caraguay [123] evaluated the grinding force components in the external cylindrical plunge grinding process of nodular cast iron (290 HB) with wheels of 0 and 45% of MC- Al_2O_3 . The specific material removal rate shifted from 6 to 10 $\text{mm}^3/\text{mm}\cdot\text{s}$ and circumferential workpiece speed of v_w of 10 m/min. In the author's studies, the forces were higher for the grinding wheel with 45% of MC abrasive.

The results from this study compared with the results presented in the consulted literature can be observed in Figure 43. The behaviors were compared considering a specific material removal superior to 250 mm^3/mm .

Figure 43 – Comparison of specific normal force versus specific material removal rate for various input parameters.

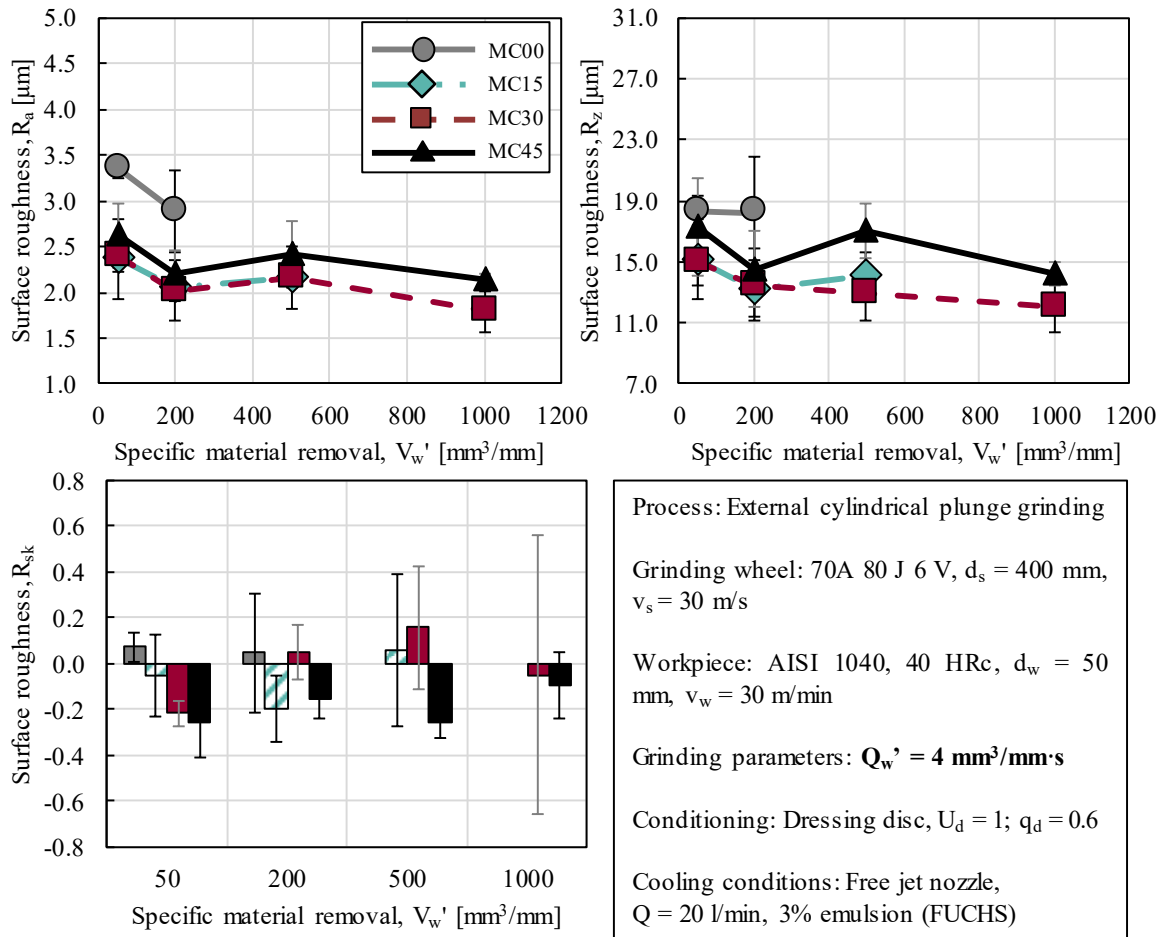


In these conditions, specific material removal rates below a threshold of 2 $\text{mm}^3/\text{mm}\cdot\text{s}$, the forces for the grinding wheel with MC aluminum oxide were equal or higher than monocrySTALLINE aluminum oxide. There is a predominance of higher forces for the lowest content of MC alumina endowed wheels. The exception is presented in the studies performed by Caraguay [123], where the highest forces were observed for the highest microcrystalline content.

4.2.2 Surface roughness

Surface roughness is a topography profile measure usually associated with surface quality, as well as being associated with some mechanical phenomena (*e.g.* fatigue behavior, etc.) or functions (*e.g.* bearing ratio, oil retention, etc.). However, a ground surface after a roughing cycle does not aim such aspects, but rather represents the result of the overall abrasive grit interaction with the material, as well as indicating the grinding wheel wear state. In this aspect, surface roughness parameters (height R_a , R_z and shape R_{sk}) are presented and discussed in this section. Figure 44 illustrates the obtained surface when considering a specific material removal rate of $4 \text{ mm}^3/\text{mm}\cdot\text{s}$.

Figure 44 – Surface roughness parameters for a Q_w' of $4 \text{ mm}^3/\text{mm}\cdot\text{s}$.



Source: Author.

A typical representation of the grinding wheel wear evolution with the increasing V_w' is illustrated. The vertical parameters point towards a higher surface roughness at the initial state, presenting a slight reduction as the volumetric material removal increases ($200 \text{ mm}^3/\text{mm}$)

and remaining at a stable condition ($500 \text{ mm}^3/\text{mm}$) until the experiment is interrupted, at a V_w' of $1000 \text{ mm}^3/\text{mm}$.

The profile generated by the MC00 grinding wheel presented the highest values of surface roughness height, followed by the MC45 grinding. Conditions MC15 and MC30 presented statistically equal values. This is an odd behavior presented by MC00 wheel, since according to the grinding force components presented in the previous section (4.2.1), an increase on the kinematic cutting edges (and consequently decrease on the chip thickness) was expected, lowering the roughness values.

The decrease of vertical surface roughness values (R_a and R_z) with the increase in ground volume V_w' is attributed to the micro-wear of the most protrude grits, revealing and increasing the number of kinematic cutting edges. Since the chip thickness is reduced in this manner, the surface roughness lowers.

In a similar occurrence as the grinding force components, for a medium to high specific grinding rate, a macro-wear driven mechanism would be expected, especially for the MC00 and MC15 grinding wheels, due to the low toughness of the MN aluminum oxide grits. However, the lower surface roughness for the MC15 indicates a predominance of the micro-wear rather than the macro-wear, which corroborates with the force results, supported by the X-ray tomography image analysis.

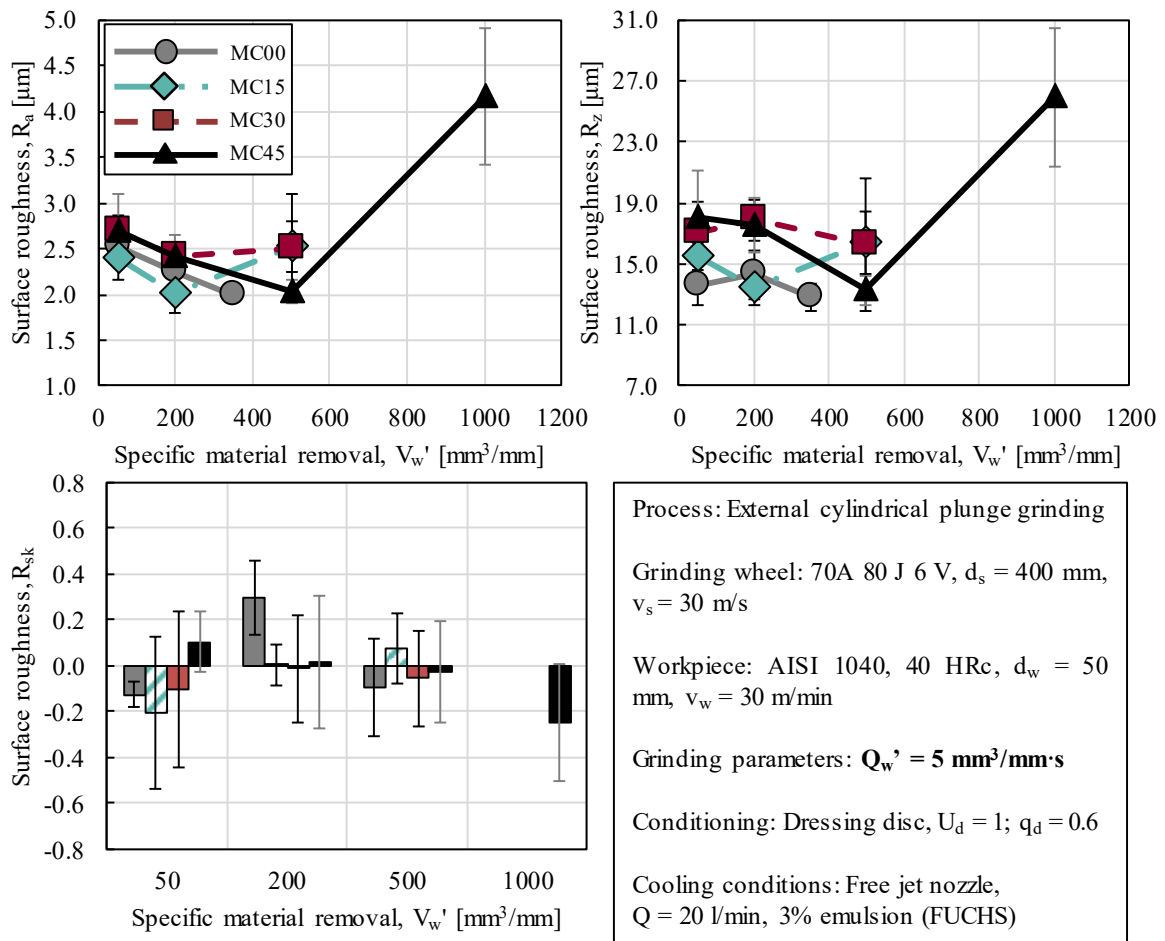
The skewness R_{sk} surface roughness values illustrate, in contrast to the height parameters, shifts on the surface roughness distribution curve. A negative value displays lower/flat peaks or deeper valleys, whereas a positive value indicates flat valleys or sharp peaks. This premise was used to also characterize the ground surface.

The R_{sk} values displayed a slight shift from negative values to positive values with an increase in the specific material removal. This was consistently observed for the MC15 and MC30 condition, whereas the MC45 condition presented predominantly low values. For the MC00 grinding wheel, the R_{sk} values illustrate evenly distributed roughness values and surface texture. Increasing the severity of the process, using a Q_w' of $5 \text{ mm}^3/\text{mm}\cdot\text{s}$, illustrated the following results (Figure 45).

Following a similar trend to the previous results, the initial surface roughness height parameters presented a high value. As the grinding wheel wears, there is an evident tendency to reduce roughness height values. However, as observed for all the last achievable V_w' for each condition: $500 \text{ mm}^3/\text{mm}$ (for MC15 and MC30); and $1000 \text{ mm}^3/\text{mm}$ (MC45), the surface roughness height rapidly increased. The MC00 ground surface, unlike the previous specific grinding rate, illustrated a similar vertical roughness value to the MC15 ground surface.

The spike on the values agrees with the earlier force results, which presented presumably higher wear leading to intense chatter. A chatter frequency, identified in the grinding force components plots, is of 550 Hz. Considering that the workpiece rotation was around 200 min^{-1} (3.3 Hz), it is believed that fluctuation on the specific grinding rate Q_w' occurred, influenced by the chatter amplitude, and thus causing anomalies on the surface profile as well as the specific grinding force components.

Figure 45 – Surface roughness parameter for a Q_w' of $5 \text{ mm}^3/\text{mm}\cdot\text{s}$.



Source: Author.

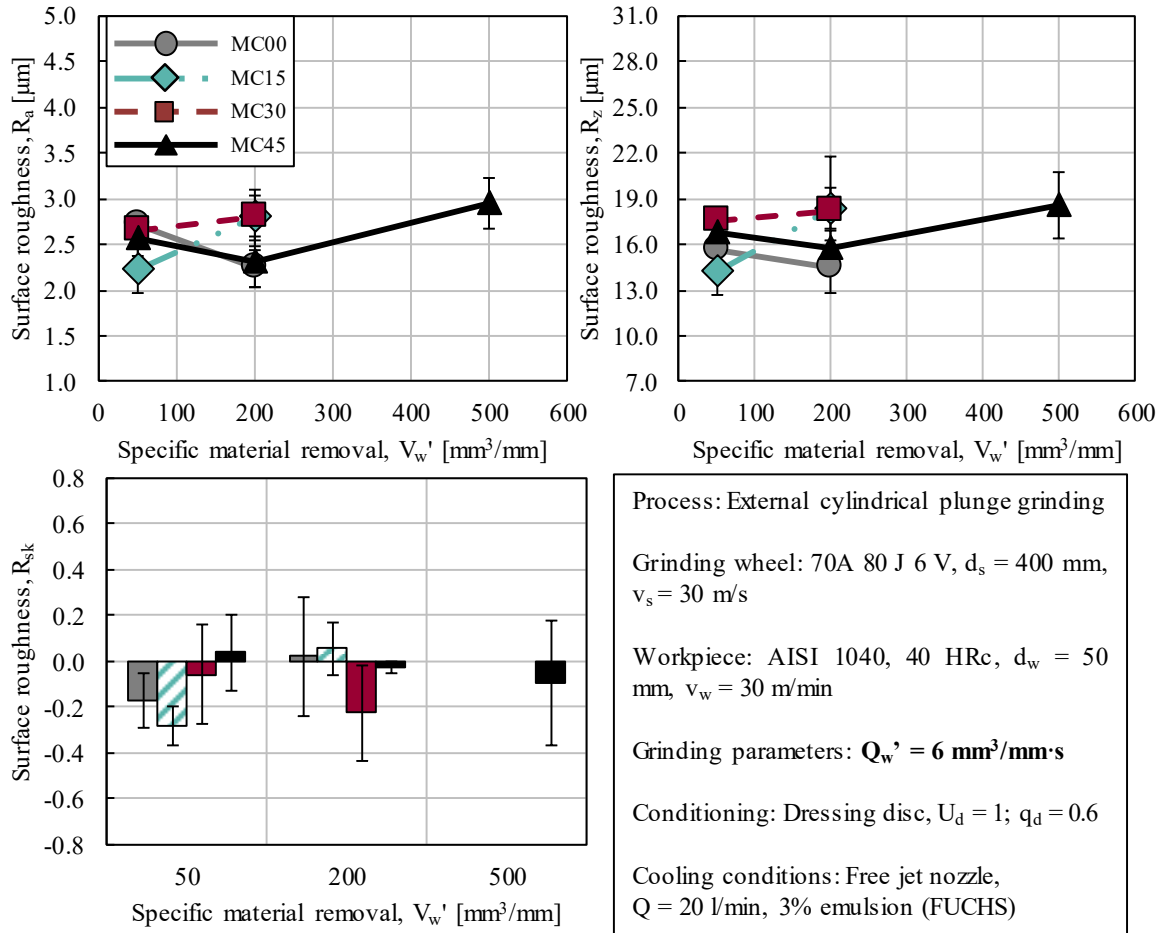
The increase in process severity did not present a distinguishable behavior in terms of the peak-valley distribution (R_{sk}). The distribution is almost evenly scattered around the null line, which indicates a stochastic roughness distribution.

With higher specific material removal rates ($Q_w' = 6 \text{ mm}^3/\text{mm}\cdot\text{s}$, Figure 46), the surface roughness displayed a consistent behavior with the other Q_w' .

The MC00 ground surface exhibited a constant decrease in surface roughness, which is consistent with the grinding force components. However, this decrease is still inconsistent

with the expected wear behavior for the MN dominant grinding wheels. By increasing the grinding rate, large portions of the abrasive grit would splitter along the cleavage plane, generating and revealing sharper new grits, decreasing the number of kinematic grits. The consequences of this behavior would be noticeable by decreasing the grinding force and increasing the surface roughness height parameters.

Figure 46 – Surface roughness parameters for a Q_w' of $6 \text{ mm}^3/\text{mm}\cdot\text{s}$.



Source: Author.

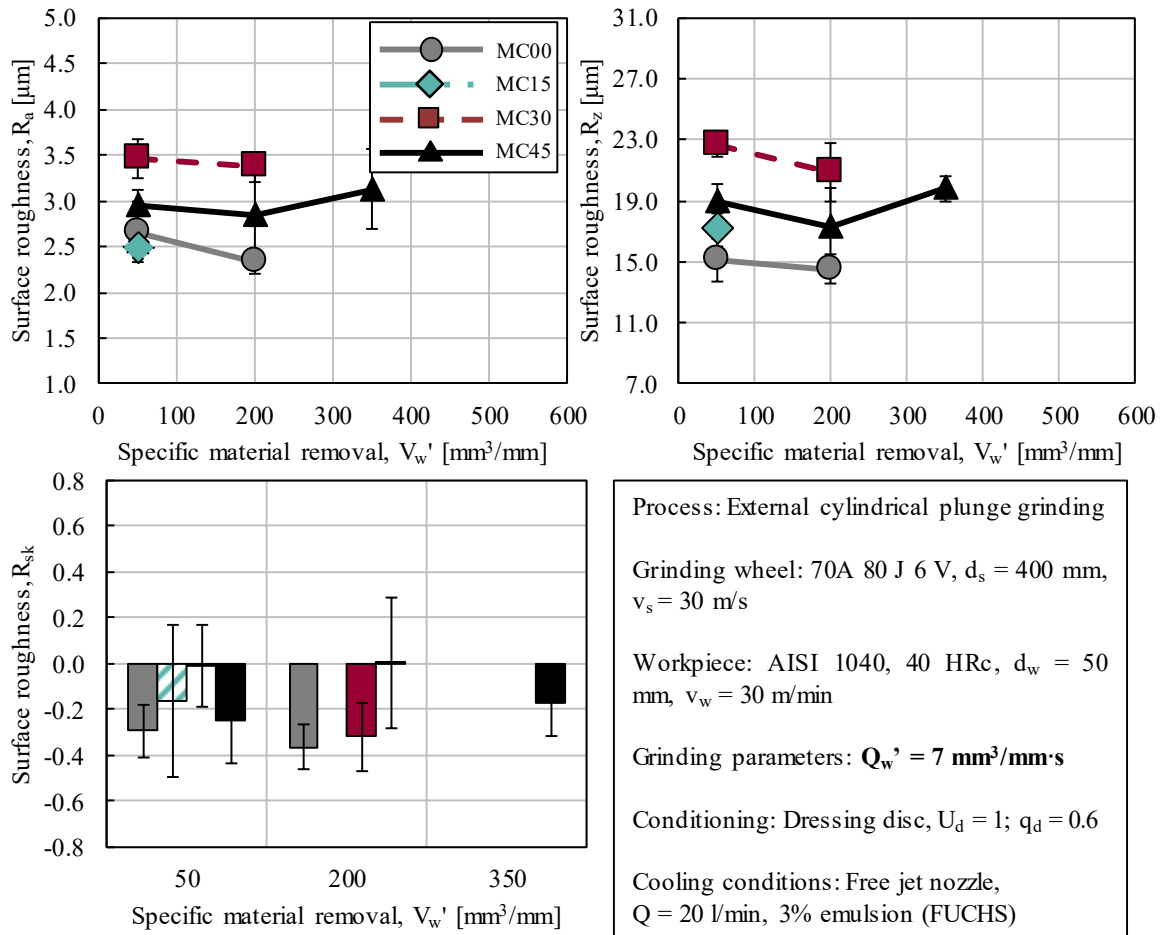
For the same conditions, MC15 and MC30 exhibited an increase/maintenance of the roughness magnitudes; whereas the MC45 grinding wheel reduced its magnitude at the second volumetric interruption, before increasing to a higher value at the end of the machining tests. The specific grinding force for this condition showcased the end of life for the MC00 and MC15 grinding wheels at a V_w' of $200 \text{ mm}^3/\text{mm}$, and $500 \text{ mm}^3/\text{mm}$ for MC30 and MC45. Since the experiments were interrupted midway the testing of the MC30 condition (V_w' of $500 \text{ mm}^3/\text{mm}$), surface roughness values were not evaluated for this condition.

The evident spike on the surface roughness parameters for the MC45 at a ground volume of 500 mm³/mm is attributed, like the previous Q_w' , to the intense chatter.

For the R_{sk} parameter, a similar trend to what was previously observed (for a Q_w' of 5 mm³/mm·s) is present here. MC15 condition shifted from a negative distribution (at the initial stage) to a neutral-positive distribution before cycle interruption. For the MC30 condition, an opposite behavior was observed. MC45 presented an evenly distributed peak-valleys ratio. In a severe machining condition, differentiating the two conflicting grit wear behaviors is difficult and requires further investigations, focusing on the couple grinding wheel profile/surface.

Results obtained for a specific material removal rate of 7 mm³/mm·s represents these aspects (Figure 47).

Figure 47 – Surface roughness parameter for a Q_w' of 7 mm³/mm·s.



Source: Author.

Surface roughness height parameters, R_a and R_z , presented very distinct behaviors for all conditions. For V_w' 's of 50 and 200 mm³/mm, the values remained at a similar value, with a slight increase when MC45 reached its end of life. The ground surface machined with the lowest

MC content illustrated the lowest vertical height parameters, evidenced for even higher ground volumes.

The R_{sk} values demonstrated a negative value for the MC15 condition, whereas increasing the MC content to 30% and initially evenly distributed peak and valleys shifted to predominant valleys (or flat peaks) when increasing the removed material to $200 \text{ mm}^3/\text{mm}$. The surface obtained with the MC45 grinding wheel illustrated initial negative values, that shifted to an even distribution of peaks and valleys, before becoming predominantly negative (predomination of valleys) at the last V_w' ($350 \text{ mm}^3/\text{mm}$).

As the abrasive grit wears (with an increase in the specific material removal V_w'), a common occurrence is the grain protrusion decrease (abrasive wear, creating a platform on the grit) exposing the less protrude grits to the material. This increases the number of kinematic cutting edges and reduces the chip thickness h_{cu} , lowering the surface roughness.

The behavior presented in most conditions, especially for the MC00 and MC15 grinding wheels is not consistent with the expected behavior. With the increase in the specific material removal rate from 4 to $7 \text{ mm}^3/\text{mm}\cdot\text{s}$, the expected wear mechanism would be based on the breakage of the abrasive grits instead of grit flattening. This behavior was previously hinted in the grinding force components but confirmed with roughness analysis.

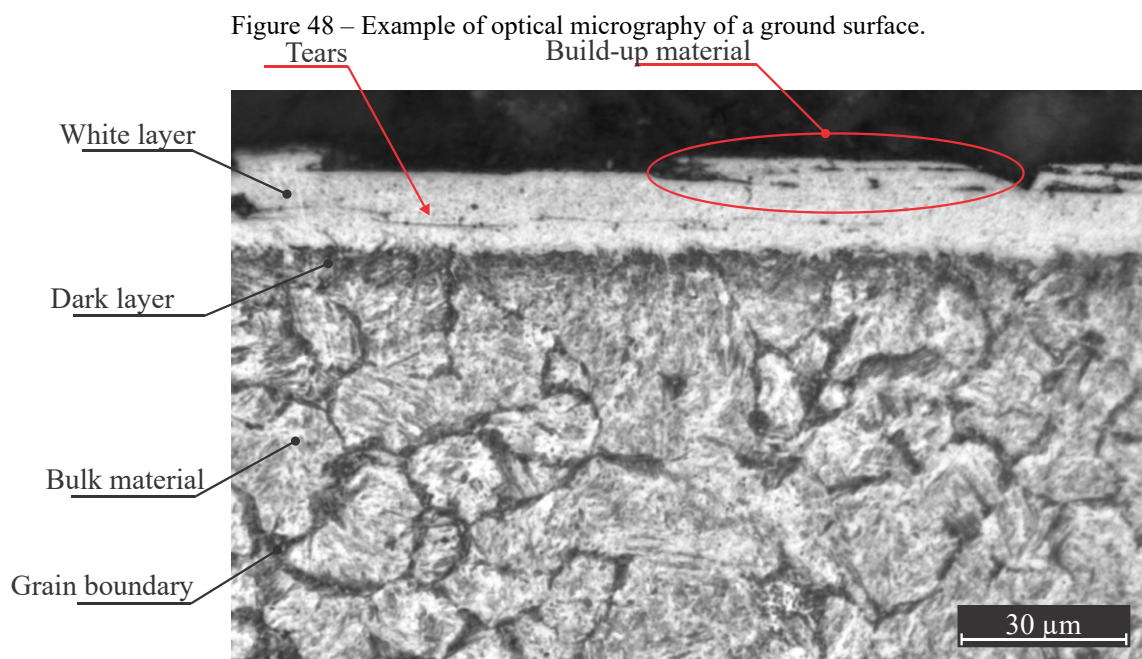
Mayer *et al.* [49] achieved the same conclusion in regard to the maintenance of a stable surface roughness level with an increase of sol-gel Al_2O_3 content. The authors established this behavior because of the stable sliding conditions on the flat surface of sol-gel grits, granted by the appearance of a tribological oxide layer. The authors also observed that for small Q_w' ($< 4 \text{ mm}^3/\text{mm}\cdot\text{s}$), the differences between grinding wheels are negligible.

However, Fathallah *et al.* [16] found conflicting results, illustrating that the presence of sol-gel Al_2O_3 led to an increase in the surface roughness, with an increase of the specific material removal. The type of wear found by the authors promotes the grit flattening (for the electro-fused Al_2O_3) in contrast to micro-chipping for the sol-gel Al_2O_3 , which explains the differences.

In agreement with the force results, the surface roughness profiles illustrated a consistent behavior if the individual grinding wheels were analyzed, however, the comparison with the presented literature shows disagreement.

4.2.3 Boundary-affected layer

Boundary-affected layer modifications, the consequence of the thermo-mechanical interaction during the grinding process, leads to various phenomena that alter materials properties. In this aspect, this section describes the influence of the input variables (cutting parameters, grinding wheels) on surface integrity. The alterations considered here were detected as white and dark layers and composed the boundary-affected layer (BAL) thickness, exemplified in Figure 48.

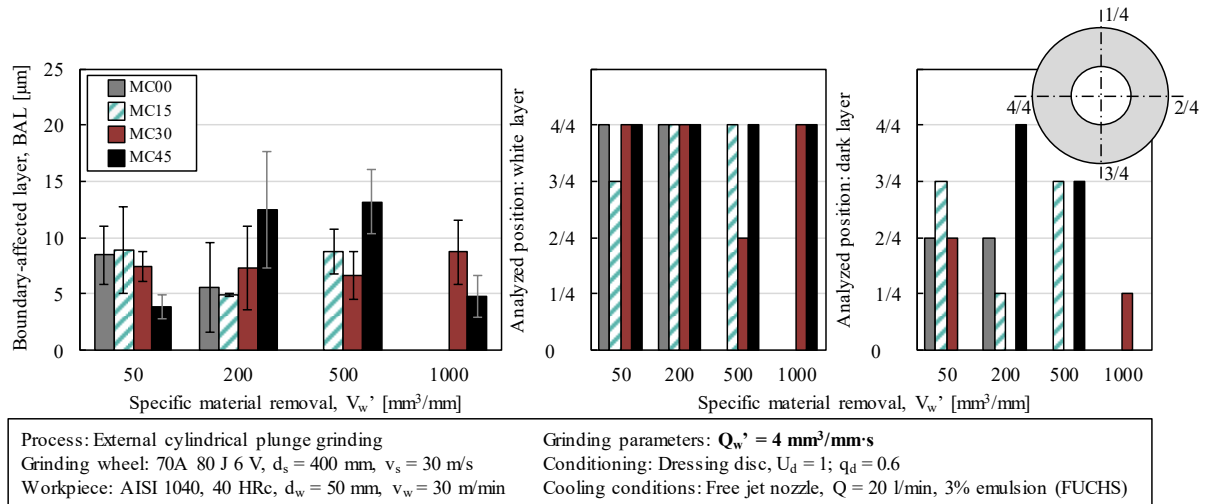


Source: Author.

A clear distinction between the bulk material (composed primarily by tempered martensite) with a white layer (no discernible microstructure). The dark layer acted as a transition zone. Indications of tears and build-up material were discernible along the ground subsurface. This type of modification was consistently observed throughout the ground subsurface and in many conditions.

The image analysis also highlighted the presence of these layers within the considered BAL thickness and workpiece periphery sections (1 to 4 position, out of 4 analyzed positions). The metallographic images of each condition can be observed in APPENDIX C for further reference.

Figure 49 illustrates the obtained thickness and the detected features for the initial specific material removal rate (Q_w' of $4 \text{ mm}^3/\text{mm}\cdot\text{s}$).

Figure 49 – Boundary-affected layer for a Q_w' of $4 \text{ mm}^3/\text{mm}\cdot\text{s}$.

Source: Author.

At first glance, the increase in specific material removal did not present a discernible trend with the calculated grinding force components. The large dispersion of results is accounted for the nature of the cylindrical plunge grinding overlap characteristic, as well as the spiral-shaped workpiece.

There is a slight difference between the grinding wheels' ground subsurface, which initially implies that the type of abrasive grit involved during the surface formation had a substantial effect on the boundary-affected layer. The MC00 and MC15 grinding wheels, in which the predominance of the monocrystalline aluminum oxide is greater, led to a BAL thickness of $10 \mu\text{m}$. This value decreased and then increased for the upcoming specific material removal intervals (V_w'). In these conditions, white and dark layers were detected, which suggests a combination of temperature and mechanical martensite transformation.

The MC30 grinding wheel showcased a uniform formation of the boundary-affected layer along the investigated ground volume. The cutting stability, evidenced by the grinding force and surface roughness results, led to uniform BAL thickness. The layers observed in this condition suggests an initial temperature gradient, that reduced along the machined volume.

However, for the MC45 grinding wheel, the behavior was predominantly different. The higher presence of MC abrasive grits led to a thick boundary-affected layer at the intermediate V_w' interval. The increase in the boundary-affected layer was associated with the presence of a dark layer, which indicates a high-temperature gradient.

The results obtained for both grinding wheels (MC30 and MC45) only differ for the surface roughness evaluations, since the grinding force components were statistically equal. It is common knowledge in the grinding process that the tangential force has a linear correlation

with the cutting power, which governs the heat generation. Therefore, similar force magnitudes imply similar heat generation and dissipation to the workpiece. In this context, a possible hypothesis relies on the fact that the microcrystalline Al_2O_3 abrasive grit has lower heat conductivity than the monocrystalline Al_2O_3 , which in turn increases the temperature on the cutting region.

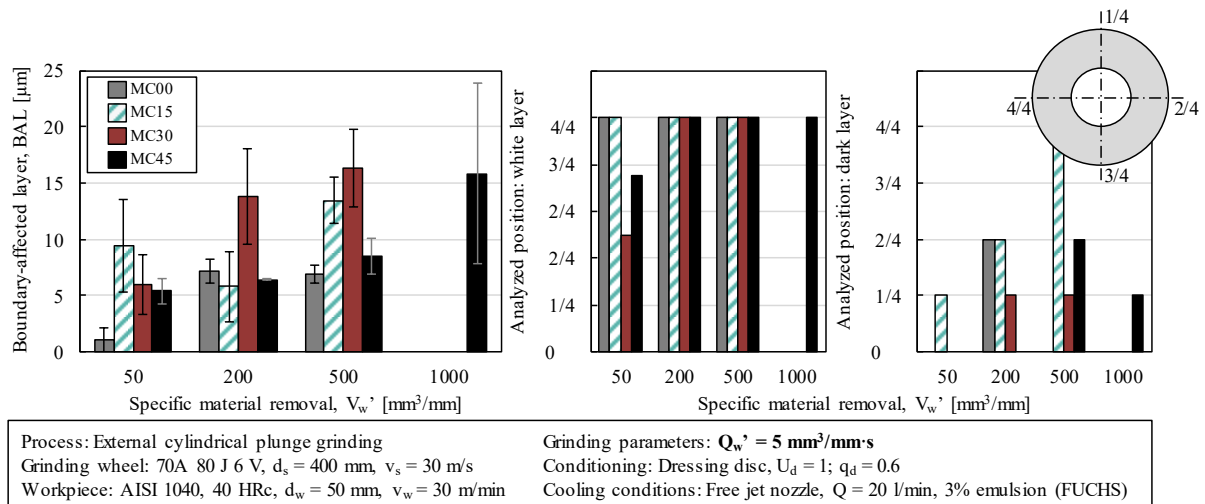
The heat conductivity hypothesis was previously stipulated by Klocke *et al.* [48] and Mayer *et al.* [49]. The authors postulated that the higher concentration of imperfections in sol-gel alumina reduces the mean optical path length of the phonons, resulting in lower heat conductivity. This effect helps to increase the temperature in the cutting zone, which also might lead to thicker heat-affected layers. This was later studied by Zhao *et al.* [124], whose study observed the highest temperatures for a 100% sol-gel grinding wheel in comparison with a 50% sol-gel/electro-fused and with a 100% extruded sol-gel grinding wheel. Experiments were conducted in the surface grinding of an Inconel 718 alloy.

In terms of observed microstructure alterations, the presence of the white layer was almost unanimous throughout all the conditions, whereas the presence of the dark layer was occasionally detected. Dark layer formation reflects the thermal aspect of the process, as it is mainly obtained as an overtempered martensite structure (OTM), which depends mostly on the temperature gradient. However, that is not the case for white layers, where the “white/blank” aspect of the layer is referenced as a fine microstructure, composed primarily of fine untempered martensite (UTM) and retained austenite (RA). This fine microstructure can be obtained through a temperature gradient or by extremely intense plastic deformations, which causes formations of twins on the structure. The deformed structure then recrystallizes into sub-micrometric grains [78].

If the volumetric phase fraction is taken into consideration, it is expected that the grinding wheels MC00 and MC15 present a quicker temperature decrease due to the higher thermal conductivity of the grinding wheel (lower pore and monocrystalline fraction, higher binder fraction) in comparison to the MC30 and MC45 grinding wheels. A higher volume of pores indicates a higher volume of air, which presents the lowest thermal conductivity of grinding materials (vitreous material, mono, and microcrystalline Al_2O_3). In other words, by associating the presence of a microstructure with the thermal gradient, lower thermal conduction would mean temperature maintenance and higher presence of dark layers. However, this is not the case for these parameters (Q_w' of $4 \text{ mm}^3/\text{mm}\cdot\text{s}$), where the highest presence of dark layers was found for the MC00 and MC15 combination.

By increasing the severity of the process, to a Q_w' of $5 \text{ mm}^3/\text{mm}\cdot\text{s}$, the following results can be observed (Figure 50).

Figure 50 – Boundary-affected layer for a Q_w' of $5 \text{ mm}^3/\text{mm}\cdot\text{s}$.



Source: Author.

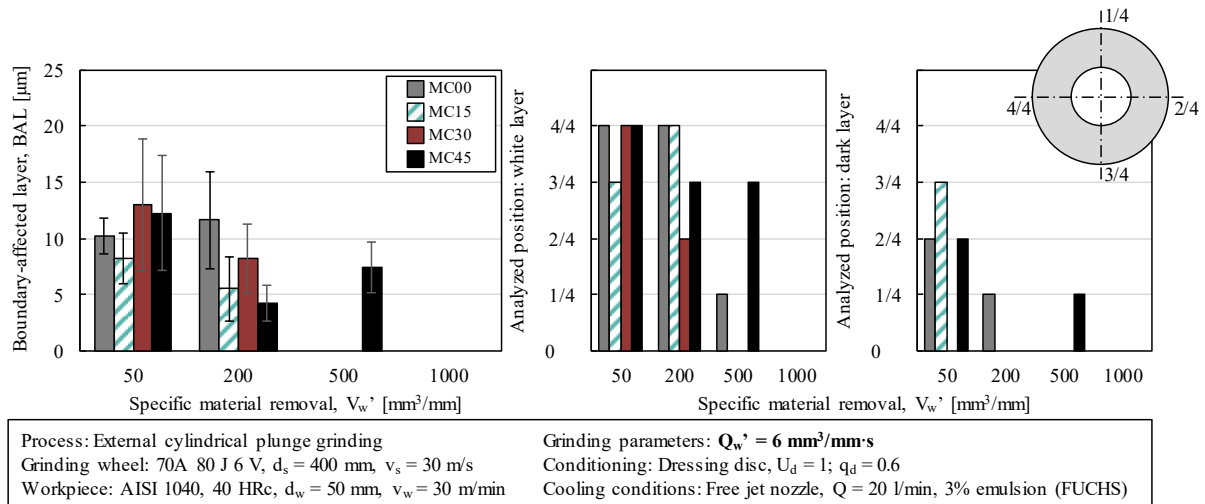
The ground subsurface obtained using an MC00 grinding wheel illustrated an increase on the boundary-affected layer with the increase of the ground volume V_w' . While the white layer was consistently detected as a resulting microstructure modification, dark layers only appeared in isolated locations. Oppositely, for the MC15 grinding wheel, an initial decrease and then an increase in the BAL thickness with each volumetric interval was measured. Since the characteristic layers are initially untempered martensite but become increasingly untempered and overtempered martensite, it is hypothesized that an increasingly intense abrasive wear took place, favoring friction.

In terms of grinding force components and surface roughness, MC00 and MC15 presented similar magnitudes, which implicates that the presence of microcrystalline aluminum oxide favored the temperature increase, as previously hypothesized.

A rapid BAL thickness increase was detected for the MC30 as the material removal increased, however, the presence of dark layers was sparsely detected along the analyzed workpiece periphery. The MC45 illustrated a slow increase in the boundary-affected layer thickness with the increase in the volume removed by the wheel. In both cases, it is suspected that the increase in the grinding forces (and cutting power for that matter) led to a thicker boundary affected layer. The difference between the two grinding wheels, however, is that the higher content of MC kept the grinding wheel initial dressing for a longer period. The detected layers indicate, for higher specific material removal V_w' , sharper thermal gradients.

Increasing the process severity with a higher Q_w' , it is expected the thickness of altered material to increase (Figure 51). However, there is a visible overall reduction of the affected layer depth for most conditions.

Figure 51 – Boundary-affected layer for a Q_w' of $6 \text{ mm}^3/\text{mm}\cdot\text{s}$.



Source: Author.

The MC00 displayed a slight tendency of boundary-affected layer thickness increase, results consistent with the grinding force components. Higher tangential force is equivalent to higher cutting power necessary to shear the material and thus, energy dissipated to the workpiece.

On the other hand, the remaining grinding wheels (MC15, MC30, and MC45) illustrated a clear tendency of a greater BAL thickness at the initial interval and reduced as the grinding wheel wore down. If the grinding force components were to reduce along the ground volume, this behavior would be consistent. However, the grinding force components increased with the material removal V_w' , which reduces the consistency of the results.

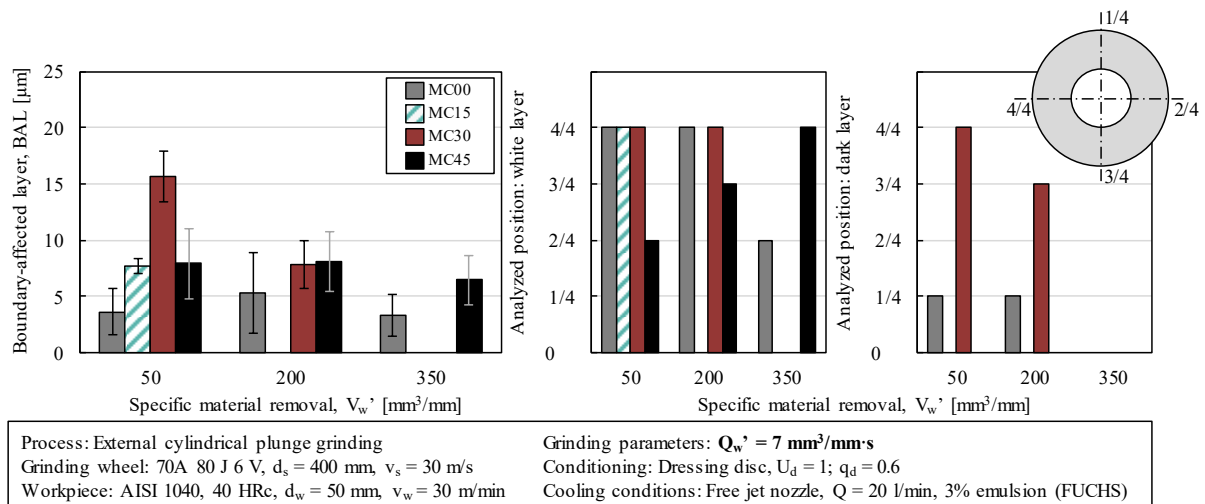
The layers detected for this specific material removal rate were mainly white layers. Dark layers were associated with the MC00 and MC15 grinding wheels, as well as the MC45 grinding wheel.

One possible explanation for this behavior is associated with the micro-wear of the MC abrasive grits by micro-splintering. Due to a large number of sintering interfaces, the MC grits wore down by micro-splintering rather than abrasion, which in turn leads to a larger real area of contact. Increasing the area of contact allows for more efficient heat conduction.

Evaluating the last Q_w' ($7 \text{ mm}^3/\text{mm}\cdot\text{s}$, Figure 52) it is possible to notice a similar behavior to the previous conditions.

The MC00 illustrated a consistently thin boundary-affected layer, however not on-par with the grinding force components. Due to the large forces, it was expected a large increase in the cutting power and consequent increase in the temperature in the cutting zone. If otherwise the grinding force component reduced, as expected for a large specific grinding rate Q_w' , the subsurface damage depth would be consistent with the presented results. The results for the MC15 wheel are similar to the MC00 grinding wheel.

Figure 52 – Boundary-affected layer for a Q_w' of $7 \text{ mm}^3/\text{mm}\cdot\text{s}$.



Source: Author.

In contrast with the previous grinding wheel, the MC30 illustrated a thicker boundary-affected layer modification. In this case, it is believed that the greater content of MC abrasives led to a more “stable” wear, creating a frequent micro-chipping of the abrasives and, with it, an increased number of micro-edges. Evidence of the dark layer suggests that a gradient of temperature was present and assisted the material modification.

For the MC45 grinding wheel, a parallel to the MC30 grinding wheel can be drawn. However, the presence of dark layers was not detected, which suggests that the increasing wear, frequent micro-chipping and higher content of microcrystalline abrasives led to a stable wear condition, reducing the load on the individual cutting edges and inducing white layer by the intense mechanical load, rather than purely phase transformation by temperature.

In a similar way that was presented on the latter specific material removal rate (Q_w'), white layer presence was the main source of alterations. In contrast, the presence of a dark layer was not detected for the MC45 grinding wheel, whereas MC30, the dark layer was extensively observed.

Given the dispersion of results, a similar magnitude of affected layer thickness can be associated with the specific material removals and grinding wheels. The great severity of this condition leads to a high energy generation and white layer accompanied by the dark layer (thermal influence) for the MC30. In the MC45 case, the presence of only white layer alerts to the fact that the increased content of sol-gel abrasive grit fractured with a higher frequency and, therefore, kept the cutting mechanism stable, but causing modifications to be under heavy plastic deformations due to the thin individuals formed chips.

Global observations illustrate a trend that increasing the specific material removal rate will reflect on a thicker boundary-affected layer. For a Q_w' of $4 \text{ mm}^3/\text{mm}\cdot\text{s}$, the average BAL thickness was in the order of $10 \text{ }\mu\text{m}$. This value increased to $15 \text{ }\mu\text{m}$ for a Q_w' of $5 \text{ mm}^3/\text{mm}\cdot\text{s}$, keeping a constant magnitude for the upcoming Q_w' of 6, and reduced to a thickness of $10 \text{ }\mu\text{m}$ for the $7 \text{ mm}^3/\text{mm}\cdot\text{s}$.

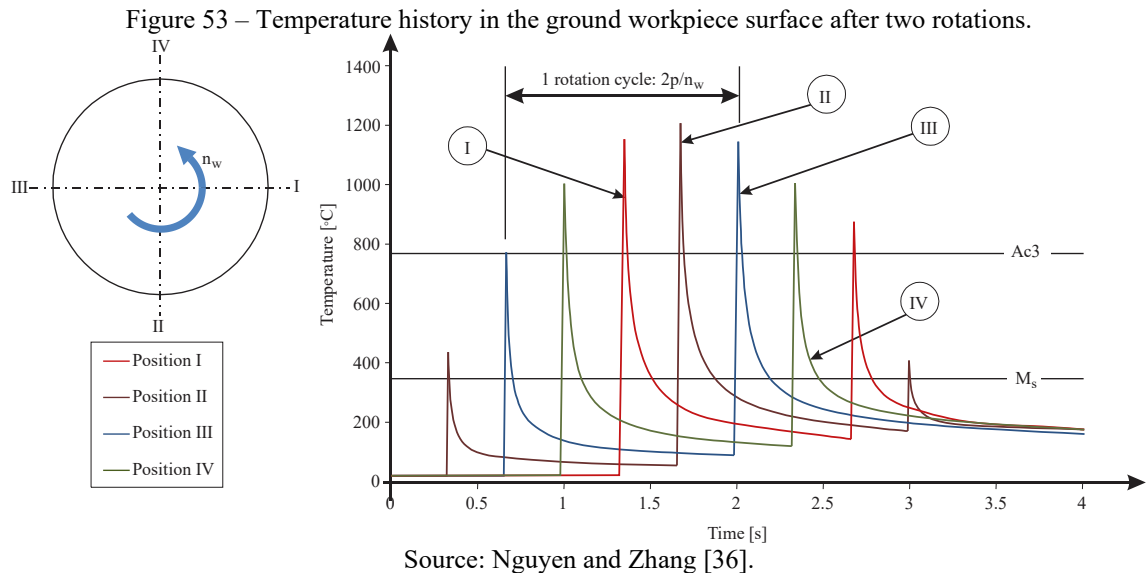
Klocke *et al.* [21] observed reliable results, for external cylindrical plunge grinding of AISI 52100 steel using conventional electro-fused Al_2O_3 . Although the modifications caused annealing of the material subsurface, the results displayed by the authors show an increase of the boundary-affected layer with an increase in specific material removal rate Q_w' . The unevenness of the boundary-affected layer thickness was also observed by the authors.

This uneven behavior of the BAL thickness is also influenced by the cylindrical plunge trajectory and cyclic temperature distribution. Cylindrical plunge grinding is a process that relies on multiple cycles of material removal, with each rotation of the workpiece overlapping the previous lap. This reflects on the subsurface microstructural modifications. Nguyen and Zhang [36] studied the effect of external cylindrical plunge grinding kinematics on the depth of the hardened layer. With each possible complete rotation of the workpiece, the temperature rises to a certain temperature peak, cools down and rises again on the next cycle. Since the new initial temperature of the workpiece is different from the ambient temperature, a lower thermal gradient is expected (Figure 53).

Hence, since the depth of the boundary-affected layer is consistently thicker than the depth of cut a_e , only a small portion of the boundary-affected layer thickness is removed each rotation, leading to a constant and cyclic layer alteration overlapping and causing a large dispersion on the results.

In terms of feature observations, assuming that the presence of the dark layer highlights the thermal aspect of phase transformation and that detection of only white layer highlights the mechanical influence on the phase transformation, it was noticed: MC00 and MC15 grinding wheels presented a more intense presence of dark layer, whereas MC45 presented a more

intense presence of only white layer. MC30 grinding wheel remained in between the other two microcrystalline Al_2O_3 contents, not favoring one or the other layer appearance. This might be indicative of superior wear resistance of sol-gel abrasive grits, which maintains a protrude cutting edge and favors material removal by cutting, rather than rubbing or plowing.



Considering a sum of all input conditions (Q_w' , V_w') the thickest boundary-affected layer is attributed to the grinding wheels with the highest microcrystalline aluminum oxide content. The average BAL thickness is $10\ \mu\text{m}$ for the MC30, $8\ \mu\text{m}$ for the MC45, $8\ \mu\text{m}$ for the MC15, and $6\ \mu\text{m}$ for the MC00.

An overall analysis of the results displays that: the subsurface boundary-affected layer thickness was consistent for each given grinding wheel, with exceptions where the cutting severity was above the measuring system/machine-tool capacities.

Predictions of the BAL thickness and microstructure, taking into consideration the grinding wheel's volumetric fraction, was not able to explain the observed behaviors for the different grinding wheels.

In conjunction with the specific grinding force components (F_n' and F_t'), surface roughness parameters (R_a , R_z , and R_{sk}) and boundary-affected layer thickness results, an ANOVA analysis was executed. However, only a first level interaction analysis was possible, due to the impossibility of breaking down the specific material removal V_w' variable (not all conditions reached the same ground volume). In those conditions, there is a clear distinguishable effect of the specific material removal rate Q_w' and the V_w' , however, the

grinding wheels microcrystalline content only display a clear trend for the surface roughness results. The adjacent results were deemed as statistically equivalent.

4.2.4 Summary of the stage I experiments

The initial analysis of the results, without consideration for the grinding wheel volumetric fraction, illustrated inconsistent results when comparing the grinding wheels variations. The results can be explained (Table 14), at least with regards to the grinding force components and surface roughness, by the volumetric phase fraction obtained by the X-ray tomography image analysis.

Table 14 – Summary of stage I results in regards to the volumetric phase fraction.

Evaluated phase	MC00 and MC15		MC30 and MC45	Influence on the results
Binder	21%	→	10%	↓ binding efficiency ↓ macro-wear resistance ↑ self-sharpening effect ↓ grinding force, ↑ surface roughness
Abrasives	50%	→	55%	↑ number of cutting edges (statics and kinematics) ↑ grinding force, ↓ surface roughness
Pores	29%	→	35%	↓ thermal conductivity

Source: Author.

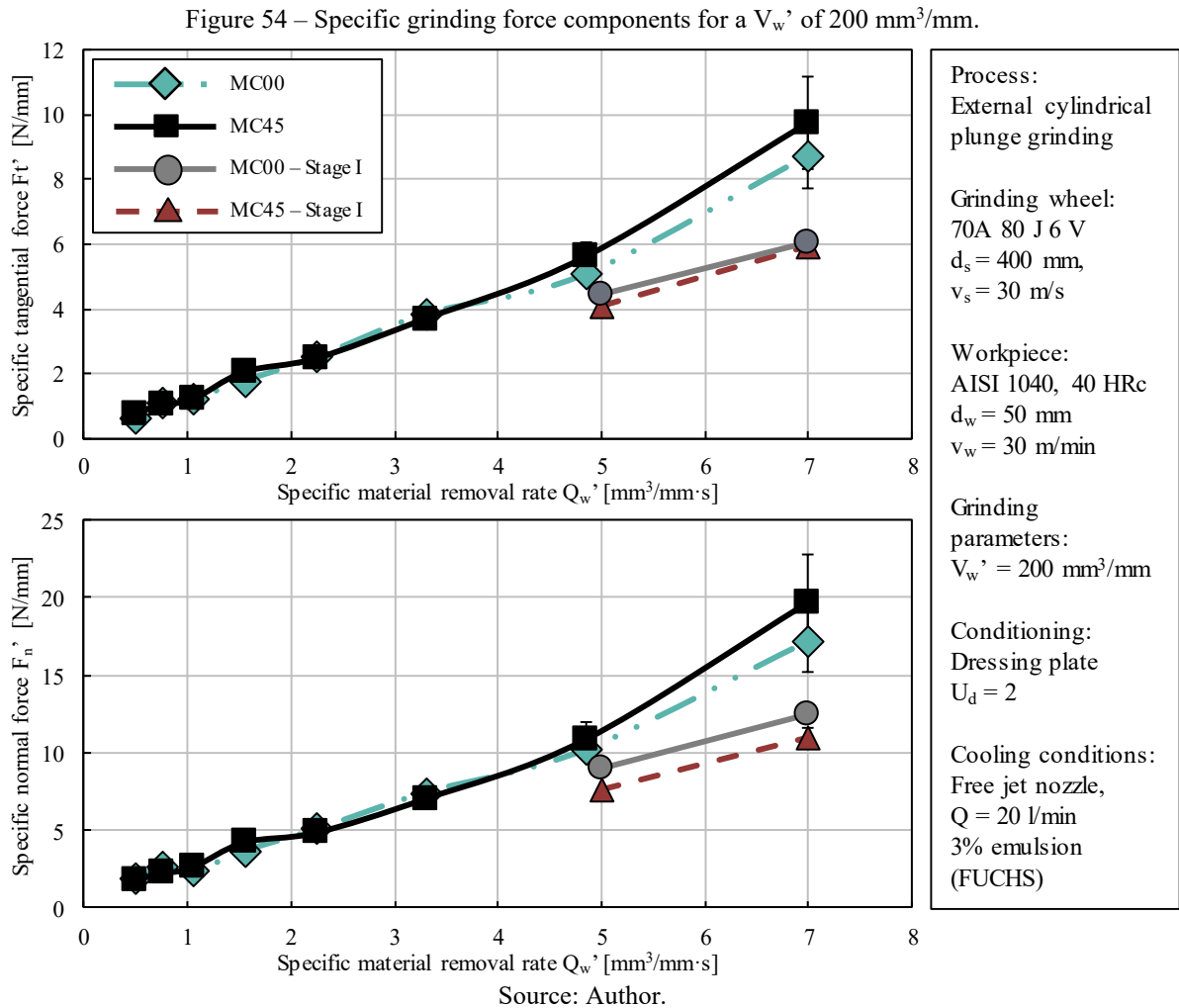
The overall analysis of the boundary-affected layer, either the detected and classified feature or the thickness, is still not entirely explained. A few hypotheses were drawn, but the wider range of factors that influences the formation of the boundary-affected layers rendered any explanations inaccurate.

4.3 STAGE II – MULTIPLE-STEP PLUNGE CYCLE

This section follows the optimization methodology for the grinding cycle, considering as input the results obtained for several specific material removal rates Q_w , from roughing to finishing stages. The first three subsections encompass the database creation with results from the: grinding force components, surface roughness, and boundary-affected layer measurements; culminating in the last section, where the resulting multi-step external circumferential plunge grinding cycle optimization will be illustrated.

4.3.1 Grinding force components, F_n' and F_t'

Figure 54 illustrates the results for the specific grinding force components as the specific grinding rate increases.



There is a clear increase in specific grinding force components with an increase in Q_w' . Although the standard deviation is large, it is possible to observe that the average grinding force comparing the grinding wheel presents similar magnitudes for an initial condition ($0.5 - 4.85 \text{ mm}^3/\text{mm}\cdot\text{s}$) but starts to differ when increasing the specific material removal rates.

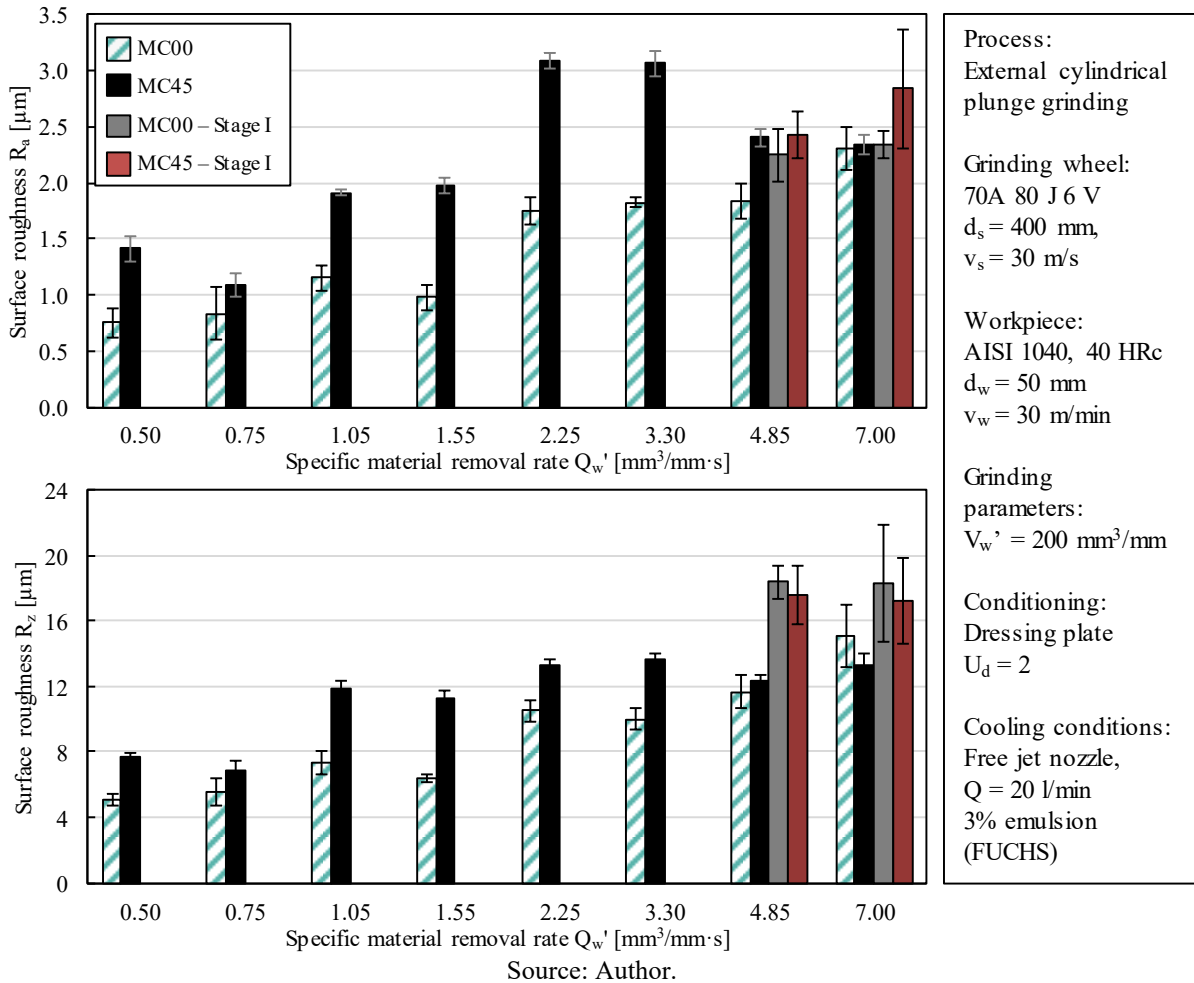
Figure 54 also showcases the grinding force for stage I experiment, MC00 and MC45 grinding wheels. Since the dressing overlap ratio was more aggressive ($U_d = 1$ for the previous experiments), it is expected that the grinding forces increase when a higher overlap ratio is employed (higher number of kinematic abrasive grits and cutting edges, and lower chip thickness).

Contrary to the previous experiments, showcased in stage I, the highest grinding force components were registered for the MC45 grinding wheel. The critical normal force, necessary for grit microfracture [19], for the microcrystalline aluminum oxide abrasive grit was not reached, which lead to a constant abrasive wear mechanism, grit dulling and higher forces. On the other hand, even though the MC00 had a higher binder content, the critical normal force was reached, which reduced slightly the grinding force components.

4.3.2 Surface roughness

Increasing the specific material removal rate (and the depth of cut a_e for that matter), it is expected an increase in the surface roughness values, confirmed by the results illustrated in Figure 55.

Figure 55 – Surface roughness height parameters for a V'_w of 200 mm³/mm.



For a fixed specific material removal, increasing the Q_w' represents increasing the depth of cut and, therefore, increases the uncut chip thickness. Also, higher Q_w' results in a higher radial wear rate due to the different wear mechanisms, which in turn may be reflected in the surface roughness.

The grinding wheel with 0% of microcrystalline abrasive grits showcased different surface roughness ranges of values. For a Q_w' from 0.5 to 1.55 mm³/mm·s, the roughness values remained on a similar range of values. Increasing the specific material removal, the range of 2.25 to 4.85 mm³/mm·s, the roughness values increased to a new magnitude. A specific material removal rate of 7 mm³/mm·s led to the highest measured values. Similarities of roughness values inside the discussed ranges are expected since the variations on the Q_w' and uncut chip thickness (h_{cu}) are small and negligible on this condition. The same can be related to the other ranges.

Similar behavior can be observed for the surfaces ground with an MC45 grinding wheel. The first range of values covers the 0.5 and 0.75 mm³/mm·s of Q_w' , increasing to a peak at the range between 2.25 and 3.3 mm³/mm·s, which decreases at the final Q_w' of 4.85 and 7 mm³/mm·s. While the different ranges of values are consistent throughout the experiments, the behavior of reaching the highest values at the 2.25 and 3.3 mm³/mm·s specific material removal is atypical. One can expect that, at the last two Q_w' , the abrasion wear mechanism was still intense, creating a duller grinding wheel, an increased number of kinematic cutting edges and reducing the surface roughness. Values for the grinding force components (section 4.3.1) indicates a higher mechanical load for this condition, which is consistent with the presented surface roughness behavior.

Differences between the two grinding wheels' content are expected to be related to wear resistance. Since the sol-gel grinding wheel presents a higher wear resistance, the initial wheel profile is kept for a longer period before the occurrence of grit flattening or the self-sharpening effect.

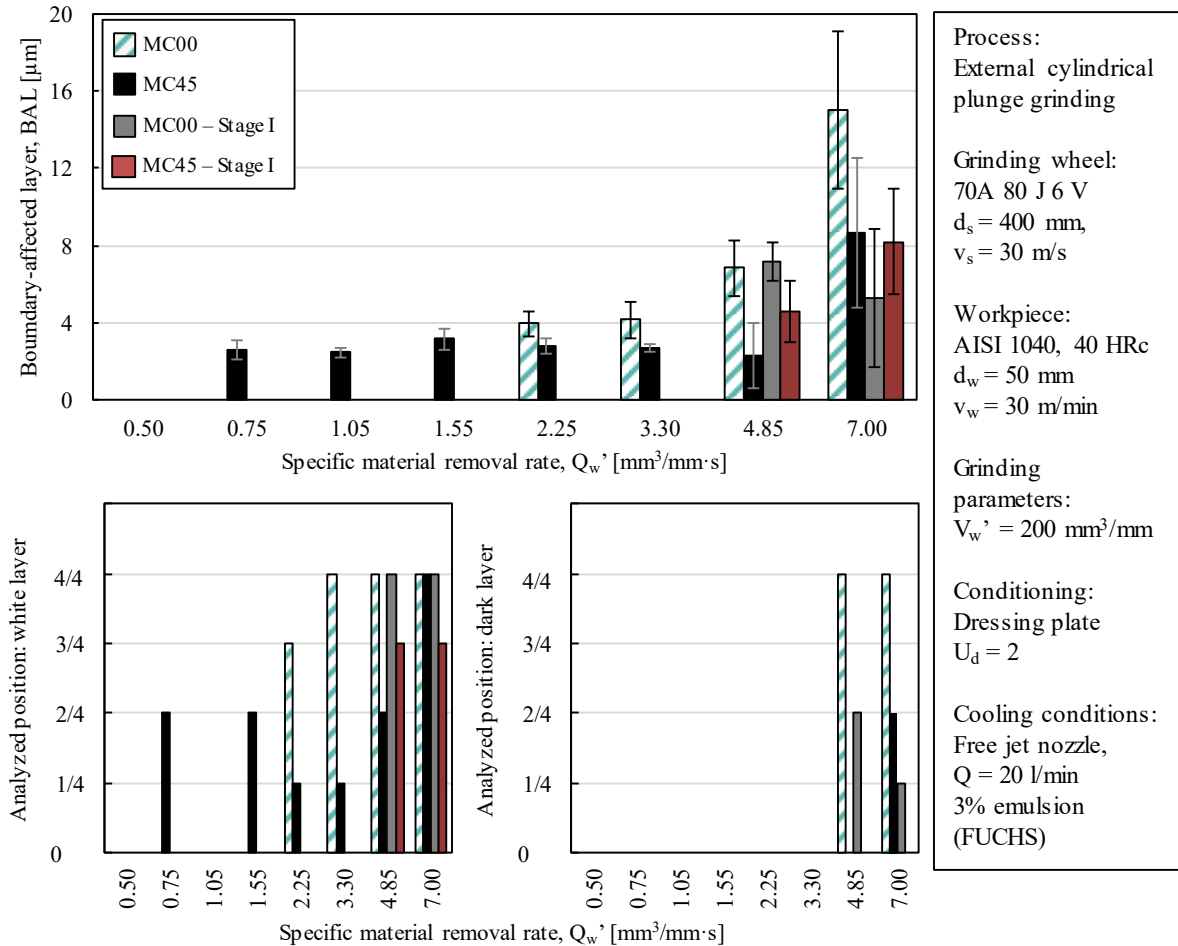
The clear effect of the aggressive dressing ratio is illustrated when comparing with the results from the experimental stage I.

4.3.3 Boundary-affected layer

When surface quality/product life is of interest, it is usual practice to reduce the radial feed rate, and for that matter the specific material removal rate of the process, in order to avoid alterations on the workpiece. Hence, to evaluate the tested conditions, Figure 56 illustrates the

boundary-affected layer thickness with increasing Q_w' . And for further reference, APPENDIX C contains the metallographic images of the steel microstructure for the tested conditions.

Figure 56 – Boundary-affected layer with a fixed V_w' of 200 mm³/mm.



Source: Author.

Two distinct behaviors were observed, associated with the microcrystalline content. On one hand, the boundary-affected layer for the grinding wheel with no content of microcrystalline grits (MC00) followed the specific force behavior, increasing the BAL thickness with the increase of Q_w' . On the other hand, the grinding wheel with 45% microcrystalline abrasive grit content presented a lower but constant BAL thickness, up until the last condition, where a thicker altered material layer was observed. It would be expected that the condition that illustrated the highest grinding force would present the thickest BAL. However, the MC00 illustrated the lowest grinding forces but the thickest boundary-affected layer.

As per features observation, it was most detected a consistent presence of white layer, with an indication of a dark layer only on the higher Q_w' (4.85 and 7 mm³/mm·s). The current

results are consistent with the hypothesis that the white layer is not only generated by phase transformation induced by quenching, but also by extensive plastically deformed zone. In the case of the heat-induced white layer, it would be expected detection of dark layers due to a temperature gradient.

The consistent presence of BAL for the MC45 condition alerts to the fact that there is higher discordance dislocation, moreover, associated with the maintenance of initial grinding wheel profile and thus inducing a consistent material deformation and shearing.

Since the MC00 grinding wheel is more prone to changes in the grinding wheel profile, material shearing is less likely to occur at smaller depths of cut. With the increase in the depth of cut, wear by microchipping is more frequent, which will prompt the shearing to increase and therefore, plastic deformation.

The overall boundary-affected layer thickness was higher for the stage II experiments, a direct correlation with the higher forces and consequent higher temperature on the cutting zone.

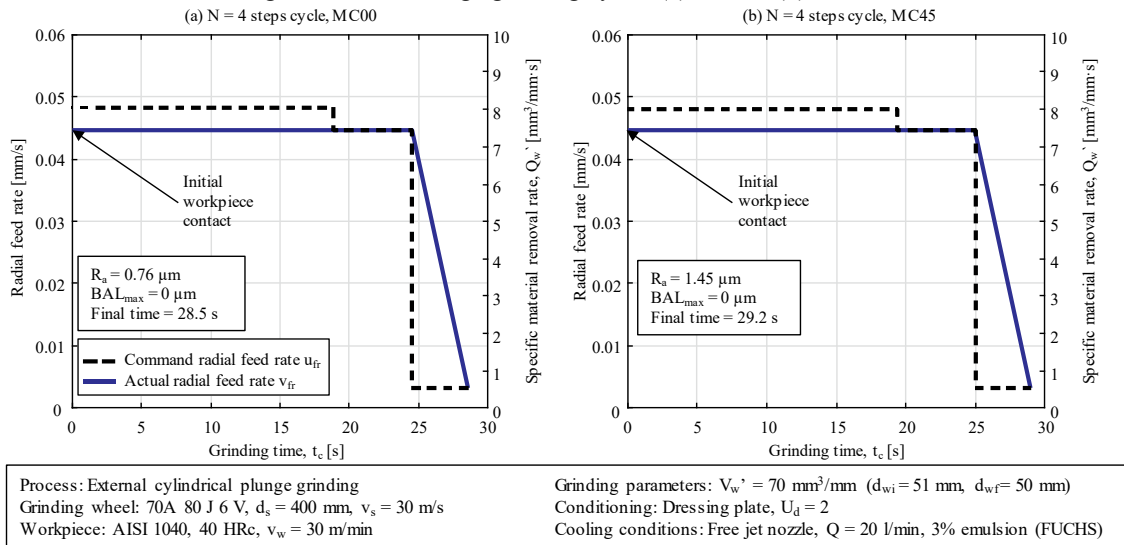
4.3.4 Optimization cycle

Using the previous results to supply a database, multi-step external cylindrical plunge grinding cycles were elaborated, using as entry input the grinding wheel and as constraints: maximum allowed surface roughness R_a , maximum boundary-affected layer BAL_{max} , minimum workpiece rotation of 1, and non-negative radial feed rates. The goal of the algorithm was to obtain the minimum grinding cycle time that respected the constraints, by iterating the number of steps “N” and finding the optimal time for the conditions. The boundary-affected layer thickness considered for cycle calculation was a value 50% higher as a safety margin.

Results were divided into two scenarios: two-stage (roughing and finishing) grinding cycle, mimicking an industrial application (Figure 57); and an optimized multi-step grinding cycle, using several discrete feed rates. Results were presented in terms of radial feed rate, in mm/s, calculated from the specific material removal rate using an average diameter. Further information about the discrete values that created the charts can be observed in APPENDIX D.

Overall, the grinding cycle presents a similar trend for both grinding wheels. A larger difference between the commanded feed rates to achieve a certain actual feed rate is due to the higher time constant for the MC45 grinding wheel (since it was observed a higher specific normal force F_n').

Figure 57 – Two-stage grinding cycle: (a) MC00, (b) MC45.



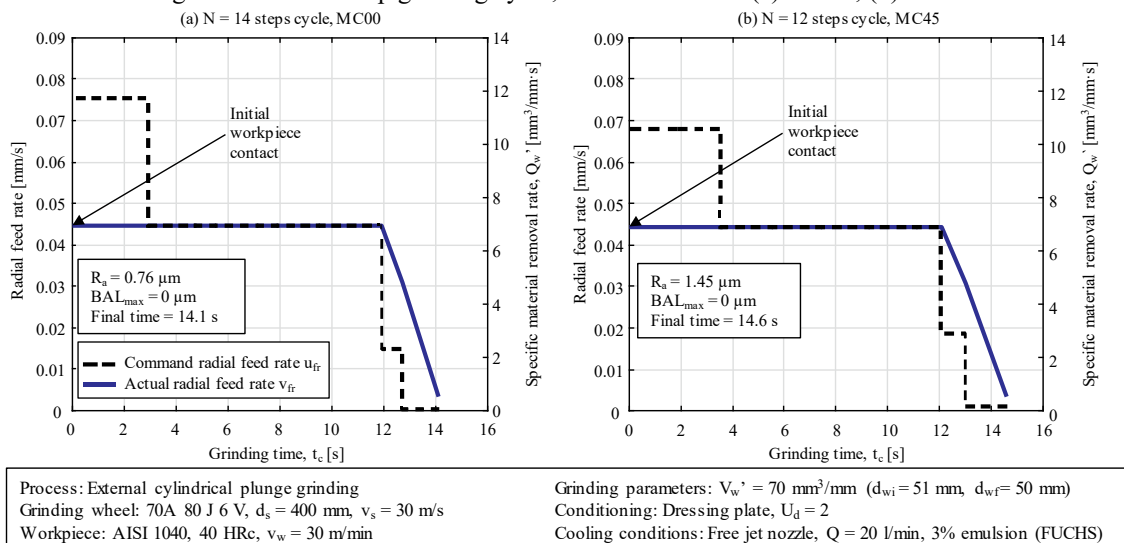
Source: Author.

However, the lowest surface roughness was achieved for the MC00 condition. If a similar surface roughness was considered for both cycles, it is expected a similar time for the MC00 grinding wheel. However, if a smaller surface roughness was selected for MC45, the maximum boundary-affected layer restriction would not be satisfied (smallest R_a of $1.09 \mu\text{m}$ is for $Q_w' = 0.75 \text{ mm}^3/\text{mm}\cdot\text{s}$, $BAL = 4.5 \mu\text{m}$, the final time of 23.1 s).

In the same manner, with no restriction regarding surface roughness, the grinding cycle time for the MC00 would be 17.1 s, with a R_a of $0.98 \mu\text{m}$, BAL of $0 \mu\text{m}$.

In contrast with the extrapolated industry two-stage results, Figure 58 illustrates the results for the multi-step grinding cycle, using N discrete feed rate intervals.

Figure 58 – Multi-step grinding cycle, with N intervals: (a) MC00, (b) MC45.



Source: Author.

It is noticeable the difference in the application of the multi-step grinding cycle algorithm. The overall grinding time is cut down by half, also exhibiting a smoother transition between one stage to the other (Figure 58a and b, between 12 and 14 seconds).

Differences for the two grinding wheels rely on the fact that the MC45 grinding wheel presented higher resistance to wear and, in this case, led to higher normal forces. Higher normal forces lead to higher τ_F values. If a no restriction condition was selected, the obtained grinding cycles would slightly differ, as depicted in Table 15.

Table 15 – Grinding cycle times, considering one restriction.

	No R_a restriction $BAL_{max} = 0 \mu m$			No BAL restriction, $R_a = 1.1 \mu m$		
	N	Final time [s]	R_a [μm]	N	Final time [s]	BAL_{max} [μm]
MC00	18	12.7	0.98	18	12.7	0
MC45	19	14.7	1.41	13	13.9	5

Source: Author.

It is evident in this case that the MC00 grinding wheel presented a better option, as it reaches a lower grinding cycle time in any comparison. Since the MC45 presented either a surface with higher surface roughness R_a or a subsurface with constant presence of boundary-affected layer (as observed in the previous sections, 4.3.2 and 4.3.3), it is apparent to say that the MC45 was not suited for a grinding cycle with roughing to finishing cycles in terms of grinding cycle time.

Even if the optimization results are promising, real grinding experiments should be performed in order to attest to the efficiency of the model.

The overall values for the simulated multi-step grinding cycle illustrated interesting results, as well as a positive approach. However, due to the lack of consistency in the grinding wheel composition for both wheels, the data obtained in the analysis is not comparable.

4.4 ENVIRONMENTAL KEY PERFORMANCE INDICATORS AS A DECISION- MAKING METHOD FOR GRINDING PROCESS EVALUATION

Life cycle inventory analysis based on key performance indicators is an easily accessible methodology to evaluate the grinding process. This type of analysis can rely on literature and experimental data. If the data from the literature is reliable, the uncertainty of the results is low. In the case of this doctoral dissertation, the premise starts from the fact that the grinding wheel volumetric concentration, as illustrated by label specification provided by the

manufacturer, is equal for all the grinding wheels. However, as indicated by the high-resolution X-ray tomography image analysis, this is not the case. Even more so, this study uses the experimental data obtained from experiments and grinding wheel characterization to extrapolate the processing of a steel component via grinding. The calculated indicators are used to make decisions of the grinding wheels best suited for different scenarios.

The selected key performance indicators were normalized (Normalization Factor - NF) considering 1000 ground components, using information from the stage II experiments. It was selected two grinding application scenarios: scenario A, which consists of only a single roughing cycle of the component, however leaving an excess material of the same magnitude of the boundary-affected layer; and scenario B, which considers a multi-step grinding cycle of roughing to finishing stages. In order to calculate the selected indicators, a few input variables were obtained from the extrapolated grinding cycles (for each scenario). The input parameters can be observed in Table 16.

Table 16 – Input variables for Key Performance Indicator calculation.

	A (Without finishing step)		B (With finishing step)	
	MC00	MC45	MC00	MC45
Grinding time t_{grinding} [s/part]	12.0	11.7	14.1	14.6
Surface roughness R_a [μm]	2.31	2.34	0.78	1.45
Boundary-affected layer BAL [μm]	28	21	0	0
Grinding energy E_c [kJ]	27.6	29.8	27.0	29.0
Average Q_w' [$\text{mm}^3/\text{mm}\cdot\text{s}$]	7.11	7.11	6.5	6.4
Grinding wheel life [# of parts]	2.5	4.4	3.2	9.5

Source: Author.

By using these input parameters, and the calculation methodology described in section (3.6) the electrical energy intensity, non-renewable materials intensity, production rate, labor costs, investment, and product life were calculated. The results can be observed in Table 17.

Table 17 – Key performance indicators calculated for the simulated conditions.

Key Performance Indicator	Unit	Scenario A		Scenario B	
		MC00	MC45	MC00	MC45
Electrical energy intensity	kW/NF	129.3	123.9	136.5	133.0
Non-renewable materials intensity	kg/NF	5.9	5.9	5.8	5.9
Production rate	$\text{mm}^3/\text{mm}\cdot\text{s}$	7.1	7.1	6.5	6.4
Labor cost	R\$/NF	299.0	287.7	312.9	305.5
Investment	Norm. R\$/NF	1.0	1.7	1.0	1.7
Product life N_f	10^6 cycles	0.12	0.20	0.80	0.70

Source: Author.

Using the data from the table, each calculated KPI value was ranked from 1 to 10 (optimum value), establishing the degree of fulfillment (DF) value. The optimum value was a value 5% higher or lower than the maximum or minimum value of the two compared conditions since it is not expected that the calculated indicators to turn out optimal (with only two comparative items). Table 18 displays an example of the selected optimum value, as well as brief considerations for the optimum value selection.

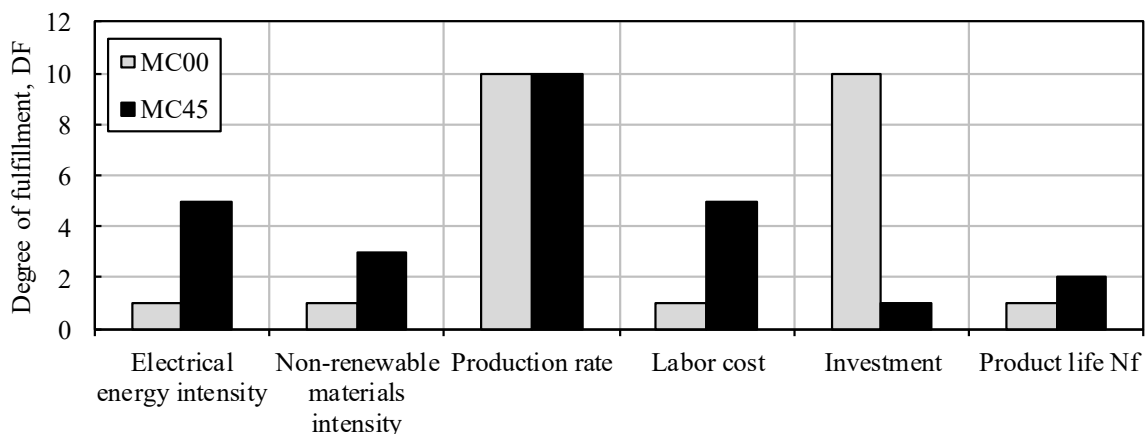
Table 18 – Example of the optimum value selection.

Key Performance Indicator	Optimum value DF =10	Tendency	Considerations
Electrical energy intensity	117.6	Decrease	5% lower value than the lowest energy consumed.
Non-renewable materials intensity	5.7	Decrease	Material discard as a chip from the component.
Production rate	7.0	Increase	Highest Q_w achieved.
Labor cost	273.3	Decrease	5% lower value than the lowest cost.
Investment	1.0	Decrease	Base value of a 100% monocrystalline Al_2O_3 grinding wheel
Product life N_f	1.0	Increase	No reduction in fatigue life.

Source: Author.

Using Table 18 considerations, Figure 59 illustrates the resulting degree of fulfillment for each indicator, scenario A.

Figure 59 – Degree of fulfillment ranking considering scenario A.



Source: Author.

For most indicators, there is a visible distinction for both grinding wheels. For the electrical energy intensity indicator, the highest score was verified for the MC45, a reflection of a higher interval between dressing operations.

The lowest values for the non-renewable material intensity, verified for the MC45 grinding wheel, were influenced by the high specific grinding rate, allowing a longer life span of the wheel.

The production rate was the highest for both conditions since the grinding wheels were able to reach the highest Q_w . This evaluation does not consider if the grinding wheel wear rate.

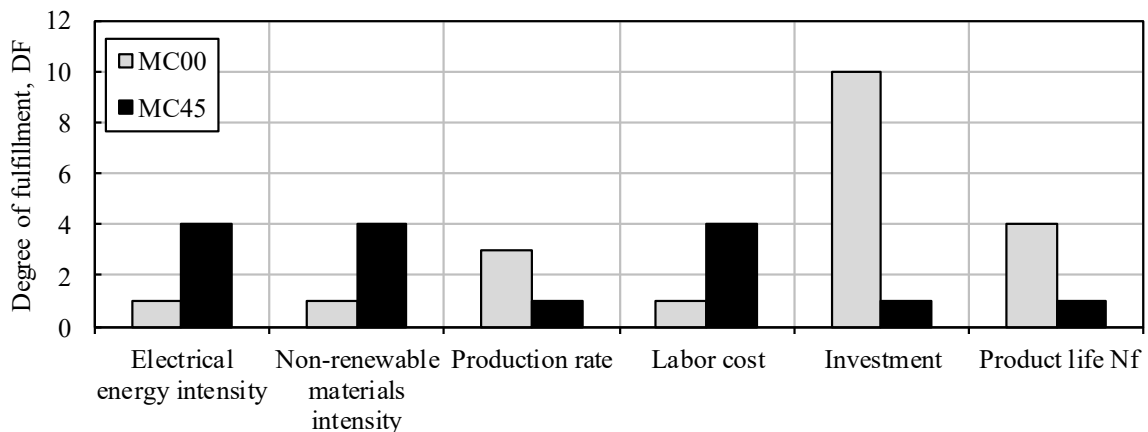
The labor cost is highly influenced by the grinding time. Since the time necessary to produce one component unit was lower for the MC45, this was the obvious choice.

The investment is where the pure monocrystalline aluminum oxide distances itself from the MC45. Since the price of MC45 is around 2.5 higher than the MC00, the relative grinding wheel cost is much lower for the MC00.

The product life for both grinding wheels was very low and of similar magnitudes. The MC00 illustrated the lowest surface roughness parameter, as well as the lowest boundary-affected layer thickness.

The degree of fulfillment analysis of the grinding scenario B, considering both roughing to finishing multi-cycle stages, can be observed in Figure 60.

Figure 60 – Degree of fulfillment ranking considering Scenario B.



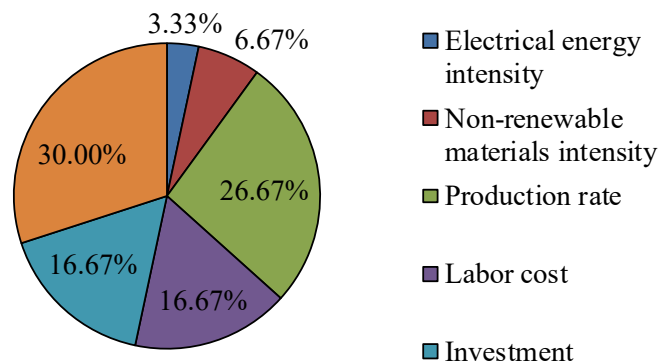
Source: Author.

The electrical energy intensity, non-renewable materials intensity, labor cost, and investment displayed similar values as the previous condition. However, the production rate exhibited a much lower degree of fulfillment, since to reach the desired surface roughness and BAL thickness, the grinding cycle strategy algorithm selected much lower specific material removal rates at the end of the cycle (finishing lap). The product life, here influenced only by the surface roughness (the BAL thickness is equal to zero), was favorable to the MC00 grinding wheel.

In an overall evaluation of the degree of fulfillment values, the MC45 displayed a better option for scenario A and the MC00 displayed a better option for scenario B.

However, using the degree of fulfillment alone is one way of comparing the best option for each scenario, yet, a more accurate approach calculates the weight of each indicator, instead of assuming that all of those indicators weigh equally on the decision. Using the pairwise comparison method, the indicators were weighted down, using as input information an informal survey with academics from the manufacturing area. The scores can be observed in Figure 61.

Figure 61 – Weight factor distribution using the pairwise comparison method.



Source: Author.

The informal survey resulted in an economical focused weight factor. Other approaches could consider the social or even the environmental metrics of sustainability analysis.

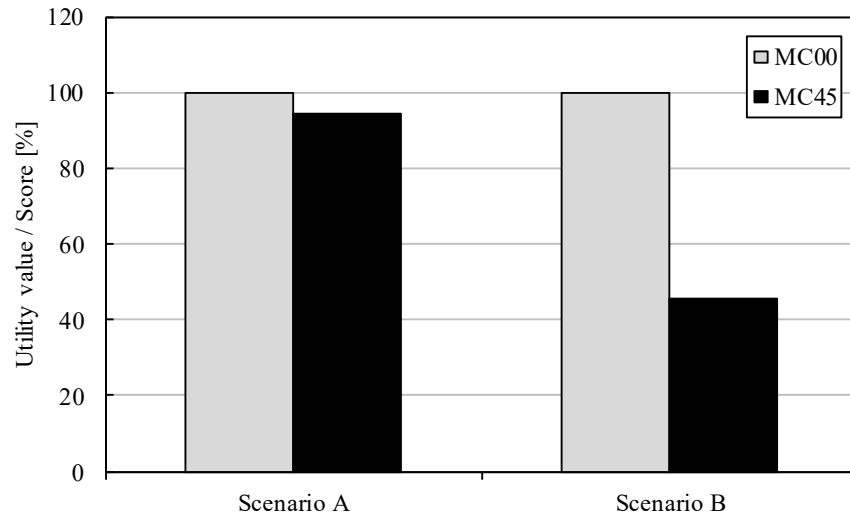
In the last step of the decision-making process, the weight factor weights down each indicator, resulting in the Utility Value (U), which will score the available options and point out the best one for each scenario (Figure 62). The grinding tool that reaches 100% is considered the best option for that scenario.

Considering a scenario without finishing stages (A), the most adequate option is the employment of MC00 grinding wheels. At the same time, when considering only one grinding wheel for a whole process (scenario B), the grinding wheel with no content of microcrystalline grits is still the most suitable option. However, the MC45 grinding wheel is still a suitable option for Scenario A if the investment is not a key factor for the application.

The indicator that had the greatest impact on the decision was the investment (for the A scenario) and the product life/investment (for the B scenario). In the case of the investment, the degree of fulfillment was biased by the binary selection, as the optimum value was selected

as the highest value of the two. Equalizing this indicator shows a close match between the grinding wheels, even though both conditions present different strong fulfillments.

Figure 62 – Relative Utility Value scoring.



Source: Author.

In the case of the product life, both conditions presented an equal extrapolated fatigue life in terms of boundary-affected layer, however, the higher roughness peaks for the MC45 slightly reduced the score for this indicator, favoring the MC00 grinding wheel for a roughing to finishing application.

This decision-making procedure only reinforced the already consistent application of the conventional grinding wheels. This analysis was carried out using experimental data as input and even if the previous results did not present an expected behavior, the employed results are enough for a life cycle inventory calculation focused on the grinding process. However, if only literature information was used as a system input, the lack of knowledge of the real grinding wheel volumetric phase fraction would misdirect the analysis and present results with larger uncertainties.

Grinding wheel specification is indicative of the grinding wheel resistance to micro and macro-wear (hardness), porosity and abrasive size. The slight variation of those properties may affect the grinding wheel wear, efficiency, surface roughness, thermal conductivity, boundary-affected layer; important data for a reliable process sustainability assessment.

5 CONCLUSIONS

In the use of conventional grinding wheels with an increasing volumetric fraction of microcrystalline aluminum oxide as abrasives, the grinding wheel manufacturer's label and normative information is not enough description to completely classify the tools as equals.

A novel methodology for characterization of the grinding wheels' morphology and phase fraction (abrasives V_g , binder V_b and pores V_p) was elaborated. It was found that the phase fraction of the MC00 and MC15 grinding wheels greatly differ from the MC30 and MC45 grinding wheels. The binder content for the MC00/MC15 is twice the magnitude of the MC30/MC45, whereas the abrasive grits content is 10% lower. The pore's volumetric fraction shifted accordingly (increasing from the MC00/MC15 to the MC30/MC45). The X-ray tomography image analysis highlighted that the label specification (and the normative for that matter) lacks complete information. The grinding wheels' volumetric content was not the same, which further affected the grinding experiments.

The presence of microcrystalline abrasive grits resulted in an improvement in the grinding wheel's life, effect resultant of the wear characteristics. In terms of specific grinding force components (F_t' and F_n'), there is an evident distinction between the experimented grinding wheels, due to the differences in volumetric phase fraction. This distinction was also evidenced by the surface roughness parameters.

With the increase in the specific material removal rate Q_w' , the grinding force components increased, as well as the surface roughness. With the increase in the specific material removal V_w' , the initial grinding force components displayed a slight increase, before exhibiting an intense chatter/vibration and noises, which leads to a spike on the force. The increase in the grinding force was accompanied by a reduction of the surface roughness. In conditions where the chatter behavior was present and the surface roughness was measured, the magnitude of the values also spiked.

Using the grinding force components and surface roughness results, it was possible to refer the main wear mechanism of the grinding wheels as abrasion, leading to a flattening/dulling of the abrasive grits. This was found to be inconsistent with the initial assumption, as well as the surveyed literature. The results reflected the grinding wheel differences characterized by means of X-ray tomography. This variation on the grinding wheel content led to an effect: a premature end of life due to the lack of self-sharpening effect.

The boundary-affected layer thickness results display mixed effects from the multiple input variables. A macro analysis indicates that the presence of microcrystalline aluminum

oxide on the composition had a significant effect on the magnitude of the BAL thickness. The results for each grinding wheel in most cases are consistent. However, the individual effects of each input variable (Q_w' , V_w' and grinding wheel content) did not present an expected linear correlation.

A multi-step optimization cycle for external cylindrical circumferential plunge grinding based on boundary-affected layer modifications thickness was elaborated, using as entry input grinding wheels with increasing content of microcrystalline aluminum oxide abrasive grits and the specific material removal rate.

Stage II, where the optimization cycle was implemented, also carrying out its own experiments with a wider selection of specific materials removal rate, but considering a fixed volumetric material removal, presented positive results in terms of reducing cycle time.

In terms of measured input data, the results (F_t' , F_n' , R_a , R_z , and BAL) presented for a fixed V_w' and increasing Q_w' a discernible trend.

The elaborated algorithm shows an improvement when compared with an extrapolated industrial condition. Differences between the two experimented grinding wheels were minor in terms of grinding cycle. However, the MC00 displayed a lower surface roughness at the end of the cycle. Although the developed algorithm displayed promising results, it is evident that a more consistent database is required to increase the confidence in the models.

Using the key performance indicators as a decision-making tool illustrated that the grinding wheel with no microcrystalline aluminum oxide content is better suited for an all-round condition. Cycles with no finishing stage are equally advantageous for both grinding wheels.

At the actual stage, the database of the grinding results obtained with aluminum oxide grinding wheels shows that the results achieved individually with each of the different evaluated grinding wheels permit an input in the discretized multi-step grinding cycle program. Based on the obtained results, if the goal is to predict the behavior of a selection of grinding wheels, reliable information of the grinding wheel structure is required. The information obtained from the normative is not nearly reliable enough, however, data from X-ray microtomography analysis, as well as other physical quantities, such as stiffness and mechanical resistance would allow a better prediction of the machining conditions.

6 SUGGESTION FOR FUTURE STUDIES

Expand the analysis of the grinding wheels by X-ray tomography for a more comprehensive variety of grinding wheels:

- a) Evaluate all the 18 grinding wheels manufactured in the scope of the collaborative research between the UFSC and the TU Berlin by Krebs & Riedel;
- b) Classify the grinding wheels according to the characteristics obtained by X-ray tomography;
- c) Compare the results obtained according to the manufacturing label with the results obtained in accordance with the X-ray tomography classification;
- d) Verify the influence of the grinding wheel phase fraction (pores, binder, and abrasives) on the work results, by individually modifying each variable; and
- e) Verify the influence of the grinding wheel manufacturing route on the structure.

REFERENCES

- [1] Liu, M.; Zhang, K.; Xiu, S. Mechanism investigation of hardening layer hardness uniformity based on grind-hardening process. **International Journal of Advanced Manufacturing Technology**, n. 88, 2017, pp. 3185-3194.
- [2] Wegener, K.; Bleicher, F.; Krajnik, P.; Hoffmeister, H.-W.; Brecher, C. Recent developments in grinding machines. **CIRP Annals – Manufacturing Technology**, n. 66, 2017, pp. 779-802.
- [3] Boaron, A.; Weingaertner, W.L. Dynamic in-process characterization method based on acoustic emission for topographic assessment of conventional grinding wheels. **Wear**, n. 406-407, 2018, pp. 218-229.
- [4] Madopothula, U.; Lakshmanan, V.; Nimmagadda, R.B. Time dependent behavior of alumina grains manufactured by two different routes while grinding of AISI 52100 steels. **Archives of Civil and Mechanical Engineering**, n. 17, 2017, pp. 400-409.
- [5] Aurich, J. C.; Linke, B.; Hauschild, M.; Carrella, M.; Kirsch, B. Sustainability of Abrasive Processes. **CIRP Annals - Manufacturing Technology**, n. 62 (2), 2013, pp. 653-672.
- [6] Oliveira, J.F.G.; Silva, E.J.; Guo, C.; Hashimoto, F. Industrial challenges in grinding. **CIRP Annals – Manufacturing Technology**, n. 58, 2009, pp. 663-680.
- [7] Godino, L.; Pombo, I.; Sanchez, J.A.; Alvarez, J. On the development and evolution of wear flats in microcrystalline sintered alumina grinding wheels. **Journal of Manufacturing Processes**, n. 32, 2018, pp. 494-505.
- [8] Jin, T.; Yi, J.; Peng, S. Determination of burn thresholds of precision gears in form grinding based on complex thermal modeling and Barkhausen noise measurements. **International Journal of Advanced Manufacturing Technology**, n. 88, 2017, pp. 789-800.
- [9] Salonitis, K. **Grind hardening Process**. 1 ed., Springer Cham Heidelberg New York Dordrecht London, 2015, 102 p.
- [10] Liu, M.; Nguyen, T.; Zhang, L.; Wu, Q.; Sun, D. Effect of grinding-induced cyclic heating on the hardened layer generation in the plunge grinding of a cylindrical component. **International Journal of Machine Tools & Manufacture**, n. 89, 2015, pp. 55-63.
- [11] Akintseva, A.; Pereverzev, P. Complex optimization of parameters for controlling the cycle of internal grinding by the method of dynamic programming. **MATEC Web of Conferences Annals**, n. 129, 2017, 4 p.
- [12] Dražumerič, R.; Roininen, R.; Badger, J.; Krajnik, P. Temperature-based method for determination of feed increments in crankshaft grinding. **Journal of Materials Processing Technology**, n. 259, 2018, pp. 228-234.
- [13] Nadolny, K. State of the art in production, properties and applications of the microcrystalline sintered corundum abrasive grains. **International Journal of Advanced Manufacturing Technology**, n. 74, 2014, pp. 1445-1457.

- [14] Linke, B.S. Review on grinding tool wear in terms of sustainability. **Proceedings of the ASME 2014 International Manufacturing Science and Engineering Conference**, Detroit, Michigan, USA, 2014, 9 p.
- [15] Dong, D.; Guo, G.; Yu, D.; An, Q.; Chen, M. Experimental investigation on the effects of different heat treatment processes on grinding machinability and surface integrity of 9Mn2V. **International Journal of Advanced Manufacturing Technology**, n. 81, 2015, pp. 1165-1174.
- [16] Fathallah, B.B.; Fredj, N.B.; Sidhom, H.; Braham, C.; Ichida, Y. Effects of abrasive type cooling mode and circumferential grinding wheel speed on the AISI D2 steel ground surface integrity, **International Journal of Machine Tools & Manufacture**, n. 49, 2009, pp. 261-272.
- [17] Madopothula, U.; Nimmagadda, R.B.; Lakshmanan, V. Assessment of white layer in hardened AISI 52100 steel and its prediction using grinding power. **Machining Science and Technology**, n. 22:2, 2018.
- [18] Benini, L.W. **Influência do teor de grãos microcristalinos de Al_2O_3 em rebolos convencionais na retificação de ADI**. Doctoral dissertation (In portuguese), Universidade Federal de Santa Catarina, Florianópolis, SC. 2017, 176 p.
- [19] Brunner, G. **Schleifen mit mikrokristallinem aluminiumoxid**. Doctoral dissertation (In german), Universität Hannover, Hanover, Germany, 1997, 135 p.
- [20] Linke, B.S. **Life Cycle and Sustainability of Abrasive Tools**. Springer International Publishing AG, Switzerland, 2016, 276 p.
- [21] Klocke, F. **Manufacturing processes: Grinding, Honing, Lapping**, vol. 2, Springer-Verlag Berlin Heidelberg, 2009, 452 p.
- [22] Deutsche Institut für Normung 8589: **Fertigungsverfahren Spanen Teil 11: Schleifen mit rotierendem Werkzeug - Einordnung, Unterteilung, Begriffe**, 2003, 18 p.
- [23] Malkin, S. **Grinding Technology: Theory and applications of machining with abrasives**. 2nd edition, Industrial Press, New York, 2008, 387 p.
- [24] Dong, S. **Continuous optimal infeed control for cylindrical plunge grinding. Doctoral dissertation**, University of Massachusetts, Massachusetts, USA, 2004, 80 p.
- [25] Saljé, E.; Mushardt, H.; Scherf, E. Optimization of short grinding cycles. **CIRP Annals – Manufacturing Technology**, n. 29, 1980, pp. 477-495.
- [26] Rowe, W.B. **Principles of Modern Grinding Technology**. 1 ed., William Andrew, Elsevier, Oxford, UK, 2009, 421 p.
- [27] Li, G.F.; Wang, L.S.; Yang, L.B. Multi-parameter optimization and control of the cylindrical grinding process. **Journal of Materials Processing Technology**, n. 139, 2001, pp. 232-236.
- [28] Inasaki, I. Monitoring and optimization of internal grinding process. **CIRP Annals – Manufacturing Technology**, n. 40, 1991, pp. 359-362.

- [29] Andretta, J.M. **Análise do erro de forma na retificação interna de assentos de bicos injetores**. Master thesis, Universidade Federal de Santa Catarina, Florianópolis, Santa Catarina, 2012, 152 p.
- [30] Pereverzev, P.P.; Popova, A.V.; Pimenov, D.Yu. Relation between the cutting force in internal grinding and the elastic deformation of the technological system. **Russian Engineering Research**, n. 35:3, 2015, pp. 215-217.
- [31] Chang, Z.; Jia, Q.; Yuan, X.; Chen, Y. Optimization of the grinding process to improve the surface integrity of bearing raceways. **International Journal of Advanced Manufacturing Technology**, n. 91, 2017, pp. 4243-4252.
- [32] Rudapрати, R.; Pal, P.K.; Bandyopadhyay, A. Modeling and optimization of machining parameters in cylindrical grinding process. **International Journal of Advanced Manufacturing Technology**, n. 82, 2016, pp. 2167-2182.
- [33] Webster, J.; Zhao, Y. W. Time-optimum adaptive control of plunge grinding. **International Journal of Machine Tools and Manufacture**, n. 30(3), pp. 413-421.
- [34] González-Santander, J. L.; Fernández, R.; Martín, G.; Arrazola, P. J. A useful analytical formula to avoid thermal damage in the adaptive control of dry surface grinding. **International Journal of Mechanical Sciences**, n. 117, 2016, pp. 152-161.
- [35] Ning, D. Xiaowen, Y.; Dingtong, Z. An intelligent supervision system for workpiece size in cylindrical grinding. In: **Second WRI Global Congress on Intelligent Systems**, 2010, 4 p.
- [36] Nguyen, T.; Zhang, L.C. Realisation of grinding-hardening in workpieces of curved surfaces – Part 1: Plunge cylindrical grinding. **International Journal of Machine Tools & Manufacture**, n. 51, 2011, pp. 309-319.
- [37] Hillier, F. S.; Liebermann, G.J. **Introduction to operations research**. 7th ed., McGraw-Hill, New York, NY, 2001, 1237 p.
- [38] Pereverzev, P. P.; Akintseva, A. V. The problem resolution of designing of cycles in the conditions of modern automated production. **Russian Engineering Research**, n. 37:6, 2017, pp. 523-529.
- [39] Weingaertner, W.L.; Taborga, A.R.M.; Taborga, J.D.M. Análise dos danos térmicos na retificação (In Portuguese). **Annals of the 16th Brazilian Congress of Mechanical Engineering**, 2001, pp. 333-341.
- [40] Marinescu, I.D.; Hitchiner, M.; Uhlmann, E.; Rowe, W.B.; Inasaki, I. Handbook of Machining with Grinding Wheels, CRC Press, 2007, 629 p. ISBN: 978-1-57444-671-5.
- [41] Kohli, S.; Guo; C., Malkin, S. Energy Partition to the Workpiece for Grinding with Aluminum Oxide Wheels and cBN Abrasive Wheels. **Journal of Engineering for Industry**, 1995, pp. 160-168.
- [42] Guo, C.; Wu, Y.; Varghese, V.; Malkin, S. Temperatures and energy partition for grinding with vitrified cBN wheels. **CIRP Annals – Manufacturing Technology**, n. 48, 1999, pp. 247-250.

- [43] Ueda, T.; Sato, M.; Nakayama, K. Cooling Characteristics of Cutting Grain in Grinding. **CIRP Annals – Manufacturing Technology**, vol. 45, 1996, pp. 293-298.
- [44] Chandradass, J.; Bae, D.S.; Balasubramanian, M. Synthesis and Characterization of Sol-Gel Alumina Fiber by Seeding α -Alumina Through Extended Ball Milling. **Materials and Manufacturing Processes**, n. 23, 2008, pp. 786-790.
- [45] Shaw, M.C. **Principles of Abrasive Processing**. 2nd ed, Oxford University Press Inc., New York, 2006, 610 p.
- [46] Nadolny, K. Wear phenomena of grinding wheels with sol-gel alumina abrasive grains and glass–ceramic vitrified bond during internal cylindrical traverse grinding of 100Cr6 steel. **International Journal of Advanced Manufacturing Technology**, n. 77, 2015, pp. 83-98.
- [47] Jackson, M.J.; Davim, J.P. **Machining with Abrasives**. Springer Science+Business Media, New York, 2011, 439 p.
- [48] Klocke, F.; Engelhorn, R.; Mayer, J.; Weirich, Th. Micro-Analysis of the Contact Zone of Tribologically Loaded Second-Phase Reinforced Sol-Gel-Abrasives. **CIRP Annals – Manufacturing Technology**, n. 51:1, 2002, pp. 245-250.
- [49] Mayer, J.; Engelhorn, R.; Bot, R.; Weirich, T.; Herwartz, C.; Klocke, F. Wear characteristics of second-phase-reinforced sol-gel corundum abrasives. **Acta Materialia**, n. 54, 2006, pp. 3605-3615.
- [50] Lindsay, R.P. The Performance of Seeded Gel Abrasives in the Laboratory and at Customer Test Sites. **Aircraft Engineering and Aerospace Technology**, n. 61:10, 1989, pp. 20-26.
- [51] Eranki, J.; Xiao, G.; Malkin, S. Evaluating the performance of “seeded gel” grinding wheels. **Journal of Materials Processing Technology**, n. 32, 1992, pp. 609-625.
- [52] Yamauchi, K.; Ueda, N. Dressing Mechanism of the SG Wheel. **Transactions of the Japan Society of Mechanical Engineers, Part C**, n. 62:597, 1996, pp. 2037-2043.
- [53] Wegener, K.; Hoffmeister, H.-W.; Karpuschewski, B.; Kuster, F.; Hahmann, W.-C.; Rabiey, M. Conditioning and monitoring of grinding wheels. **CIRP Annals - Manufacturing Technology**, n. 60, 2011, pp. 757-777.
- [54] Leskovar, P.; Peklenik, J. Influences affecting surface integrity in the cutting process. **CIRP Annals – Manufacturing Technology**, n. 31, 1982, pp. 447-450.
- [55] Davim, J.P. **Surface Integrity in Machining**. Springer London Dordrecht Heidelberg New York, 2010, 222 p.
- [56] Brinksmeier, E.; Tönshoff, H.K. X-Ray Stress Measurement - a Tool for the Study and Layout of Machining Processes. **CIRP Annals – Manufacturing Technology**, n. 34, 1985, pp. 485-490.
- [57] Field, M.; Kahles, J.F. The surface integrity of machined and high strength steels. **DMIC Report**, n. 210, 1964, 517 p.
- [58] Griffiths, B. **Manufacturing surface technology**. London: Penton Press, 2001, 237 p.

- [59] Boehs, L. **Análise de superfícies usinadas**. Florianópolis, class notes, 1992.
- [60] Klocke, F. **Manufacturing processes: Cutting**, vol. 1, Springer-Verlag Berlin Heidelberg, 2009, 517 p.
- [61] König, W. **Fertigungsverfahren: Schleifen, Honen, Läppen (VDI-Buch)** (German Edition). 2 ed., n. 2, Düsseldorf, German, 1989.
- [62] Brinksmeier, E.; Walter, A. Generation of reaction layers on machined surfaces. **CIRP Annals – Manufacturing Technology**, n. 49, 2000, pp. 435-438.
- [63] Jiang, X.J.; Whitehouse, D.J. Technological shifts in surface metrology. **CIRP Annals - Manufacturing Technology**, n. 61, 2012, pp. 815-836.
- [64] Whitehouse, D.J. **Surfaces and their measurement**. 1 ed., Hermes Penton Ltd., 2002, 425 p. ISBN19039 96015.
- [65] Noppen, G.; Sigalla, J.; Czichos, H.; Petersohn, D.; Schwarz, W. **Technische Oberflächen**, n.1-2, 2 ed., Beuth Verlag GmbH, Berlin and Cologne, 1985, 82 p.
- [66] Marra, L.A. **Influência da concentração de grãos de Al_2O_3 microcristalinos sobre a força e textura na retificação cilíndrica externa de mergulho**. Master thesis (In portuguese), Universidade Federal de Santa Catarina, SC, Brazil, 2018, 106 p.
- [67] Kitamura, F.; Gotanda, K. High performance steel grinding using SG/Alumina wheels. **Journal of the Japan Society for Precision Engineering**, n. 58, 1992, pp. 583-585.
- [68] Littman, W.E. **The influence of the grinding process on the structure of hardened steel**. Doctoral dissertation, Massachusetts Institute of Technology, 1953, 87 p.
- [69] Brockhoff, T. Grind-Hardening: A Comprehensive View. **CIRP Annals – Manufacturing Technology**, n. 48, 1999, pp. 255-260.
- [70] Abbaschian, R.; Abbaschian, L.; Reed-Hill, R.E. **Physical metallurgy principles**. 4 ed., Cengage Learning, 2009, 769 p.
- [71] Abrão, A.M.; Aspinwall, D.K. The surface integrity of turned and ground hardened bearing steel. **Wear**, n. 196, 1996, pp. 279-284.
- [72] Bairi, B.S.; Radhakrishnan, V. **Study of the surface layer of ground high strength steels**. **Wear**, n. 35, 1975, pp. 41-52.
- [73] Barbacki, A.; Kawalec, M.; Hamrol, A. Turning and grinding as a source of microstructural changes in the surface layer of hardened steel. **Journal of Materials Processing Technology**, n. 133, 2003, pp. 21-25.
- [74] Shaw, M.C.; Vyas, A. Heat-affected zones in grinding steel. **CIRP Annals - Manufacturing Technology**, n. 43, 1993, pp. 279-282.
- [75] Anderson, D.; Warkentin, A.; Bauer, R. Comparison of numerically and analytically predicted contact temperatures in shallow and deep dry grinding with infrared

- measurements. **International Journal of Machine Tools & Manufacture**, n. 48, 2008, pp. 320-328.
- [76] Nguyen, T.; Zhang, L.C. Grinding–hardening using dry air and liquid nitrogen: Prediction and verification of temperature fields and hardened layer thickness. **International Journal of Machine Tools & Manufacture**, n. 50, 2010, pp. 901-910.
- [77] Walton, I.M.; Stephenson, D.J.; Baldwin, A. The measurement of grinding temperatures at high specific material removal rates. **International Journal of Machine Tools & Manufacture**, n. 46, 2006, pp. 1617-1625.
- [78] Fang-yuan, Z.; Chun-zheng, D.; Min-jie, W.; Wei, S. White and dark layer formation mechanism in hard cutting of AISI52100 steel. **Journal of Manufacturing Processes**, n. 32, 2018, pp. 878-887.
- [79] Salonitis, K.; Stavropoulos, P.; Stournaras, A.; Chryssolouris, G. Finite element modeling of grind hardening process. In: **Proceedings of the 10th CIRP international workshop on modeling of machining operations**, Calabria, Italy, 2007, pp. 117–123.
- [80] Brinksmeier, E.; Brockhoff, T. Utilization of Grinding Heat as a New Heat Treatment Process. **CIRP Annals – Manufacturing Technology**, n. 45, 1996, pp. 283-286.
- [81] Grum, J. A review of the influence of grinding conditions on resulting residual stresses after induction surface hardening and grinding. **Journal of Materials Processing Technology**, n. 114, 2001, pp. 212-226.
- [82] Silva, L.R.; Mattos, M.F.; Amaral, L.V.; Corrêa, E.C.S.; Brandão, J.R. Behavior of surface integrity in cylindrical plunge grinding using different cooling systems. **Materials Research**, n. 14:2, 2011, pp. 206-211.
- [83] Vashista, M.; Paul, S. Correlation between surface integrity of ground medium carbon steel with Barkhausen Noise parameters and magnetic hysteresis loop characteristics. **Materials and Design**, n. 30, 2009, pp. 1595-1603.
- [84] Brinksmeier, E.; Cammett, J.T.; König, W.; Leskovic, P.; Peters, J.; Tönshoff, H.K. Residual Stresses – Measurement and Causes in Machining Processes. **CIRP Annals – Manufacturing Technology**, n. 31, 1982, pp. 491-510.
- [85] Balart, M.J.; Bouzina, A.; Edwards, L.; Fitzpatrick, M.E. The onset of tensile residual stresses in grinding of hardened steels. **Materials Science and Engineering A**, n. 367, 2004, pp. 132-142.
- [86] Kruszynski, B.W. Wójcik, R. Residual stress in grinding, **Journal of Materials Processing Technology**, n. 109, 2001, pp. 254-257.
- [87] Zarudi, I. Zhang, L.C. A revisit to some wheel-workpiece interaction problems in surface grinding. **International Journal of Machine Tools & Manufacture**, n. 42, 2002, pp. 905-913.
- [88] Alonso, U.; Ortega, N.; Sanchez, J.A.; Pombo, I.; Plaza, S. Izquierdo, B. In-process prediction of the hardened layer in cylindrical traverse grind-hardening. **International Journal of Advanced Manufacturing Technology**, n. 71, 2014, pp. 101-108.

- [89] Jermolajev, S.; Brinksmeier, E. A new approach for the prediction of surface and subsurface properties after grinding. **Advanced Materials Research**, n. 1018, 2014, pp. 189-196.
- [90] Sridharan, U.; Bedekar, V.; Kolarits, F.M. A functional approach to integrating grinding temperature modeling and Barkhausen noise analysis for prediction of surface integrity in bearing steels. **CIRP Annals – Manufacturing Technology**, n. 66, 2017, pp. 333-336.
- [91] Linke, B.S.; Corman, G.J.; Dornfeld, D.A.; Tönissen, S. Sustainability indicators for discrete manufacturing processes applied to grinding technology. **Journal of Manufacturing Systems**, n. 32, 2013, pp. 556-563.
- [92] Haapala, K. R.; Zhao, F.; Camelio, J.; Sutherland, J. W.; Skerlos, S. J.; Dornfeld, D. A.; Jawahir, I. S.; Zhang, H. C.; Clarens, A. F. A review of engineering research in sustainable manufacturing. **Proceedings of the ASME International Manufacturing Science and Engineering Conference 2011**, 2011, pp. 599-619.
- [93] ASTM E3096-18. **Standard Guide for Definition, Selection, and Organization of Key Performance Indicators for Environmental Aspects of Manufacturing Processes**, 2018.
- [94] Kibira, D.; Brundage, M. P.; Feng, S.; Morris, K. C. Procedure for Selecting Key Performance Indicators for Sustainable Manufacturing. **Journal of Manufacturing Science and Engineering**, n. 140, 2018, 7 p.
- [95] Linke, B.S.; Garcia, D.; Kaur, G.; Ghadamli, F. Sustainable process planning for subtractive and additive manufacturing unit processes. In: **Proceedings of the ASME 2016 International Manufacturing Science and Engineering Conference**, Blacksburg, Virginia, USA, 2016, 7 p.
- [96] Linke, B.; Das, J.; Lam, M.; Ly, C. Sustainability Indicators for Finishing Operations based on Process Performance and Part Quality, **Procedia CIRP**, n. 14, 2014, pp. 564-569.
- [97] Linke, B. S. Sustainability Indicators for Grinding Applied to Dressing Strategies, **Journal of Manufacturing Science and Engineering**, n. 135, 2013, 6 p.
- [98] Kellens, K.; Dewulf, W.; Overcash, M.; Hauschild, M.Z.; Duflou, J.R. Methodology for systematic analysis and improvement of manufacturing unit process life-cycle inventory (UPLCI) —**CO2PE! initiative (cooperative effort on process emissions in manufacturing)**. Part 1: Methodology description, *International Journal of Life Cycle Assessment*, n. 17, 2012, pp. 69-78.
- [99] Linke, B.; Overcash, M. Reusable unit process life cycle inventory for manufacturing: grinding, **Production Engineering - Research and Development**, n. 11, 2017, pp. 643-653.
- [100] Zema Zselics Ltda. **Manual de manutenção da retificadora Pratika Flexa-G600-L**, 2003, 132 p.
- [101] Tecnotempera. **Procedimento de tratamento térmico**. Tecnotêmpera, 2017, 1 p.
- [102] LMPT – Laboratório de Meios Porosos e Propriedades Termofísicas. **Relatório de aquisição de imagens**. Universidade Federal de Santa Catarina, Florianópolis, SC. 2018, 28 p.

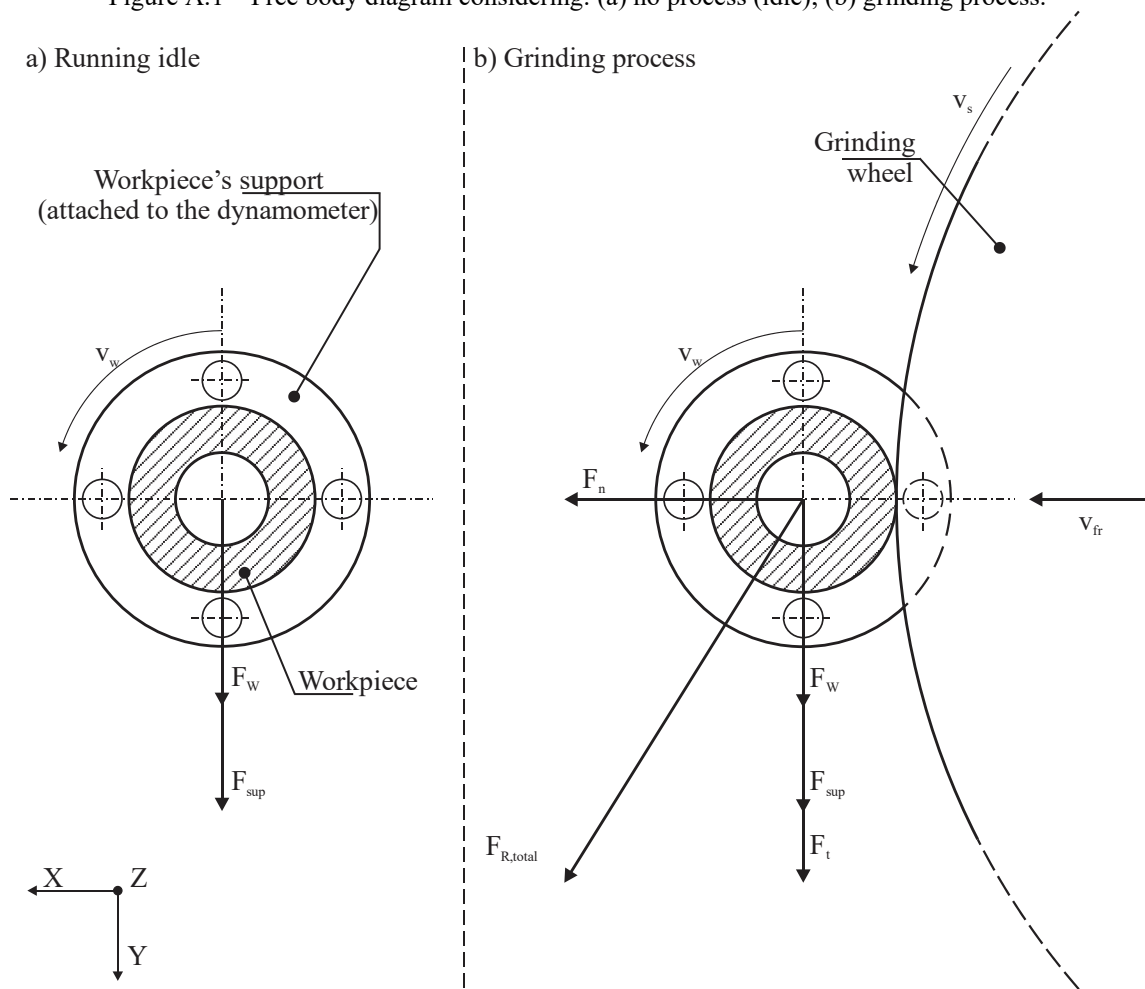
- [103] Landis, E. N.; Keane, D. T. X-ray microtomography. **Materials Characterization**, n. 61, 2010, pp. 1305-1316.
- [104] Kistler. **Rotating cutting dynamometer Type 9123C Instruction Manual**. Kistler Group, 2010, 59 p.
- [105] Boaron, A. **Desenvolvimento e validação de um método dinâmico, baseado em emissão acústica, para a caracterização em processo de rebolos convencionais**. Doctoral dissertation (In portuguese), Universidade Federal de Santa Catarina, UFSC, Florianópolis, Santa Catarina. 2015, 206 p.
- [106] Pereira, E. L. **Elaboração de algoritmo em linguagem Python para otimização de ciclos de retificação cilíndrica**. Internship report, Universidade Federal de Santa Catarina, UFSC, Florianópolis, Santa Catarina. 2018, 15 p.
- [107] Arganda-Carreras, I.; Kaynig, V.; Rueden, C.; Eliceiri, K. W.; Schindelin, J.; Cardona, A.; Seung, H. S. Trainable Weka Segmentation: a machine learning tool for microscopy pixel classification. **Bioinformatics**, n. 33:15, 2017, pp.2424-2426.
- [108] Datafolha. **Consulta de cargos e salários 2010**. Available at: {Hyperlink “<http://datafolha1.folha.com.br/empregos/salarios>” }. Accessed: November 30th, 2018.
- [109] Zeng, Q. **Surface integrity evaluation and the effect of machining-induced surface integrity characteristics on part’s performance**. Doctoral dissertation, University of Strathclyde, Glasgow, Scotland, UK. 2015, 197 p.
- [110] Gao, Y.-k.; Li, X.-b.; Yang, Q.-x.; Yao, M. Influence of surface integrity on fatigue strength of 40CrNi2Si2MoVA steel. **Material Letters**, n. 61, 2007, pp. 466-469.
- [111] Smith, S.; Melkote, S.N.; Lara-Curzio, E.; Watkins, T.R.; Allard, L.; Riester, L. Effect of surface integrity of hard turned AISI 52100 steel on fatigue performance. **Materials Science and Engineering A**, n. 459, 2007, pp. 337-346.
- [112] Hashimoto, F.; Guo, Y.B.; Warren, A.W. Surface integrity difference between hard turned and ground surfaces and its impact on fatigue life. **CIRP Annals – Manufacturing Technology**, n. 55, 2006, 4 p.
- [113] Choi, Y. Influence of white layer on the performance of hard machined surfaces in rolling contact. **Journal of Engineering Manufacture**, n. 224, 2010, pp. 1207-1215.
- [114] Linke, B.S.; Corman, G.J.; Dornfeld, D.A.; Tönissen, S. Sustainability indicators for discrete manufacturing processes applied to grinding technology. **Journal of Manufacturing Systems**, n. 32, 2013, pp. 556-563.
- [115] Zhang, H.; Haapala, K.R. Integrating sustainable manufacturing assessment into decision making for a production work cell. **Journal of Cleaner Production**, n. 105, 2015, pp. 52-63.
- [116] Linke, B.S.; Garcia, D.; Kaur, G.; Ghadamli, F. Sustainable process planning for subtractive and additive manufacturing unit processes. In: **Proceedings of the ASME 2016 International Manufacturing Science and Engineering Conference**, Blacksburg, Virginia, USA, 2016, 7 p.

- [117] Behrens, B.-A.; Seidel, H.-J.; Lange, F.; Kammler, M. Vergleichende experimentelle und numerische Untersuchungen zum schwingungsberlagerten Pressen zweier Pulvermaterialien, **Materialwissenschaft und Werkstofftechnik**, n. 2:8, 2011, pp. 705-711.
- [118] Bot-Schulz, R. **Untersuchung der Reaktionen an der Schnittstelle Korn/Bindung für Sol-Gel-Korund**. Doctoral dissertation (In german). Institute of Machine Tools and Production Engineering (WZL), Aachen, 2005, 157 p.
- [119] Korlinov, A. S.; Safonov, I. V. An overview of watershed algorithm implementations in open source libraries. **Journal of Imaging**, n. 4, 2018, 15 p.
- [120] GrindoSonic. **Application: Abrasives and Grinding**. Available at: {Hyperlink "https://www.grindosonic.com/applications/abrasives_grinding.html" }. Accessed: October 23rd, 2019.
- [121] Uhlmann, E.; Hasper, G.; Heitmüller, F. Verschleißmodell für Sinterkorundschleifscheiben. **Werkstattstechnik online**, n. 6, 2013, pp. 511-516.
- [122] Madopothula, U.; Lakshaman, V.; Nimmagadda, R.B. Time dependent behavior of alumina grains manufactured by two different routes while grinding of AISI 52100 steels. **Archives of Civil and Mechanical Engineering**, n. 17, 2017, pp. 400-409.
- [123] Caraguay, S. J. **Influência da concentração de grãos abrasivos de óxido de alumínio microcristalino sobre o desgaste de rebolos**. Master's thesis (In portuguese), Universidade Federal de Santa Catarina – UFSC, Florianópolis, SC, 2018, 138 p.
- [124] Zhao, Z.; Xu, J.; Fu, Y.; Zhang, Z. Performance of micro-crystalline ceramic alumina wheels during creep feed grinding nickel-based superalloy. **International Journal of Abrasive Technology**, n. 6, 2014, pp. 314-323.

APPENDIX A

The rotating cutting dynamometer, model 9124B1111, measures force signal in three Cartesian directions (X, Y, and Z), as well as torque in one direction (Z). Since the RCD device rotates during the force measurement, the force signal for the reference Cartesian directions X and Y were observed as a sinusoidal and cosine wave. Additionally, mass from the workpiece and workpiece's support system may alter the force magnitude. These precepts were taken into consideration, following the force calculation methodology elaborated by Boaron [105]. Figure A.1 illustrates the schematic free body diagram used for the force calculation.

Figure A.1 – Free body diagram considering: (a) no process (idle); (b) grinding process.



Source: Adapted from Boaron [105].

The tangential force (F_t) is evaluated based on both measured torque signal (M_z , around the Z-axis of the dynamometer) and average workpiece diameter ($d_{w, average}$), illustrated on Eq. (A.1)

$$F_t = \frac{M_z}{\frac{(d_{wi} - d_{wf})}{4}} = \frac{M_z}{\frac{d_{w, average}}{2}} \quad (A.1)$$

where:

M_z is the torque signal around Z-axis [N·m]

d_{wi} is the initial workpiece diameter [mm]

d_{wf} is the final workpiece diameter [mm]

$d_{w, average}$ is the average workpiece diameter [mm]

However, the normal force (F_n) can only be obtained by calculating the total resulting force $F_{R, total}$, tangential force F_t , as well as considering the interference of the system mass.

On one hand, during the idle process (Figure A.1a), the only forces actuating on the system are due to the workpiece and workpiece's holder mass, respectively F_w and F_{holder} . Since the dynamometer rotates, the reference system also rotates, the signal obtained by the force measuring system, directions X and Y, alternates between sinusoidal and cosine. Therefore, the resulting force of the idle process ($F_{R, idle}$) represents the interference caused by the F_w and F_{holder} forces. On the other hand, during the grinding process (Figure A.1b), tangential and normal grinding forces arise on the system, caused by the feed motion, as well as material removal. Consequently, the normal force can be calculated, according to Boaron [105], by the Eq. (A.2)

$$F_n = \sqrt{F_{R, total}^2 - (F_w + F_{holder} + F_t)^2} \quad (A.2)$$

where:

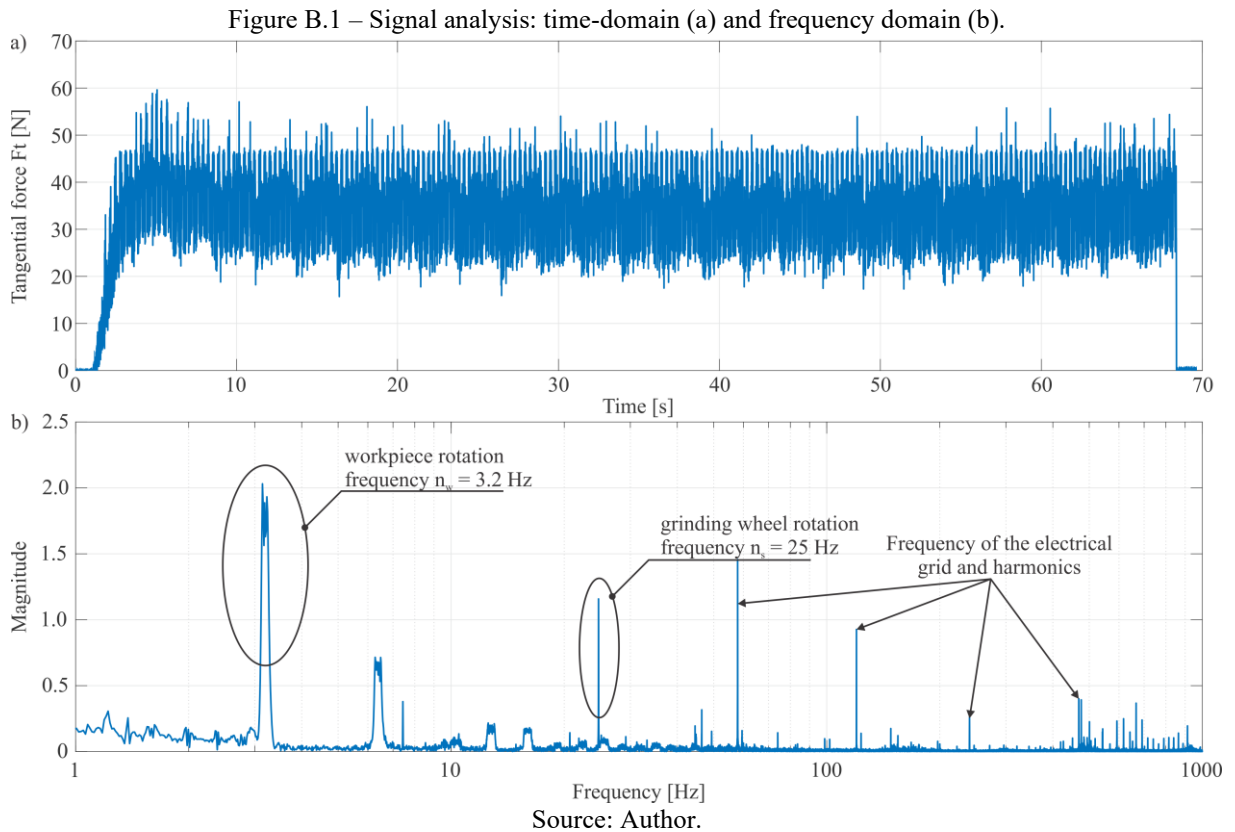
$F_{R, total}$ is the total resulting force from the forces on the X and Y axis [N]

F_w is the force due to the workpiece mass [N]

F_{holder} is the force due to the workpiece holder mass [N]

APPENDIX B

After force signal acquisition, the generated text file (from the Dynoware software) was analyzed both in time and frequency domain in order to select a suitable processing methodology. Force (F_t) was employed for time (Figure B.1a) and frequency (Figure B.1b) observations.



The observation concerning the frequency domain was employed to identify the frequencies during the process and, therefore, choose the suitable filter for the signals (Figure B.2a). In this case, two main frequencies were observed: $f_1 = 3.2$ Hz and $f_2 = 25$ Hz, equivalent respectfully to, workpiece and grinding wheel rotations.

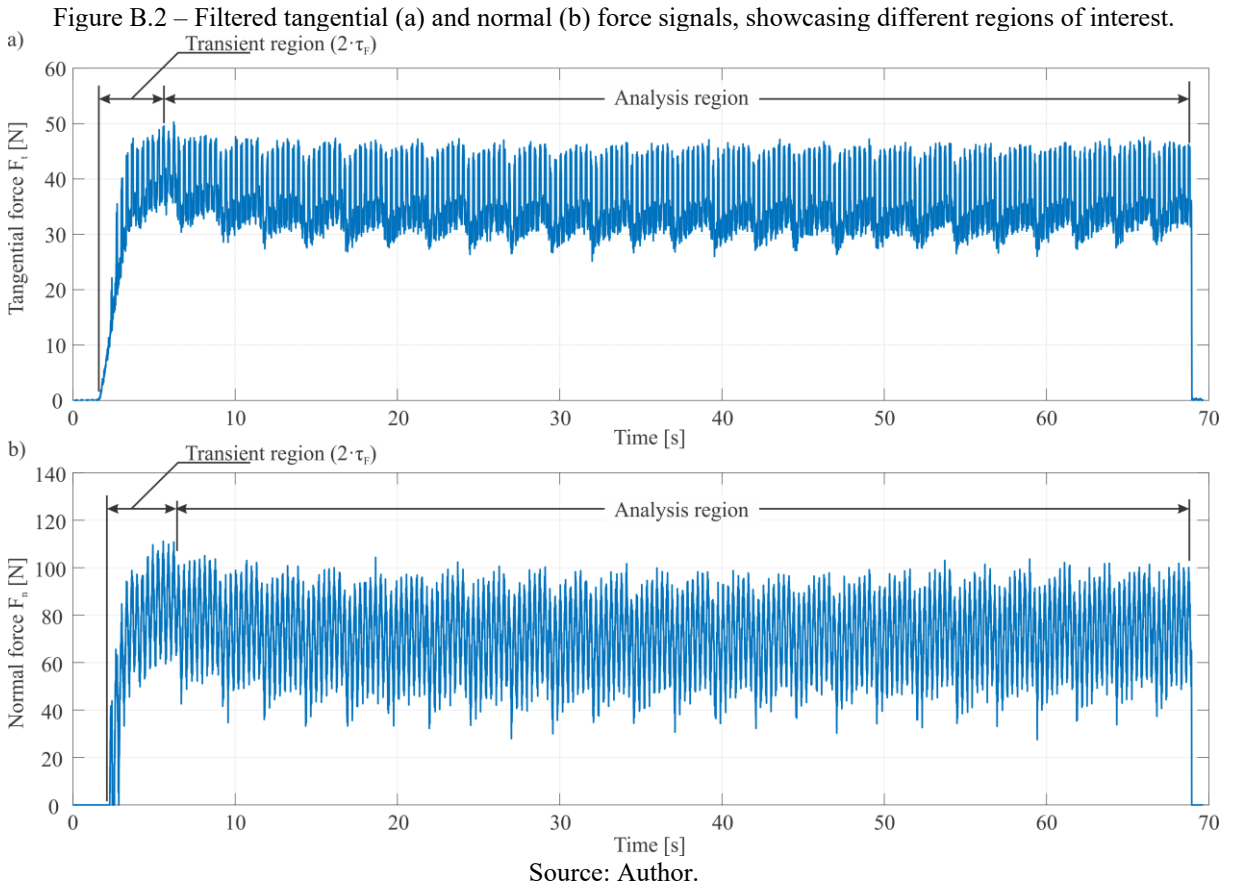
Time-domain observations served as a guideline to define the grinding wheel entrance transient region (from which the time coefficient τ_F was calculated) by using the Eq. (B.1) [26],

$$\tau_F = \frac{t_{\text{transient}}}{2} \quad (\text{B.1})$$

where

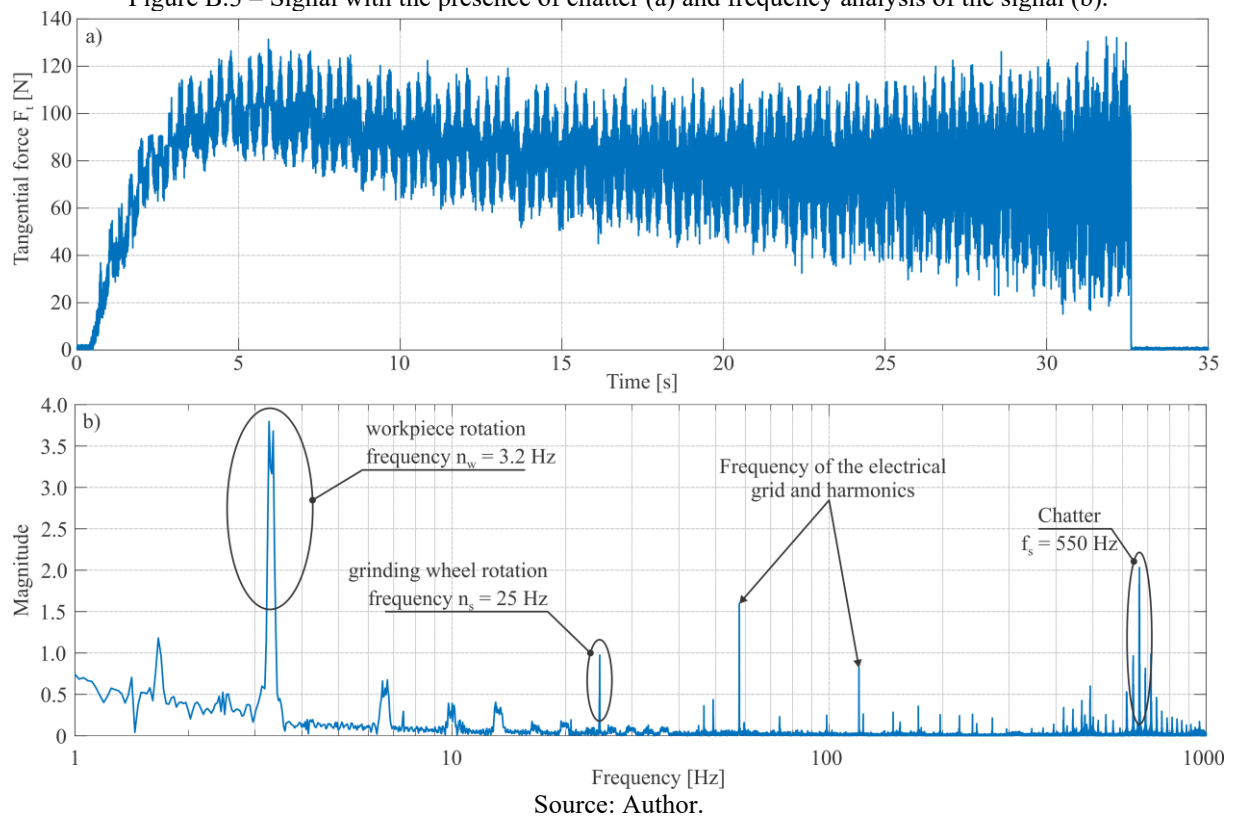
$t_{\text{transient}}$ is the grinding wheel entrance interval [s]

The analysis region (from which the average, standard deviation, and maximum forces were calculated) was also defined. These regions are highlighted on the illustrated signal and were used during the evaluation of the normal force filtered signal (Figure B.2b).



A higher frequency was observed when the grinding wheel reached the end of life force/vibration criteria. Figure B.3 illustrates an example.

Figure B.3 – Signal with the presence of chatter (a) and frequency analysis of the signal (b).



The frequency, in this case, coincides with the measured system natural frequency f_n of 550 Hz, establishing a threshold for the grinding experiments.

APPENDIX C

A selection of one metallographic image, for each sectioned surface, intended for the boundary-affected layer analysis was conducted. Stage I image examples are illustrated in Figure C.1, C.2, C.3, and C.4, respectively for the MC00, MC15, MC30, and MC45 grinding wheels.

Figure C.1 – Micrographs of the ground surface with an MC00 grinding wheel.

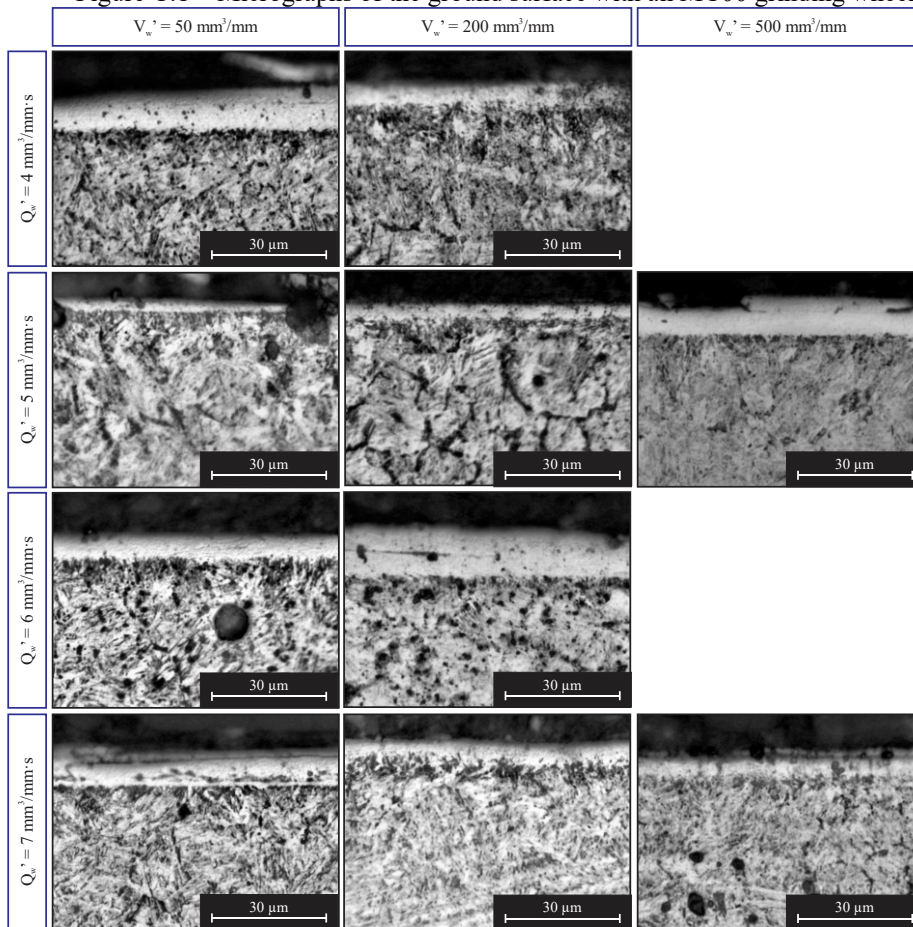
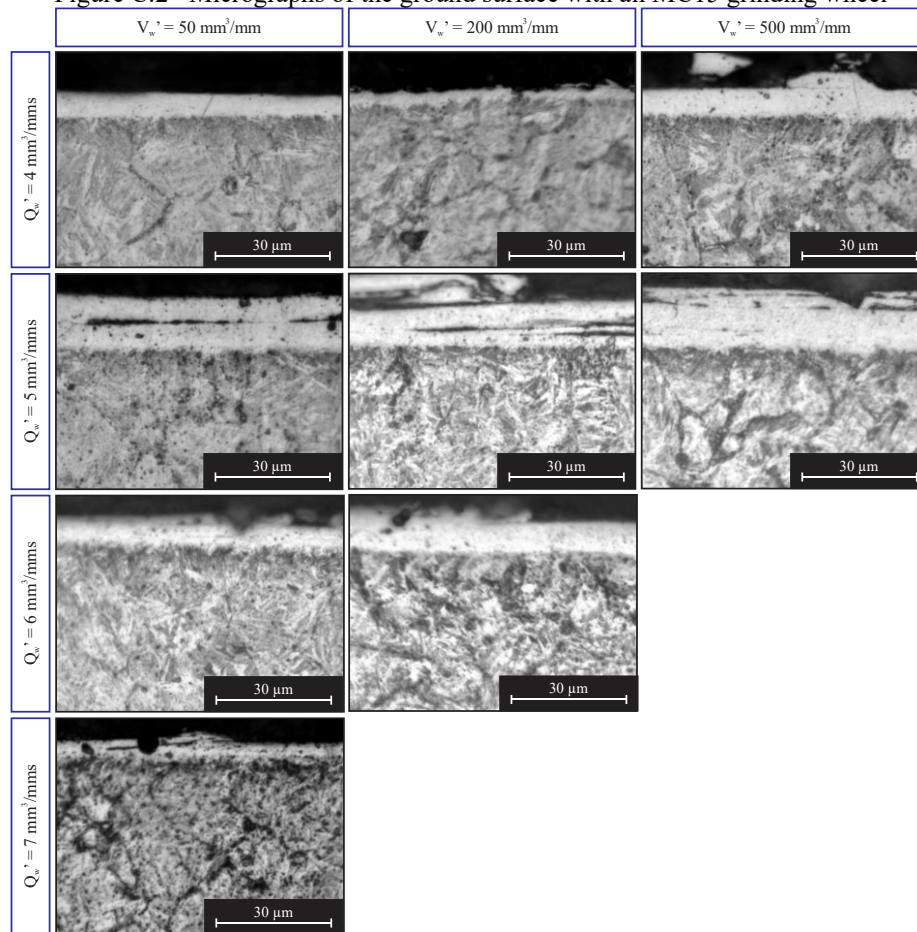
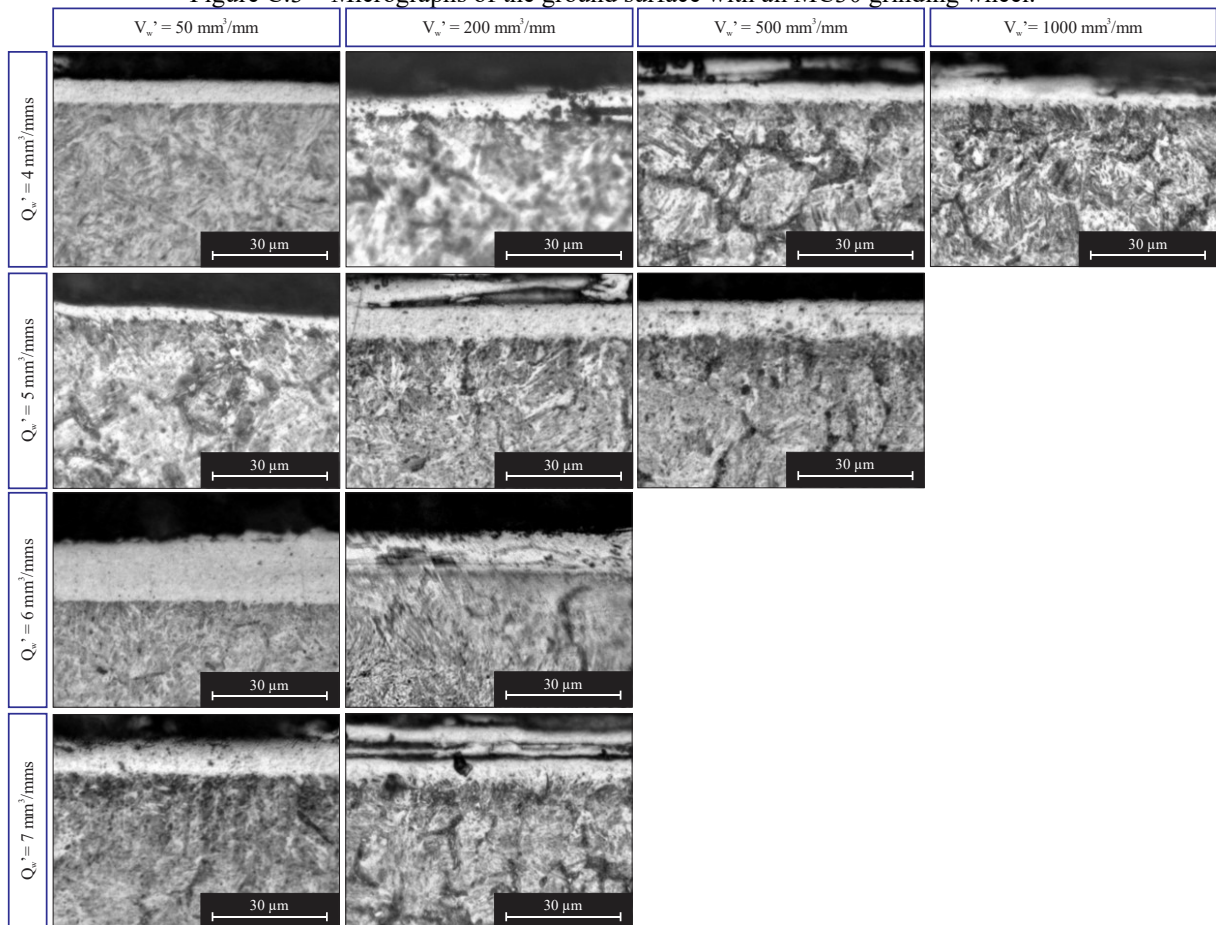


Figure C.2 –Micrographs of the ground surface with an MC15 grinding wheel



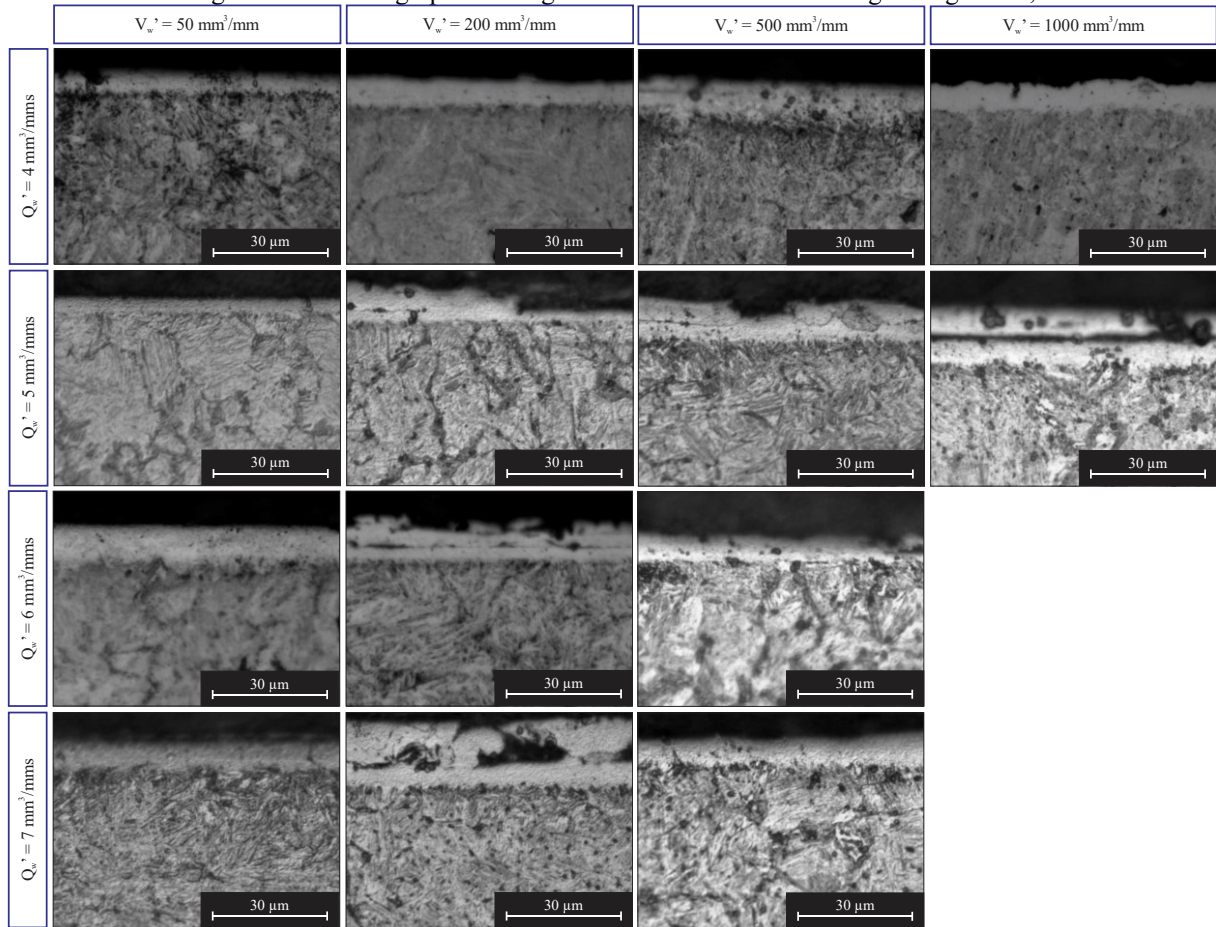
Source: Author.

Figure C.3 – Micrographs of the ground surface with an MC30 grinding wheel.



Source: Author.

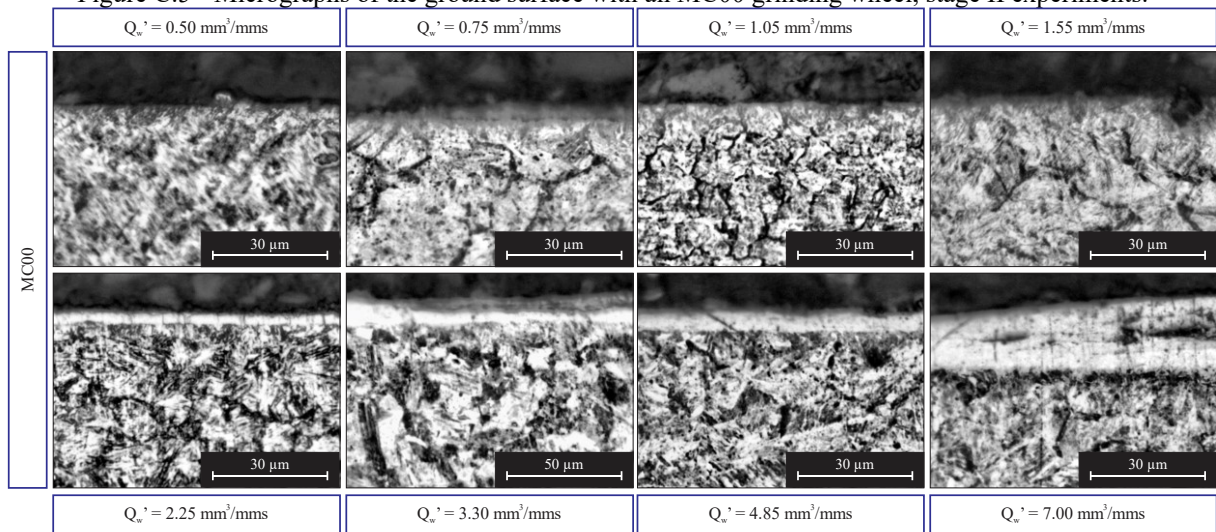
Figure C.4 – Micrographs of the ground surface with an MC45 grinding wheel;



Source: Author.

Complementarily, stage II analysis also contemplated the boundary-affected layer. Therefore, for reference, Figure C.5 illustrates examples of the metallographic images of the steel microstructure for an MC00 grinding wheel.

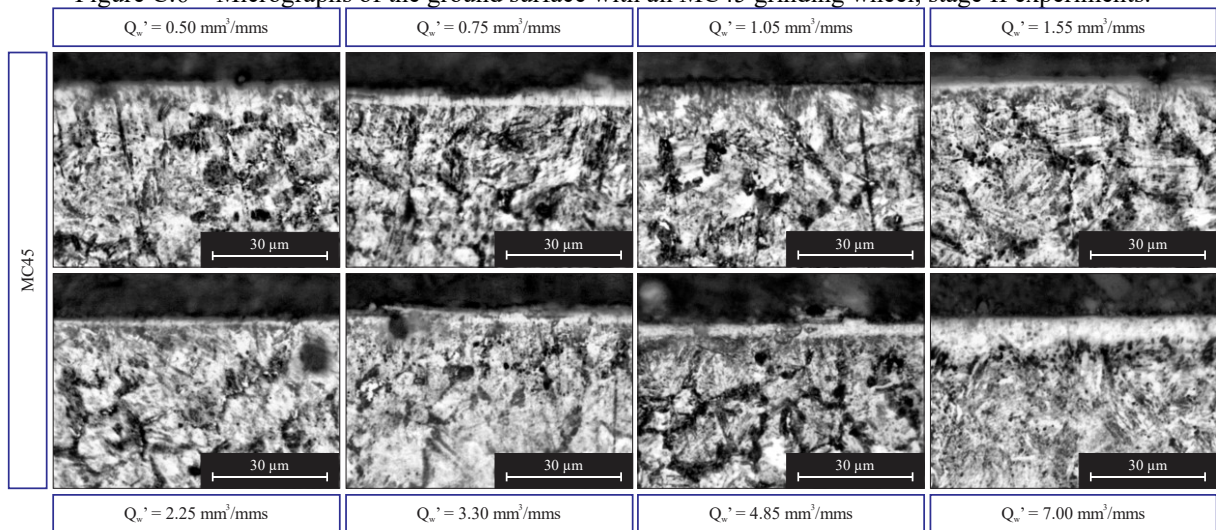
Figure C.5 - Micrographs of the ground surface with an MC00 grinding wheel, stage II experiments.



Source: Author.

Figure C.6 the metallographic images of the steel microstructure for an MC45 grinding wheel.

Figure C.6 – Micrographs of the ground surface with an MC45 grinding wheel, stage II experiments.



Source: Author.

APPENDIX D

From the results obtained on the stage II experiments, a database containing values for the: specific grinding force components (F_n' , F_t'), surface roughness (R_a , R_z), boundary-affected layer thickness (BAL), time coefficient (τ_F), specific material removal rate (Q_w'), radial feed rate (v_{fr}) was elaborated. This data was later used to elaborate on the multi-step external cylindrical grinding cycles using the developed algorithm in python language. The algorithm also included the specific material removal (V_w') and grinding energy (E_c), contemplated on the sustainability analysis.

The discrete data, with N interactions, used for each grinding cycle on the stage II experiments can be visualized in Table D.1, D.2, D.3, D.4. Since the steps are discretized values, the v_{fr} origin and destiny refers to actual radial feed rate values of the movement origin and destiny; u_{fr} refers to commanded radial feed rate.

Table D.1 – Discrete steps resulting from the grinding cycle algorithm, industry extrapolation, MC00.

N	$v_{fr, origin}$	$v_{fr, destiny}$	u_{fr}	Time	Total time	Q_w'	BAL	R_a	F_t	τ_F	E_c	V_w'
-	[mm/s]	[mm/s]	[mm/s]	[s]	[s]	[mm ³ /mm·s]	[mm]	[μ m]	[N]	[s]	[J]	[mm ³ /mm]
4	0.000	0.045	0.048	4.03	28.52	7.08	0.028	2.31	82.3	1.9	349.0	4.9
3	0.045	0.045	0.045	2.80	24.49	7.09	0.028	2.31	82.3	1.9	348.1	7.1
2	0.045	0.045	0.045	2.80	21.68	7.11	0.028	2.31	82.3	1.9	347.3	7.1
1	0.045	0.003	0.003	18.88	18.88	0.51	0.000	0.75	5.9	3.3	347.8	1.1

Source: Author.

Table D.2 – Discrete steps resulting from the grinding cycle algorithm, industry extrapolation, MC45.

N	$v_{fr, origin}$	$v_{fr, destiny}$	u_{fr}	Time	Total time	Q_w'	BAL	R_a	F_t	τ_F	E_c	V_w'
-	[mm/s]	[mm/s]	[mm/s]	[s]	[s]	[mm ³ /mm·s]	[mm]	[μ m]	[N]	[s]	[J]	[mm ³ /mm]
4	0.000	0.045	0.048	4.01	29.02	7.08	0.021	2.34	88.9	1.9	377.0	4.9
3	0.045	0.045	0.045	2.80	25.00	7.09	0.021	2.34	88.9	1.9	376.1	7.1
2	0.045	0.045	0.045	2.80	22.20	7.11	0.021	2.34	88.9	1.9	375.1	7.1
1	0.045	0.003	0.003	19.40	19.40	0.51	0.000	1.45	6.9	4.5	406.4	1.0

Source: Author.

Table D.3 – Discrete steps resulting from the grinding cycle algorithm, multi-step cycle, MC00.

N	V _{fr, origin}	V _{fr, destiny}	u _{fr}	Time	Total time	Q _{w'}	BAL	R _a	F _t	τ _F	E _c	V _{w'}
-	[mm/s]	[mm/s]	[mm/s]	[s]	[s]	[mm ³ /mm·s]	[mm]	[μm]	[N]	[s]	[J]	[mm ³ /mm]
14	0.000	0.045	0.075	1.40	14.13	7.08	0.028	2.31	82.3	1.9	349.0	4.1
13	0.045	0.045	0.045	0.80	12.73	7.08	0.028	2.31	82.3	1.9	348.7	7.1
12	0.045	0.045	0.045	0.80	11.93	7.09	0.028	2.31	82.3	1.9	348.5	7.1
11	0.045	0.045	0.045	0.80	11.13	7.09	0.028	2.31	82.3	1.9	348.2	7.1
10	0.045	0.045	0.045	0.80	10.33	7.10	0.028	2.31	82.3	1.9	348.0	7.1
9	0.045	0.045	0.045	0.80	9.53	7.10	0.028	2.31	82.3	1.9	347.8	7.1
8	0.045	0.045	0.045	0.80	8.73	7.11	0.028	2.31	82.3	1.9	347.5	7.1
7	0.045	0.045	0.045	0.80	7.93	7.11	0.028	2.31	82.3	1.9	347.3	7.1
6	0.045	0.045	0.045	0.80	7.13	7.12	0.028	2.31	82.3	1.9	347.0	7.1
5	0.045	0.045	0.045	0.80	6.33	7.12	0.028	2.31	82.3	1.9	346.8	7.1
4	0.045	0.045	0.045	0.80	5.52	7.13	0.028	2.31	82.3	1.9	346.5	7.1
3	0.045	0.045	0.045	0.80	4.72	7.13	0.028	2.31	82.3	1.9	346.3	7.1
2	0.045	0.031	0.015	0.96	3.92	4.94	0.012	1.84	46.3	1.8	281.2	5.9
1	0.031	0.003	0.000	2.96	2.96	0.51	0.000	0.75	5.9	3.3	347.2	1.9

Source: Author.

Table D.4 – Discrete steps resulting from the grinding cycle algorithm, multi-step cycle, MC45.

N	V _{fr, origin}	V _{fr, destiny}	u _{fr}	Time	Total time	Q _{w'}	BAL	R _a	F _t	τ _F	E _c	V _{w'}
-	[mm/s]	[mm/s]	[mm/s]	[s]	[s]	[mm ³ /mm·s]	[mm]	[μm]	[N]	[s]	[J]	[mm ³ /mm]
12	0.000	0.045	0.069	1.59	14.68	7.08	0.021	2.34	88.9	1.9	377.0	4.1
11	0.045	0.045	0.045	0.93	13.08	7.08	0.021	2.34	88.9	1.9	376.7	7.1
10	0.045	0.045	0.045	0.93	12.15	7.09	0.021	2.34	88.9	1.9	376.4	7.1
9	0.045	0.045	0.045	0.93	11.22	7.09	0.021	2.34	88.9	1.9	376.1	7.1
8	0.045	0.045	0.045	0.93	10.28	7.10	0.021	2.34	88.9	1.9	375.8	7.1
7	0.045	0.045	0.045	0.93	9.35	7.10	0.021	2.34	88.9	1.9	375.5	7.1
6	0.045	0.045	0.045	0.93	8.41	7.11	0.021	2.34	88.9	1.9	375.1	7.1
5	0.045	0.045	0.045	0.93	7.48	7.12	0.021	2.34	88.9	1.9	374.8	7.1
4	0.045	0.045	0.045	0.93	6.55	7.12	0.021	2.34	88.9	1.9	374.5	7.1
3	0.045	0.045	0.045	0.93	5.61	7.13	0.021	2.34	88.9	1.9	374.2	7.1
2	0.045	0.031	0.018	1.13	4.68	4.94	0.007	2.41	52.9	1.5	320.9	5.9
1	0.031	0.003	0.001	3.55	3.55	0.51	0.000	1.42	6.9	4.5	405.8	1.9

Source: Author.